Ref. Ares(2024)6837199 - 27/09/2024

Deliverable D3.6

Report on validation of recovered materials re-use on new cells

Funded by the European Union

Views and opinions expressed are those of the author(s) only and do not necessarily reflect those of the European Union or CINEA. Neither the European Union nor the granting authority can be held responsible for them.

This project has received funding from Horizon Europe research and innovation programme under Grant Agreement No.1069890

Feasible Recovery of critical raw materials through a new circular Ecosystem for a Li-Ion Battery cross-value chain in Europe

WP3 – Recycling technologies and materials re-using for Li-batteries

D3.6 – Report on validation of recovered materials re-use on new cells

Due date of deliverable	**Actual submission date:**	Organisation name responsible for this deliverable: SAKARYA
31/08/2024	27/09/2024	

Dissemination Level

SEN	Sensitive	X
PU	Public	

Project Acronym
FREE4LIB

Grant Agreement No.
101069890

Project Start Date
01-09-2022

Project End Date
31-08-2026

Duration
48 months

Views and opinions expressed are those of the author(s) only and do not necessarily reflect those of the European Union or CINEA. Neither the European Union nor the granting authority can be held responsible for them. This project has received funding from Horizon Europe research and innovation programme under Grant Agreement No.1069890

Disclaimer

©2022 FREE4LIB Consortium Partners. All rights reserved.

Free4lib is an EU-funded project that has received funding from the European Union's Horizon Europe research and innovation programme under grant agreement no. 101069890. The sole responsibility for the content of this report lies with the authors. It does not necessarily reflect the opinion of the European Union. The European Commission is not responsible for any use that may be made of the information contained therein.

While this publication has been prepared by the consortium partners of the project, the authors provide no warranty with regards to the content and shall not be liable for any direct, incidental or consequential damages that may result from the use of the information or the data contained therein.

Versions

DATE	VERSION	AUTHOR	COMMENT
13/09/2024	1	SAKARYA, NESSTEC, IREC, LUREDERRA, TORRECID,	first draft of the document
19/09/2024	2	SAKARYA	Comments from WP3
25/09/2024	3	SAKARYA, LUREDERRA	Comments from CSIC, LUREDERRA
26/09/2024	4	CARTIF	Final document

Contents

Views and opinions expressed are those of the author(s) only and do not necessarily reflect those of the European Union or CINEA. Neither the European Union nor the granting authority can be held responsible for them. This project has received funding from Horizon Europe research and innovation programme under Grant Agreement No.1069890

Funded by the European Union

Views and opinions expressed are those of the author(s) only and do not necessarily reflect those of the European Union or CINEA. Neither the European Union nor the granting authority can be held responsible for them. This project has received funding from Horizon Europe research and innovation programme under Grant Agreement No.1069890

List of Abbreviations

ACRONYMS	DESCRIPTION
BM	Black Mass
cP	Centipoise
DMC	Dimethyl carbonate
EC	Ethylene carbonate
EDS	Energy Dispersive X-ray Spectroscopy
EOL	End-of-Life
EV	Electric Vehicle
FSP	Flame Spray Pyrolysis
FTIR	Fourier Transform Infrared spectroscopy
ICP	Inductively Coupled Plasma Spectroscopy
LIB	Lithium-ion batteries
LTO	$Li_4Ti_5O_{12}$
MEVVA	Metal vacuum vapor arc
NMA	$LiNi_{0.8}Mn_{0.15}Al_{0.05}O_2$
NMC 622	$LiNi_{0.6}Mn_{0.2}Co_{0.2}O_2$
NMC 811	$LiNi_{0.8}Mn_{0.1}Co_{0.1}O_2$
PSDs	Particle Size Distributions
PVDF	Poly(vinylidene fluoride)
SEM	Scanning Electron Microscopy
TRL	Technology Readiness Level
wt. %	Weight percent
XRD	X-Ray Diffraction

Views and opinions expressed are those of the author(s) only and do not necessarily reflect those of the European Union or CINEA. Neither the European Union nor the granting authority can be held responsible for them. This project has received funding from Horizon Europe research and innovation programme under Grant Agreement No.1069890

1. Executive summary

This deliverable presents the feasibility of the new active anode and cathode materials obtained after different recycling technologies. To general inspection for each material, the morphological and chemical characterisation studies are realized, to understand the microstructural evolution and phase identification by SEM, EDS and XRD. Battery performances of materials with suitable microstructure and phase at coin-cell level is investigated and the performances were compared via galvanostatic charge/discharge test, CVs and impedances. To scaling up the suitable materials, the developing pf pouch cell is used.

The obtained results will be using for pilot-scale production of the LIBs in the pouch-cell levels at WP4.

2. Introduction

In recent years, the European electric vehicle (EV) market has experienced significant growth. Since the early 2020s, there has been a notable increase in EV adoption, driven by the European Union's targets to reduce carbon emissions. The EU has set a goal to cut emissions by 55% by 2030 compared to 1990 levels, which has led to various incentives and regulations promoting electric vehicles. By 2023, electric vehicle sales accounted for 20% of total car sales in Europe, reflecting an annual increase. Countries such as Germany, Norway, and the United Kingdom are among the leaders in the European market, benefiting from advanced charging infrastructure and supportive government policies. The expansion of the electric vehicle market is supported by advancements in battery technology and government incentives. Consequently, the European electric vehicle market is expected to continue growing, with an increasing share in the automotive sector.

Efforts to reduce the amount of cobalt in electric vehicle batteries have become increasingly important due to environmental and ethical concerns. Cobalt is a critical component in lithium-ion batteries, enhancing their energy density. However, cobalt mining is often associated with significant environmental damage and social issues, particularly in the Democratic Republic of Congo, where mining practices raise concerns about child labour and poor working conditions. In response to these challenges, researchers and battery manufacturers are developing alternative battery chemistries that minimize cobalt content. For instance, high-nickel batteries and solid-state battery technologies reduce the reliance on cobalt while potentially lowering costs and improving performance. Additionally, advancements in battery recycling technologies offer further potential to decrease cobalt demand. These strategies represent crucial steps toward enhancing the sustainability of the electric vehicle industry and mitigating its environmental impact.

Battery recycling for electric vehicles is critical for both environmental and economic sustainability. Lithium-ion batteries, commonly used in electric vehicle, energy storage systems, contain valuable metals such as lithium, cobalt, and nickel. Recovering these metals through recycling can reduce the need for new mining and mitigate environmental impacts. The recycling process involves the disassembly and processing of battery components, which not only facilitates the efficient recovery of battery materials but also helps manage hazardous waste. Advanced recycling technologies enable the effective reuse of metals like lithium and nickel, minimizing material loss at the end of battery life. Additionally, recycling can lower costs and reduce the demand for raw materials needed for new battery production. In this context, advancing battery-recycling technologies is a crucial step in enhancing the environmental sustainability of electric vehicles and promoting a circular economy.

In the context of the FREE4LIB project, precursors derived from end-of-life lithium-ion batteries were synthesized in LNMO, NMC622, and NMC811 stoichiometry's using various methodologies, including flame pyrolysis, ion implantation, hydrothermal processing, and solid-state synthesis. The physicochemical and electrochemical properties of these precursors were assessed, and the scalability of the processes was evaluated based on the results obtained.

The findings from our laboratory-scale studies, as detailed in this report, indicate that certain products derived from recycled powders can achieve performance levels comparable to commercial NMC materials and demonstrate potential for scalable production.

3. Electrochemical and morphological investigation of recovered materials synthesised by Flame Spray Pyrolysis

One of the cathode production routes considered on the FREE4LIB project, is the Flame Spray Pyrolysis (FSP). The FSP is an innovative and industrially scalable technology, which let the production of different metal oxide compositions on the nano-scale. The process consists of introducing a liquid precursor mixture into a combustion chamber through an atomizer, which disperse the mixture forming small droplets. These droplets burn in the flame creating the nanoparticles.

This route can be divided into several stages, including the preparation of the precursor mixture with the desired cations; the definition of the technical parameters, the collection of material and characterisation; and the optimisation of the process if needed. All these steps are summarized on the Figure 1.

Funded by the European Union

Views and opinions expressed are those of the author(s) only and do not necessarily reflect those of the European Union or CINEA. Neither the European Union nor the granting authority can be held responsible for them. This project has received funding from Horizon Europe research and innovation programme under Grant Agreement No.1069890

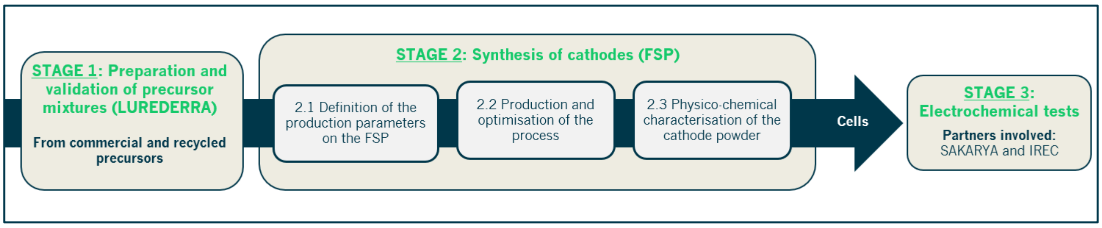

Figure 1. General overview of the process.

The central point of this study is synthesising cathode materials with recycled precursors. Nevertheless, due to the complexity of the process, initial productions have been carried out with commercial precursors, in order to identify possible critical points or aspects that would need an optimisation, before introducing recycled materials. In parallel, D3.3. compiles all the activities done with recycled precursors and the different goals and recycled precursor mixtures obtained.

According to the cathode synthesis, the pre-selected compounds on FREE4LIB project were LMNO, NMC622 and NMC811. Lurederra produced several batches, NMC622, Li-NMC811 and an optimisation of this last composition.

3.1 NMC 622 cathode powder synthesised by Flame Spray Pyrolysis

To produce NMC622 nanomaterial on the FSP equipment, LUREDERRA started with the preparation of the precursor mixture. Metallic precursors of each of the metals included on the composition (nickel, manganese, and cobalt) from different natures (organometallic, inorganic) were studied, as well as, testing their compatibility in different medias and between them. All these actions resulted in a couple of precursor mixtures that were validated concerning their calorimetry properties, viscosity, and stability in time (Figure 2).

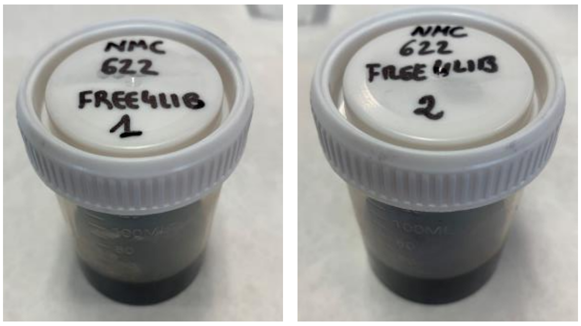

Figure 2. Examples of most representative NMC622 precursor mixtures.

On the following table (Table 1), the main properties of both precursor mixtures are compiled. After analysing the characteristics, "precursor mixture 1" was selected, as it has a lower calorimetry property what would support the "lower temperature" required on this type of nanoparticle productions. Additionally, the viscosity is in a good range.

Funded by the European Union

Views and opinions expressed are those of the author(s) only and do not necessarily reflect those of the European Union or CINEA. Neither the European Union nor the granting authority can be held responsible for them. This project has received funding from Horizon Europe research and innovation programme under Grant Agreement No.1069890

Table 1. Characterisation of the precursor mixtures.

Precursor mixture	Calorimetry (cal g^{-1})	Viscosity (cP)	Stability
1	6545	7.81	OK
2	7051	5.08	OK

Next, production parameters were defined and settled on the equipment. Along the injection of the precursor mixture, several adjustments were done with the purpose of getting a stable and non-stop flame. Main modifications were carried out on precursor mixture flow, combustion gas flows, fan power and pressure of the nozzle. As shown on Figure 3, those modifications let a uniform combustion flame.

Figure 3. Laboratory FSP equipment, different flame morphologies and cathode powder collected.

In order to validate the production process, a small batch of material was collected on the specific filters and characterised. LUREDERRA performed a BET analysis (Figure 4), getting a surface area of 36.5 $m^2 g^{-1}$, which estimates an average particle size of 31.7 nm; and a mass loss on ignition, resulting on around 4.5%.

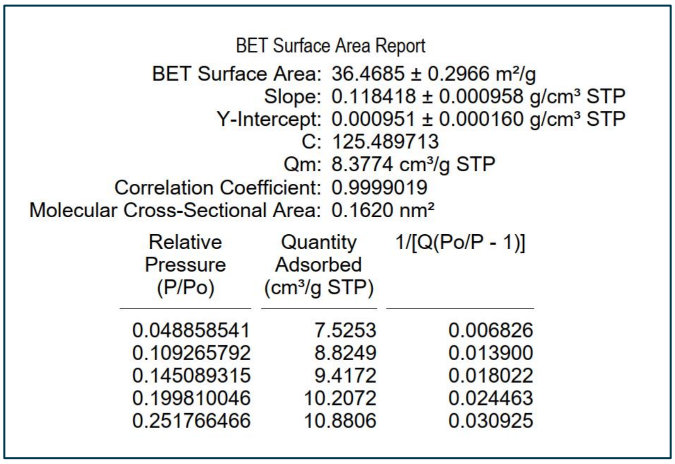

```
                        BET Surface Area Report
                   BET Surface Area:  36.4685 ± 0.2966 m²/g
                              Slope:  0.118418 ± 0.000958 g/cm³ STP
                        Y-Intercept:  0.000951 ± 0.000160 g/cm³ STP
                                  C:  125.489713
                                 Qm:  8.3774 cm³/g STP
            Correlation Coefficient:  0.9999019
     Molecular Cross-Sectional Area:  0.1620 nm²

                  Relative      Quantity     1/[Q(Po/P - 1)]
                  Pressure      Adsorbed
                   (P/Po)     (cm³/g STP)
                ----------    ----------    ------------
                0.048858541      7.5253        0.006826
                0.109265792      8.8249        0.013900
                0.145089315      9.4172        0.018022
                0.199810046     10.2072        0.024463
                0.251766466     10.8806        0.030925
```

Figure 4. BET analysis of NMC622 powder.

On the other hand, SAKARYA/NESSTEC and IREC partners completed the characterisations. The physico-chemical properties of the synthesised cathode powder were compared with the commercial one. Morphological analysis was carried out by Scanning Electron Microscope; and phase and elemental analysis of the powders were analysed by XRD and EDS techniques.

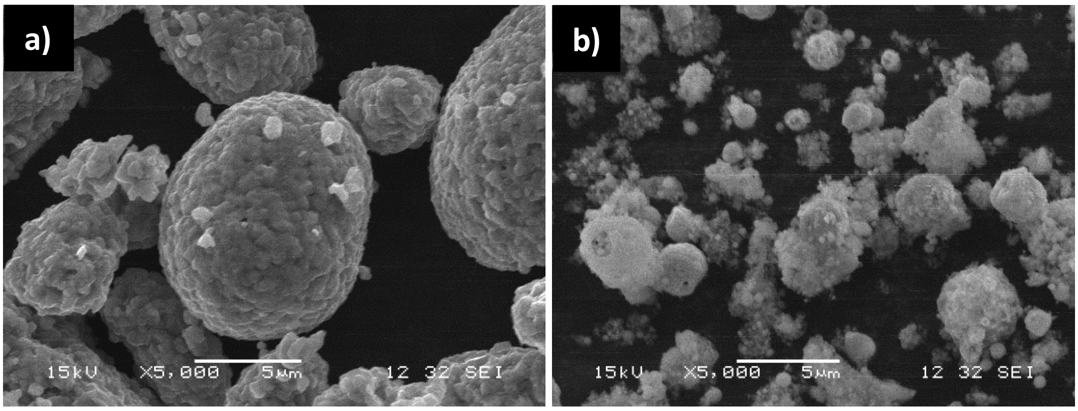

Figure 5. The SEM images of a) commercial NMC622 and b) CPO11 powders.

Morphology of the commercial NMC622 powder is illustrated in Figure 5a. The commercial NMC622 particles form aggregates that exhibit dense packing and consist of relatively small primary particles. These aggregates display a uniform size distribution, with particle sizes ranging from 5 to 10 µm. In contrast, the CPO11 sample demonstrates a broader size distribution at the nanoscale to microscale. As depicted in Figure 5b, the microstructure of CPO11 differs significantly from that of the commercial NMC622, indicating distinct characteristics between the two materials.

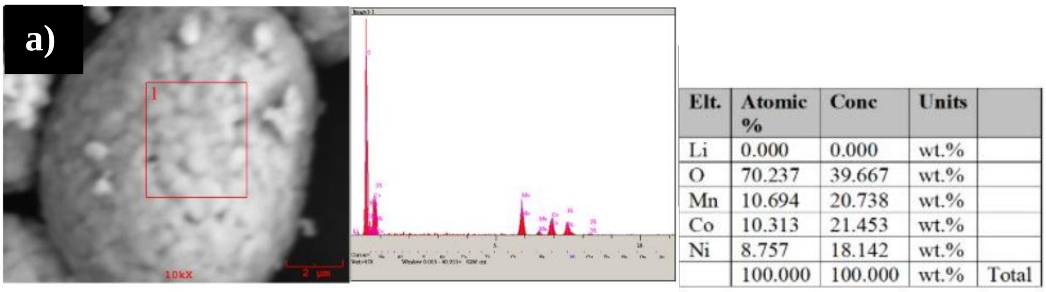

Elt.	Atomic %	Conc	Units	
Li	0.000	0.000	wt.%	
O	70.237	39.667	wt.%	
Mn	10.694	20.738	wt.%	
Co	10.313	21.453	wt.%	
Ni	8.757	18.142	wt.%	
	100.000	100.000	wt.%	Total

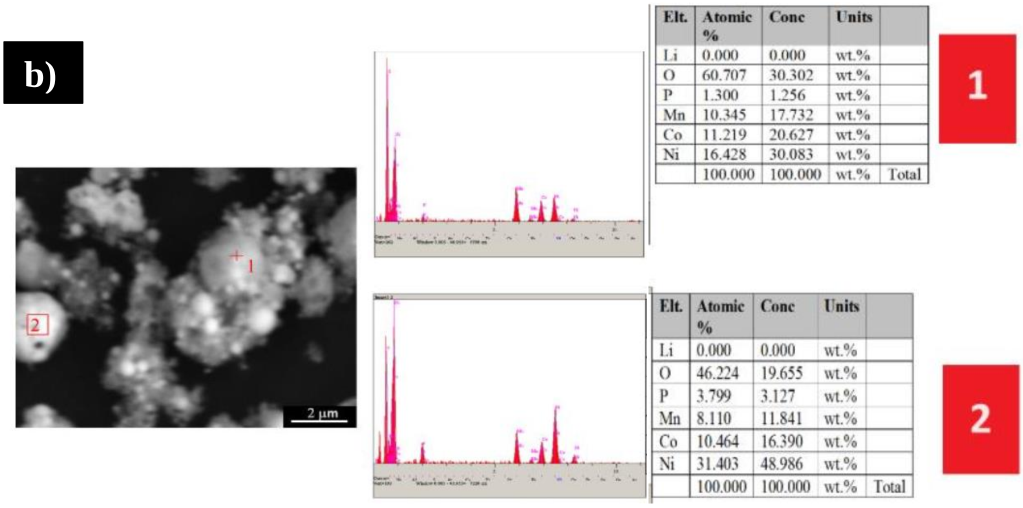

Elt.	Atomic %	Conc	Units	
Li	0.000	0.000	wt.%	
O	60.707	30.302	wt.%	
P	1.300	1.256	wt.%	
Mn	10.345	17.732	wt.%	
Co	11.219	20.627	wt.%	
Ni	16.428	30.083	wt.%	
	100.000	100.000	wt.%	Total

Elt.	Atomic %	Conc	Units	
Li	0.000	0.000	wt.%	
O	46.224	19.655	wt.%	
P	3.799	3.127	wt.%	
Mn	8.110	11.841	wt.%	
Co	10.464	16.390	wt.%	
Ni	31.403	48.986	wt.%	
	100.000	100.000	wt.%	Total

Figure 6. EDS results of a) commercial NMC622 and b) CPO11 powders.

Although EDS results may not provide precise measurements comparable to ICP results (e.g., inability to measure lithium content, lower sensitivity), they can offer a general understanding of the elements present within the particles. The EDS findings displayed in Figure 6 illustrate the elemental composition of the commercial NMC622 and CPO11 sample particles. In Figure 6a, the EDS analysis of the commercial NMC622 powder shows the presence of O, Ni, Co, and Mn elements exclusively. Conversely, when examining the EDS results for the CPO11 sample (Figure 6b), in addition to O, Ni, Co, and Mn, the detection of phosphorus (P) is observed. The presence of phosphorous could be attributed to the commercial precursors used, as the majority (especially organometallics) have additives in their compositions.

In Figure 7, XRD spectra for commercial NMC622 and CPO11 samples are presented. Upon examination of the XRD spectrum for commercial NMC622 powders, a consistent pattern emerges, aligning with literature data. However, it is evident from the figure that the XRD spectra of the CPO11 sample are discordant with those of commercial NMC622.

Views and opinions expressed are those of the author(s) only and do not necessarily reflect those of the European Union or CINEA. Neither the European Union nor the granting authority can be held responsible for them. This project has received funding from Horizon Europe research and innovation programme under Grant Agreement No.1069890

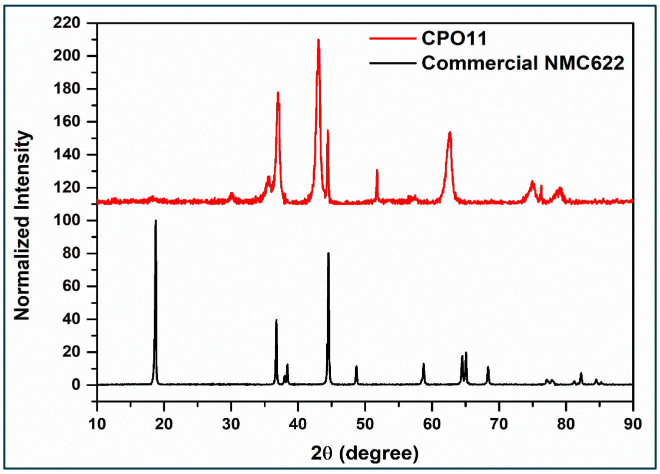

Figure 7. XRD spectrum of commercial NMC622 and CPO11 sample powders.

Although the exact crystal phase required was not achieved, several mixed phases were achieved so, as preliminary review of the properties of the nanomaterial obtained, the electrochemical tests were done. The electrode preparation parameters (PVDF, carbon black and active material amount), coin cell assembling conditions (coin cell type, electrolyte volume, separator type) and electrochemical test conditions are given in Table 2.

Table 2. Electrode preparation, coin cell assembling and electrochemical test conditions for commercial NMC 622 and CPO11 samples

NMC622 and CPO11 electrode test specifications		
Electrode preparation	Binder type and amount	PVDF – 5, 7.5 wt%
	Carbon black amount	Super P – 5wt%
	Active material amount	87.5-90wt.%
	Electrode thickness	Wet thickness ~300 µm
	Loading (mg/cm^2)	~5 mg/cm^2
Coin cell assembly	Coin cell type	2032
	Electrolyte type and volume	60 µl of 1M $LiPF_6$ in EC:DMC
	Half-cell or full-cell	Half-cell
	Separator	Celgard 2400
Electrochemical tests	Charge/discharge test parameters	Voltage range: 4.2-2.7 V vs. Li/Li$^+$ Current: C/20

Funded by the European Union

Views and opinions expressed are those of the author(s) only and do not necessarily reflect those of the European Union or CINEA. Neither the European Union nor the granting authority can be held responsible for them. This project has received funding from Horizon Europe research and innovation programme under Grant Agreement No.1069890

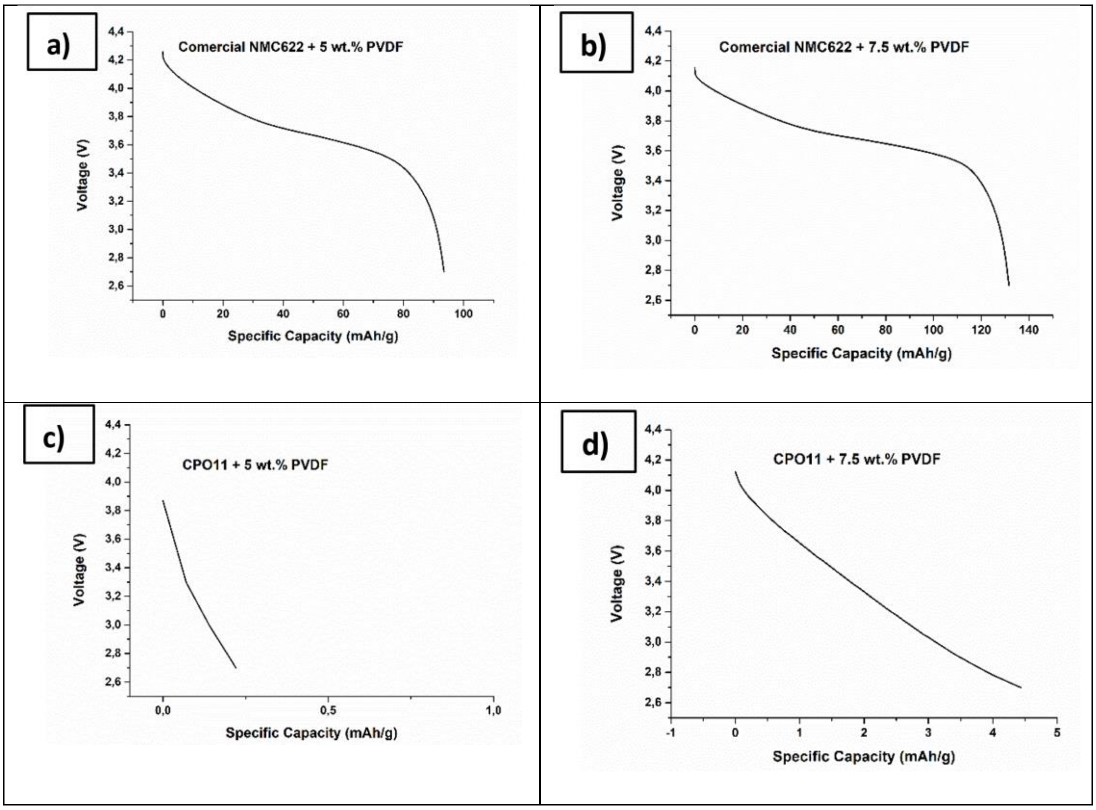

Figure 8. First discharge curves of a) commercial NMC622+5wt.%PVDF, b) commercial NMC622+7.5wt.%PVDF, c) CPO11+5wt.%PVDF and d) CPO11+7.5wt.%PVDF.

Figure 8 illustrates the first discharge curves for both commercial NMC622 and CPO11 samples, which were prepared with varying PVDF percentages of 15 wt.% and 7.5 wt.%. The commercial NMC622 electrode exhibits enhanced specific capacity performance with increased PVDF content. Regrettably, the CPO11 electrodes fail to demonstrate any specific capacity, even with a higher PVDF content. This indicates that the CPO11 sample did not operate electrochemically as expected.

With the complete characterization of the material, the following observations have been identified and extracted:

- SEM images showed smaller particle sizes in FSP produced material than in commercial one.

- EDX analysis found impossible to identify lithium neither in commercial nor in produced one, due to its low sensitivity.

- XRD spectra identified crystalline mixed oxide phases (lithium-cobalt, nickel manganese…), but not the exactly desired NMC crystal phase.

All these comments have been analysed to get guidelines to optimize the following cathode productions. In that sense, next production was a Li-NMC811 and the main optimization was focused on increasing the lithium content, get more homogeneous particle size, in order to

Views and opinions expressed are those of the author(s) only and do not necessarily reflect those of the European Union or CINEA. Neither the European Union nor the granting authority can be held responsible for them. This project has received funding from Horizon Europe research and innovation programme under Grant Agreement No.1069890

have a better distribution of the different elements; and this modification could let to an increase on the electrochemical performance.

3.2 NMC 811 cathode powder synthesised by Flame Spray Pyrolysis

As mentioned before, the second cathode composition was Li-NMC811, and it was also produced from commercial precursors. Following a similar methodology as in the previous production, a precursor mixture was prepared and validated (Figure 9). After testing the behaviour and complementarity of metallic precursors in the same media, lithium content was increased to compensate the expected sublimation during combustion in the FSP equipment.

Figure 9. Precursor mixture preparation: 1,2, and 3) Step-by-step integration of each of the metal precursors in the same media; and 4) final precursor mixture.

The final precursor mixture had a calorimetry of 6295 cal g^{-1}, a viscosity of 1.65 cP and a good stability over time. With the validation of these characteristics, LUREDERRA proceeded with the adjustment of the production parameters and a small quantity of material was collected (Figure 10c).

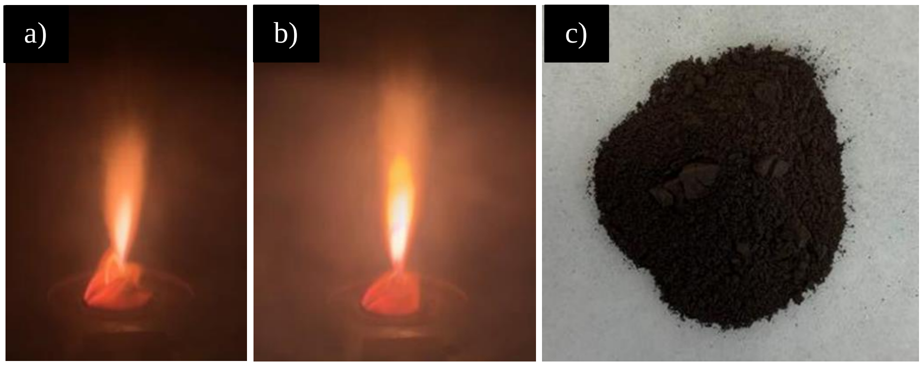

Figure 10. FSP production process: a) and b) optimisation of the flame morphology; and c) Li-NMC811 powder collected.

Funded by the European Union

Views and opinions expressed are those of the author(s) only and do not necessarily reflect those of the European Union or CINEA. Neither the European Union nor the granting authority can be held responsible for them. This project has received funding from Horizon Europe research and innovation programme under Grant Agreement No.1069890

Concerning the physico-chemical characterisations, within this production, a reduction of the particle size was achieved, getting a higher surface area, 53.83 $m^2\ g^{-1}$, and a lower loss on ignition, 1%.

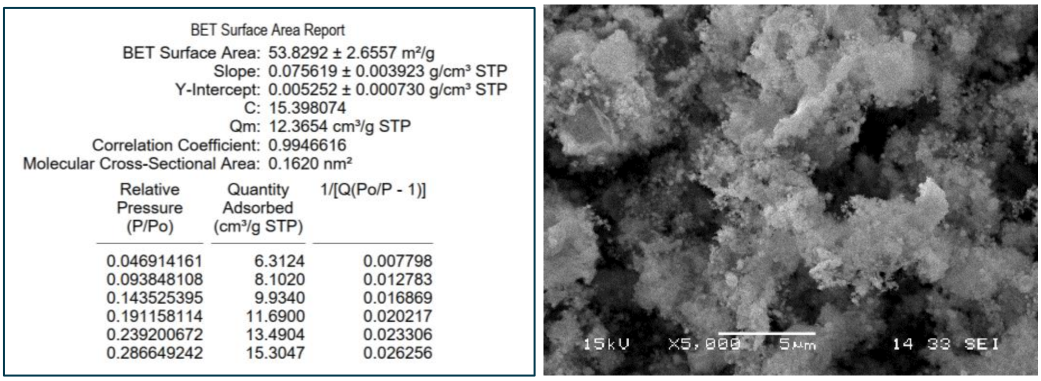

BET Surface Area Report
BET Surface Area: 53.8292 ± 2.6557 m²/g
Slope: 0.075619 ± 0.003923 g/cm³ STP
Y-Intercept: 0.005252 ± 0.000730 g/cm³ STP
C: 15.398074
Qm: 12.3654 cm³/g STP
Correlation Coefficient: 0.9946616
Molecular Cross-Sectional Area: 0.1620 nm²

Relative Pressure (P/Po)	Quantity Adsorbed (cm³/g STP)	1/[Q(Po/P - 1)]
0.046914161	6.3124	0.007798
0.093848108	8.1020	0.012783
0.143525395	9.9340	0.016869
0.191158114	11.6900	0.020217
0.239200672	13.4904	0.023306
0.286649242	15.3047	0.026256

Figure 11. BET report and SEM image of Li-NMC811 cathode powder (CPO33).

On *Figure 11*, it is shown a SEM image of the second composition of active powder synthesised. It showed a smaller particle size in the range of the submicron to nanometer scales compared to the one obtained with commercial NMC622 and CPO11 (NMC622 synthesized by FSP). EDS analysis (*Figure 12*) resulted on the identification of some elements such as Zn, P, Al and Si. In the same way as the previous material (NMC622), phosphorous was present. It is supposed to avoid it when producing with recycled precursors.

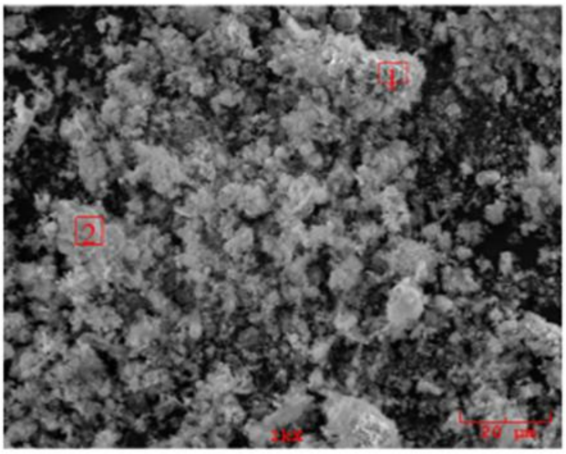

Funded by the European Union

Views and opinions expressed are those of the author(s) only and do not necessarily reflect those of the European Union or CINEA. Neither the European Union nor the granting authority can be held responsible for them. This project has received funding from Horizon Europe research and innovation programme under Grant Agreement No.1069890

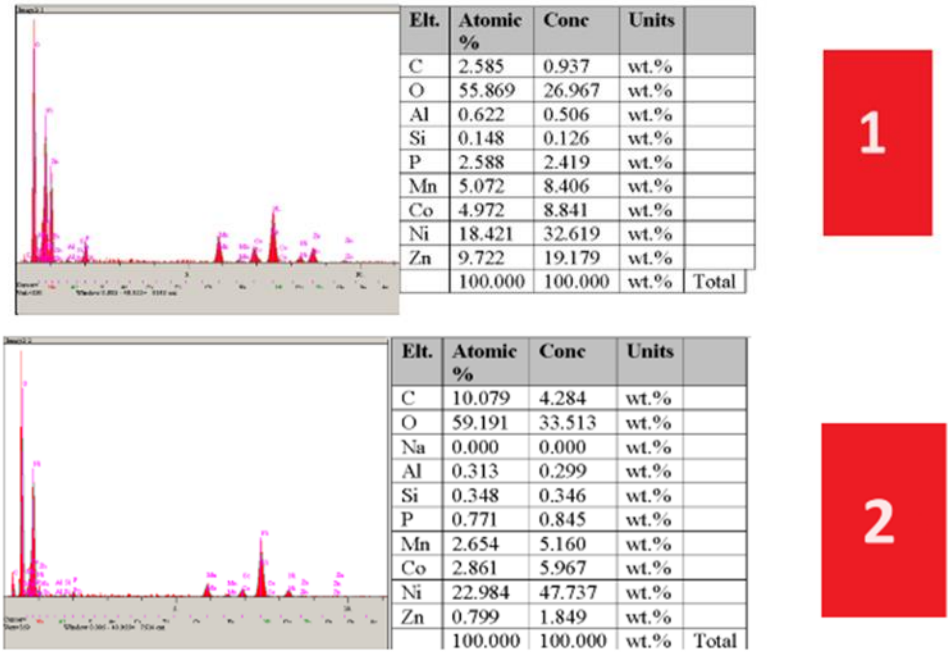

Elt.	Atomic %	Conc	Units	
C	2.585	0.937	wt.%	
O	55.869	26.967	wt.%	
Al	0.622	0.506	wt.%	
Si	0.148	0.126	wt.%	
P	2.588	2.419	wt.%	
Mn	5.072	8.406	wt.%	
Co	4.972	8.841	wt.%	
Ni	18.421	32.619	wt.%	
Zn	9.722	19.179	wt.%	
	100.000	100.000	wt.%	Total

Elt.	Atomic %	Conc	Units	
C	10.079	4.284	wt.%	
O	59.191	33.513	wt.%	
Na	0.000	0.000	wt.%	
Al	0.313	0.299	wt.%	
Si	0.348	0.346	wt.%	
P	0.771	0.845	wt.%	
Mn	2.654	5.160	wt.%	
Co	2.861	5.967	wt.%	
Ni	22.984	47.737	wt.%	
Zn	0.799	1.849	wt.%	
	100.000	100.000	wt.%	Total

Figure 12. EDS result of CPO33 powder.

The phase structure of the powder is Li_2CO_3, $NiMn_2O_4$ and $Li_{.185}Co_{.815}O$ (cubic phase) phases. It is evident from Figure 13 that the XRD spectra of the CPO11 and CPO33 sample are discordant with those of commercial NMC622.

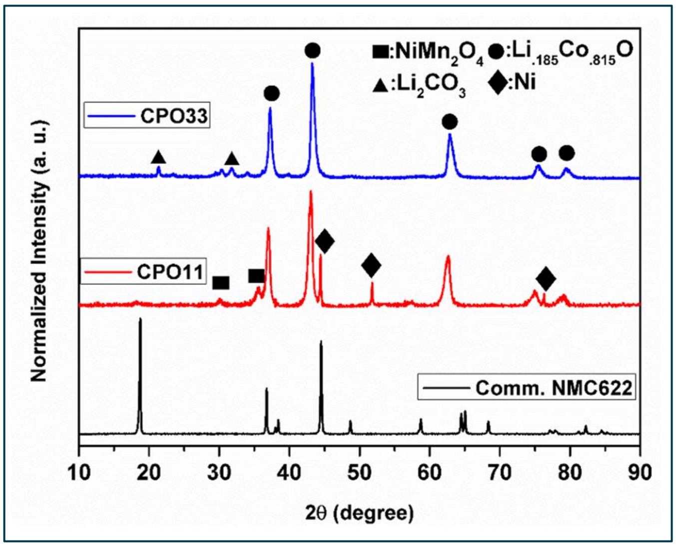

Figure 13. XRD spectrum comparison of commercial NMC622, CPO11 and CP033 sample powders.

As the desired crystal phase was not achieved, in this case, the electrochemical charge/discharge tests were not conducted. A detailed study on the production process requirements was done, trying to understand and identify the optimization points.

Funded by the European Union

Views and opinions expressed are those of the author(s) only and do not necessarily reflect those of the European Union or CINEA. Neither the European Union nor the granting authority can be held responsible for them. This project has received funding from Horizon Europe research and innovation programme under Grant Agreement No.1069890

3.3 Production optimisation studies for NMC 811 by Flame Spray Pyrolysis

Taking into consideration all the results obtained on the two previous productions, Lurederra decided to optimise this second composition. Firstly, modifications on the precursor mixture were done looking for a lower calorimetry, which would directly imply a colder flame. The strategy followed to reach a colder precursor mixture, was centred on using inorganic-based precursors, as well as, including a specific percentage of water on the media (*Figure 14*).

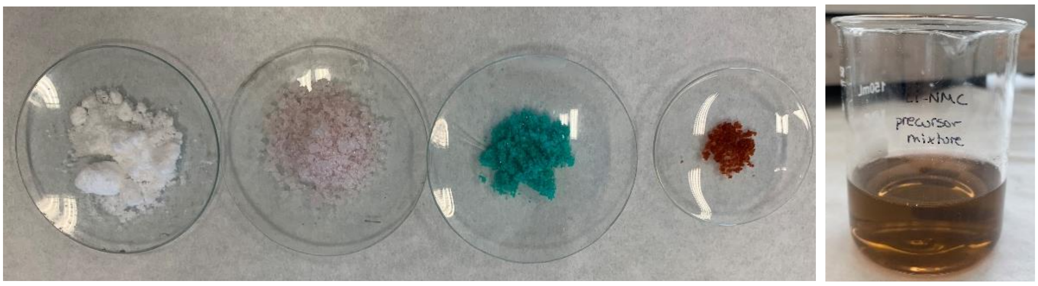

Figure 14. Inorganic metal precursors, lithium, manganese, nickel, and cobalt, respectively. Final precursor mixture prepared.

The final precursor mixture was characterized getting a calorimetry of 241 cal g^{-1} and a viscosity of 2.4 cP. A clear reduction on the combustion capacity was achieved. Parameters of the FSP equipment were defined and a small batch of material was produced and collected to carry out a preliminary analysis of its physico-chemical properties. The material collected was wet, so a light drying was required. Then, harder thermal conditions were used trying to achieve the desired crystal phase.

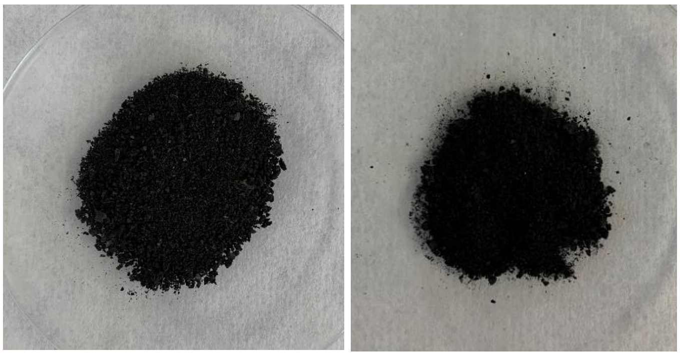

Figure 15. Optimized Li-NMC811 powder produced, 1) after light drying and 2) after thermal treatment.

Table 3. BET analysis results from both optimised Li-NMC811 powders.

Optimised Li-NMC811	Surface area ($m^2 g^{-1}$)	Estimated particle size
Drying 80ºC	1.68	805 nm
Thermal conditions 800ºC	1.19	1.1 µm

Funded by the European Union

Views and opinions expressed are those of the author(s) only and do not necessarily reflect those of the European Union or CINEA. Neither the European Union nor the granting authority can be held responsible for them. This project has received funding from Horizon Europe research and innovation programme under Grant Agreement No.1069890

An IR analysis of both materials was done looking for a modification of the material after the thermal post-processing. As shown on the figure below (Figure 16), clear differences on the peaks detected are visualized, meaning that a transformation of the material structure might have been occurred. An XRD essay would confirm this modification.

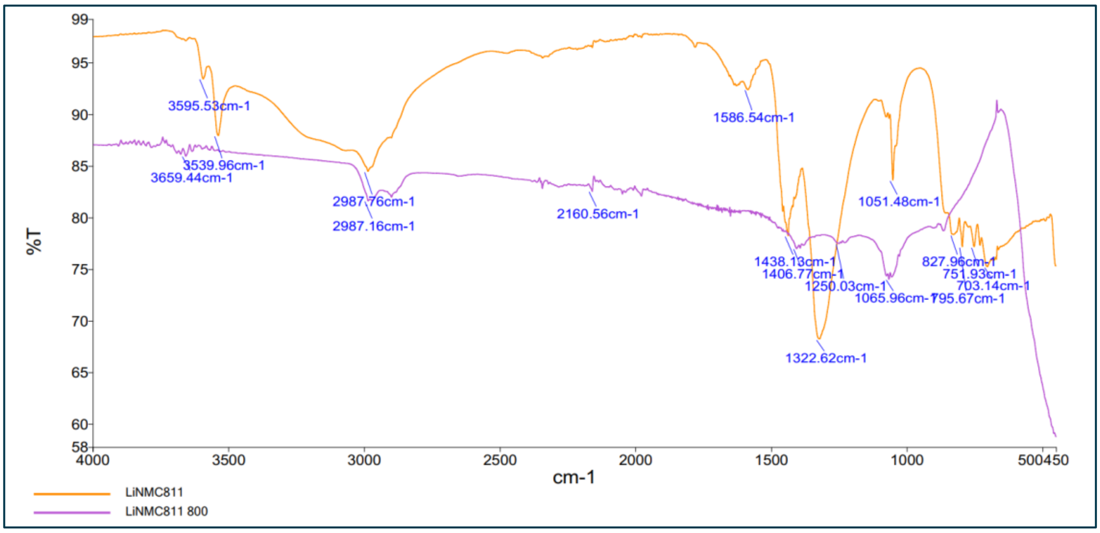

Figure 16. IR spectra. Yellow: dried powder; and pink: powder after thermal treatment.

This material was sent to IREC to carry out an XRD essay. Results obtained are showed on the following figure. In Figure 17, we can see the diffractogram of the experimental sample (CPO44) compared with the diffraction pattern of NMC811, and we can observe the coincidence of the 2θ peak positions with respect to the pattern.

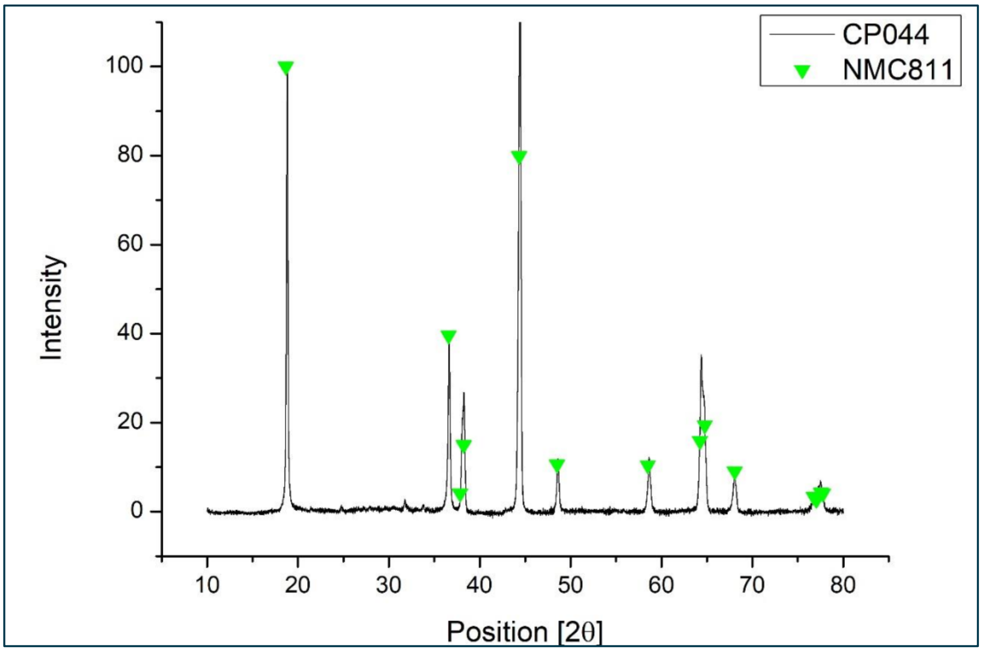

Figure 17. XRD spectra of material CPO44.

Funded by the European Union

Views and opinions expressed are those of the author(s) only and do not necessarily reflect those of the European Union or CINEA. Neither the European Union nor the granting authority can be held responsible for them. This project has received funding from Horizon Europe research and innovation programme under Grant Agreement No.1069890

4. The electrochemical and physical investigation NMA and LTO electrodes produced by ion implantation processes

4.1 Results

In order to increase the performance of the batteries, EURECAT has performed different ion implantation processes on new cathode and anode electrodes provided by IREC. The surface treatments were carried out by means of MEVVA (Metal Vacuum Vapor Arc) ion implantation technique. Nb, C and Al pure cathodes were evaporated using a pulsed cathodic arc source (MEVVA50, Plasma Technology Limited, Hong Kong, Figure 18). The acceleration ion implantation voltage was ranged between 15 and 30 kV. The incident ion-implanted dose was explored in the range of $9.6{\cdot}10^{13}$ to $9.1{\cdot}10^{16}$ ions/cm^2.

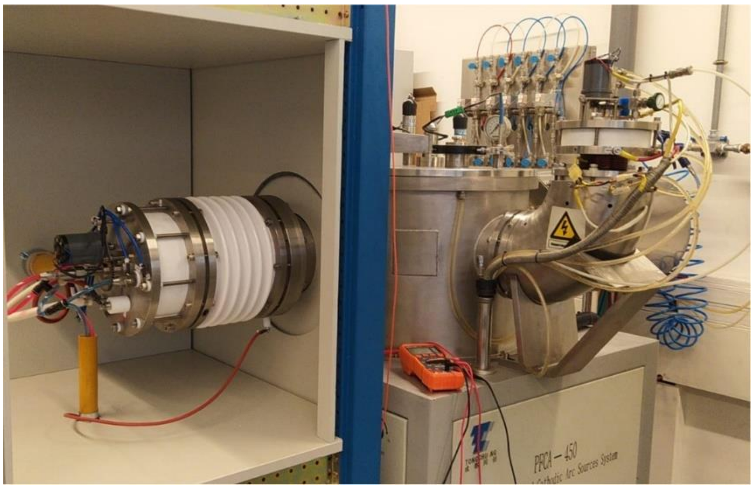

Figure 18. MEVVA ion implantation equipment of EURECAT.

Niobium ion implantation processes

The first ion implantation trials were performed on both NMA/Al cathodes and LTO/Cu anodes, the description of which is as follows:

(a) Electrode cathode: NMA/Al

- Active material: Lithium nickel manganese aluminum oxide [$LiNi_{0.8}Mn_{0.15}\,Al_{0.05}O_2$].
- Electrode composition: 85 wt.% Active material + 10 wt.% Carbon + 5 wt. % PVDF binder.
- Coated on Aluminum foil (18 µm thickness).
- Total thickness: 40-45 µm.
- The weight of deposited material is around 3.5 mg/cm^2.

Funded by the European Union

Views and opinions expressed are those of the author(s) only and do not necessarily reflect those of the European Union or CINEA. Neither the European Union nor the granting authority can be held responsible for them. This project has received funding from Horizon Europe research and innovation programme under Grant Agreement No.1069890

(b) Electrode anode: LTO/Cu

- Active material: Lithium titanate oxide ($Li_4Ti_5O_{12}$).
- Electrode composition (wt.% active, carbon, binder): about 4 mg/cm^2 of deposited material 85% is LTO, 10% carbon SuperP, 5% PVDF binder.
- Coated on copper foil.
- Loading: theoretical loading is 175mAh/g of LTO, experimental loading is 150mAh g^{-1} of LTO at C/10-rate.
- Thickness: measured layer thickness ranges between 35-40 µm.

Subsequent ion implantation processes were limited to the LTO/Cu anodes. The niobium ion implantation treatments were performed according to the process parameters shown in Table 4.

Table. 4. Process parameters of Nb ion implantation treatments.

Process	Ion implanted	Samples	Treatment time (min.)	Accelerating voltage (kV)	Ion dose (1/cm^2)
025-22	Nb	NMA/Al, LTO/Cu	85	30	$4.28\cdot10^{16}$
026-22	Nb	NMA/Al, LTO/Cu	75	30	$7.55\cdot10^{16}$
027-22	Nb	NMA/Al, LTO/Cu	90	30	$9.06\cdot10^{16}$
028-22	Nb	NMA/Al, LTO/Cu	40	30	$4.03\cdot10^{16}$
029-22	Nb	NMA/Al, LTO/Cu	47	30	$4.44\cdot10^{16}$
030-22	Nb	NMA/Al, LTO/Cu	25	30	$2.52\cdot10^{16}$
031-22	Nb	NMA/Al, LTO/Cu	95	30	$1.35\cdot10^{16}$
008-23	Nb	LTO/Cu	60	20	$2.64\cdot10^{15}$
009-23	Nb	LTO/Cu (2 sccm of O2 added during this process)	60	20	$2.64\cdot10^{15}$

Figure 19 shows the surface morphology of NMA/Al and LTO/Cu electrodes before and after the ion implantation process 026-22. As can be seen, the ion implantation treatment has induced significant morphological changes, resulting in fusion and coalescence of the original polycrystalline morphology.

Funded by the European Union

Views and opinions expressed are those of the author(s) only and do not necessarily reflect those of the European Union or CINEA. Neither the European Union nor the granting authority can be held responsible for them. This project has received funding from Horizon Europe research and innovation programme under Grant Agreement No.1069890

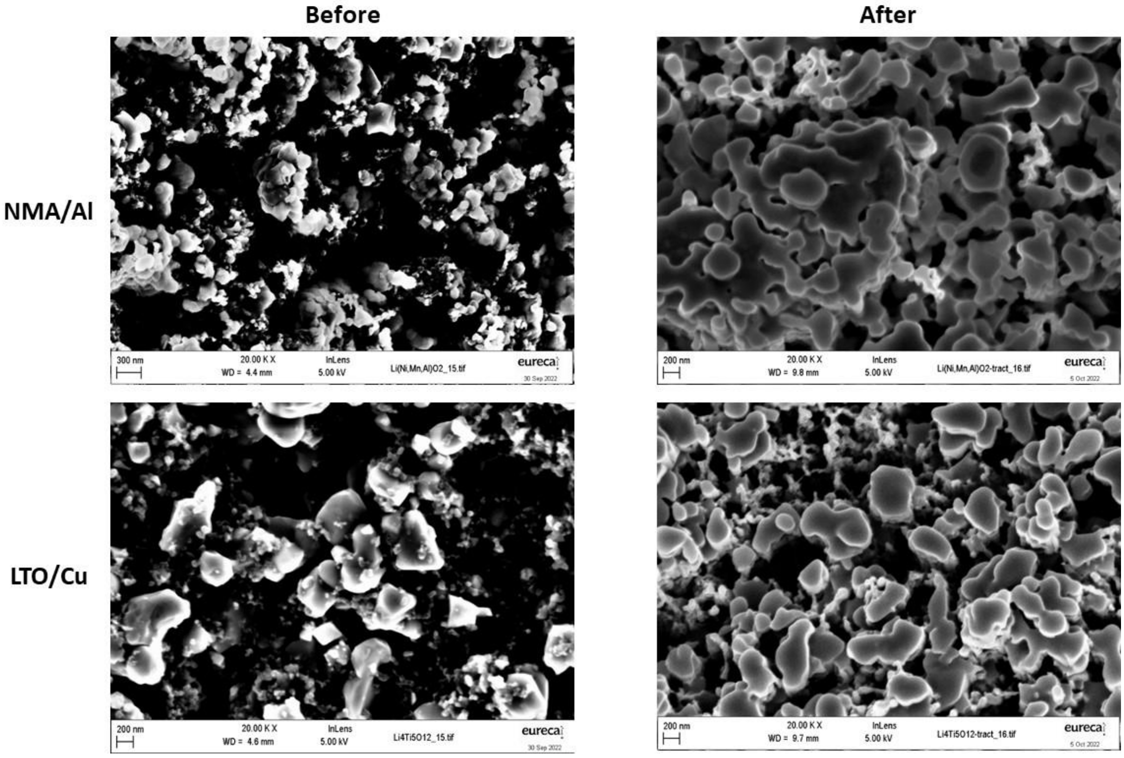

Figure 19. Scanning Electron Microscopy (SEM) images of NMA/Al and LTO/Cu electrodes before and after the 026-22 niobium ion implantation process.

The chemical composition analysis performed by Energy Dispersive X-ray Spectroscopy (EDS) shows a surface concentration of Nb around 1.5 %atomic.

Some selected samples (processes: 027-22, 029-22, 031-22) from Table 4 were tested electrochemically in half-cell, and results are presented in Figure 20. Results for LTO are included for comparison. In the discharge capacity plots, baseline sample delivers high theoretical capacity of 175 mAhg^{-1} and treated samples lower capacities of 120 – 140 mAh g^{-1} at C/10 depending on processing condition, Figure 20a. There is no trend between processing conditions and discharge capacity. Regarding the C-rate capability test, Figure 20b, baseline sample delivers a discharge capacity of 100 mAh g^{-1} at 2C, while in treated samples high current performance is decreased delivering capacities in the range of 70-40 mAh g^{-1}. As above, there is no trend between sample processing conditions and discharge capacity at high current. Overall, Nb ion implantation does not improve LTO performance at any current rate. We hypothesise that Nb ion implantation using processing conditions defined in Table 4 blocks Li^{+} diffusivity at the electrode level limiting discharge capacity and C-rate performance.

Funded by the European Union

Views and opinions expressed are those of the author(s) only and do not necessarily reflect those of the European Union or CINEA. Neither the European Union nor the granting authority can be held responsible for them. This project has received funding from Horizon Europe research and innovation programme under Grant Agreement No.1069890

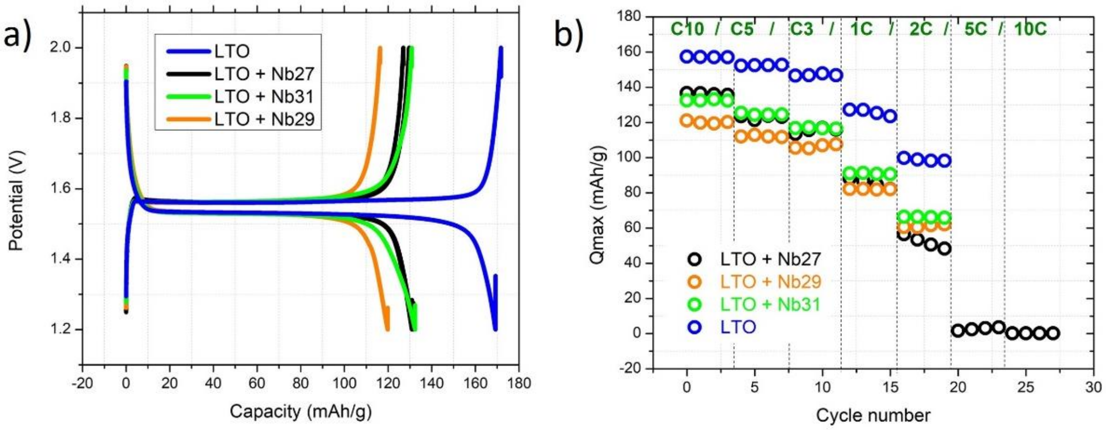

Figure 20. Coin cell testing results for baseline LTO and Nb ion implantation treatments.

<u>Carbon ion implantation processes</u>

Two different carbon ion implantation treatments were performed on LTO/Cu anodes according to the process parameters shown in Table 5.

Table 5. Process parameters of C ion implantation treatments.

Process	Ion implanted	Samples	Treatment time (min.)	Accelerating voltage (kV)	Ion dose (1/cm^2)
010-23	C	LTO/Cu	5	20	$7.93 \cdot 10^{15}$
011-23	C	LTO/Cu	30	25	$7.93 \cdot 10^{16}$

Figure 21 shows the images of LTO/Cu electrodes before and after the 010-23 and 011-23 carbon ion implantation processes. As can be seen with the naked eye, sample implanted with C ions in the 010-23 process shows just a little change in the appearance, whereas the one implanted in the 011-23 process (at higher ion dose and accelerating voltage) has been strongly darkened.

Funded by the European Union

Views and opinions expressed are those of the author(s) only and do not necessarily reflect those of the European Union or CINEA. Neither the European Union nor the granting authority can be held responsible for them. This project has received funding from Horizon Europe research and innovation programme under Grant Agreement No.1069890

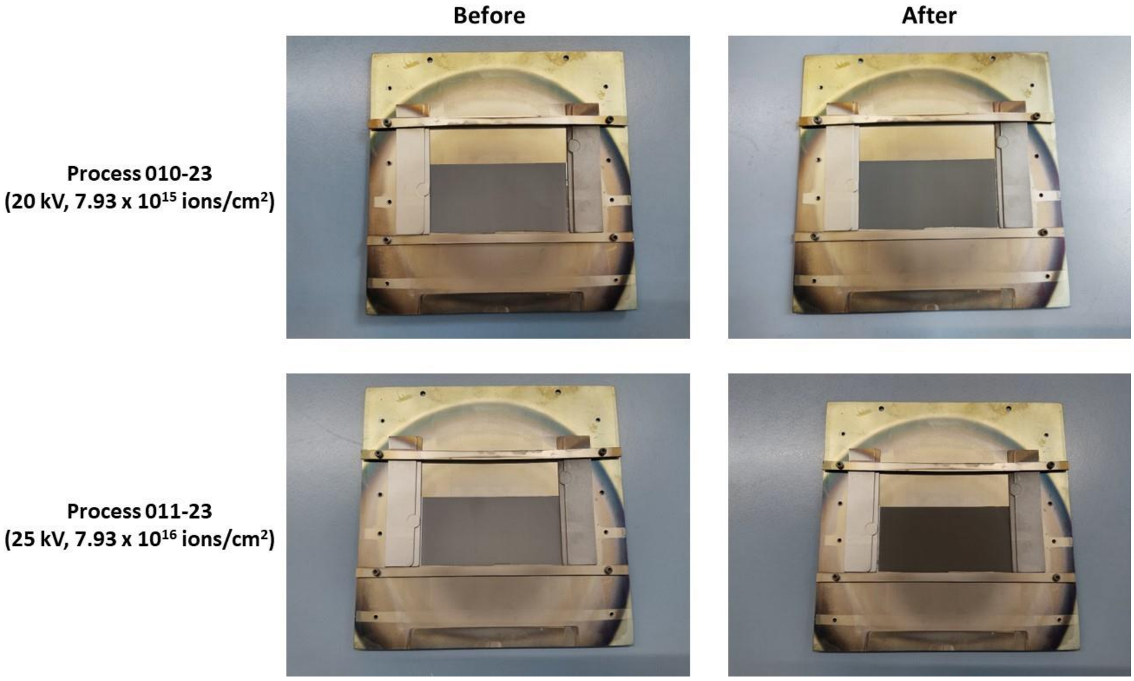

Figure 21. Images of LTO/Cu electrodes before and after the 010-23 and 011-23 carbon ion implantation process.

Treated samples with processes 010-23 and 011-23 were tested electrochemically in half-cell, and results are presented in Figure 22 Results for untreated LTO/Cu electrodes are included for comparison. All samples show similar discharge capacities at low and high C-rates and in the range of 185-190 mAhg^{-1} at 1C, Figure 22a). Some coin cells were tested for long cycling at C/2; the results are presented in Figure 22b). Performance shows cycling ageing with no clear differences among samples. The samples reach 80% SOH after 200 cycles. Therefore, C ion implantation does not improve the electrochemical performance of LTO at the electrode level.

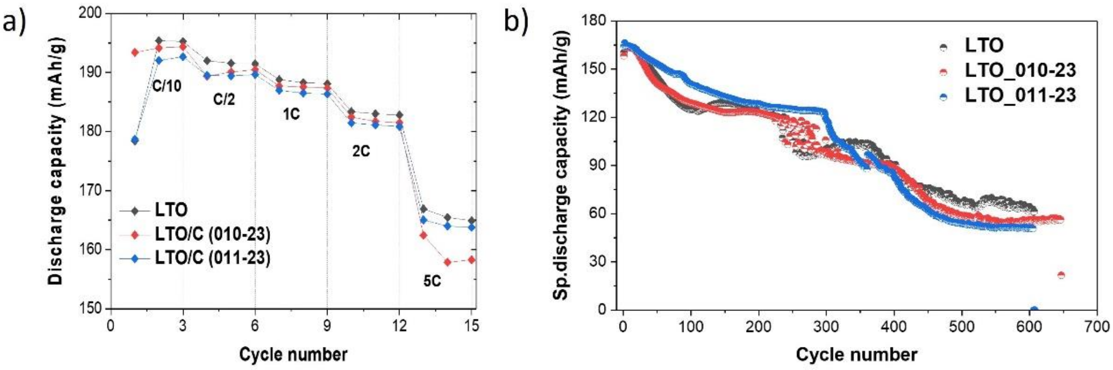

Figure 22. Coin cell testing results for LTO and C ion implantation treatments.

Funded by the European Union

Views and opinions expressed are those of the author(s) only and do not necessarily reflect those of the European Union or CINEA. Neither the European Union nor the granting authority can be held responsible for them. This project has received funding from Horizon Europe research and innovation programme under Grant Agreement No.1069890

Aluminium ion implantation processes

Aluminium ion implantation treatments were performed on graphite/Cu anodes and on NMC-622 ($LiNi_{0.6}Mn_{0.2}Co_{0.2}O_2$)/Al cathodes according to the process parameters shown in Table 6.

Table 6. Process parameters of Al ion implantation.

Process	Ion implanted	Samples	Treatment time (min.)	Accelerating voltage (kV)	Ion dose (1/cm^2)
006-24	Al	Graphite/Cu	5	15	$9.55 \cdot 10^{13}$
007-24	Al	NMC-622/Al	5	15	$9.55 \cdot 10^{13}$
008-24	Al	NMC-622/Al	30	15	$5.73 \cdot 10^{14}$

Figure 23 shows microscope images of graphite/Cu electrode before and after the 006-24 aluminium ion implantation process. Similarly, Figure 24 shows microscope images of NMC-622/Al electrodes before and after the 007-24 and 008-24 aluminium ion implantation processes. In both cases, no significant morphological differences were observed between untreated and treated samples.

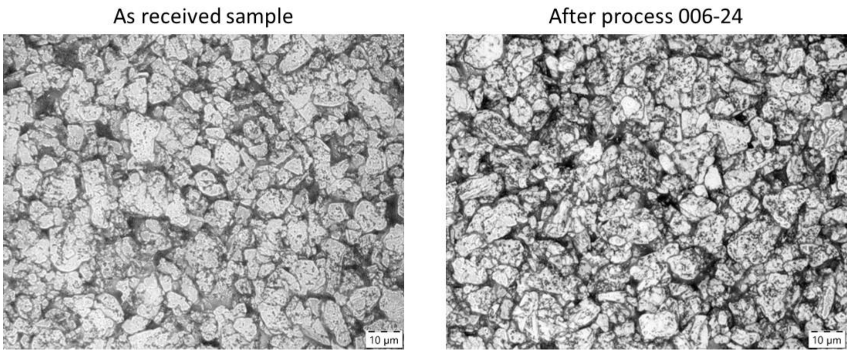

Figure 23. Microscope images of graphite/Cu electrode before and after the 006-24 aluminium ion implantation process.

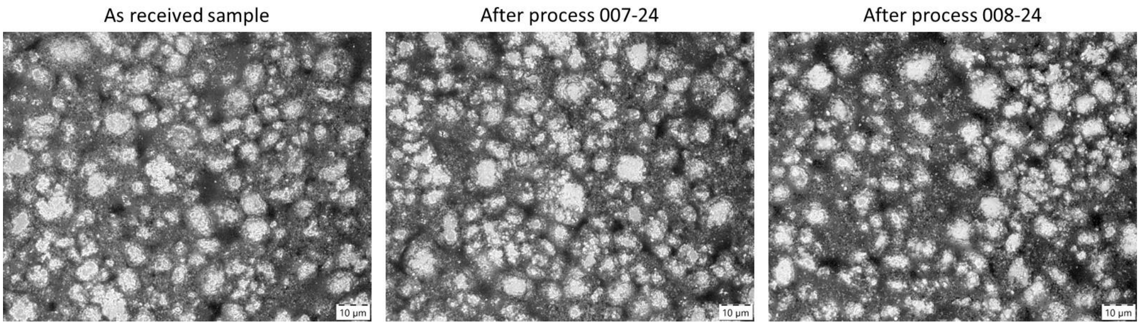

Figure 24. Microscope images of NMC-622/Al electrodes before and after the 007-24 and 008-24 aluminium ion implantation processes.

Funded by the European Union

Views and opinions expressed are those of the author(s) only and do not necessarily reflect those of the European Union or CINEA. Neither the European Union nor the granting authority can be held responsible for them. This project has received funding from Horizon Europe research and innovation programme under Grant Agreement No.1069890

Electrochemical testing of these samples is performed in half-cells. Commercial NMC622 is used as a reference material for Aluminum ion implemented samples 007-24 and 008-24 with 1M $LiPF_6$ in EC:DEC 1:1 electrolyte and 12.336mg/disc (12mm diameter). Cyclic voltammetry and impedance spectroscopy of Al-ion implemented samples are as shown in Figure 25. For each condition, 3 half-cells are measured. Al-ion implemented samples show a similar oxidation-reduction behavior while the resistance of Al-007-24 and Al-008-24 are low and similar to the resistance of commercial NMC622 electrodes.

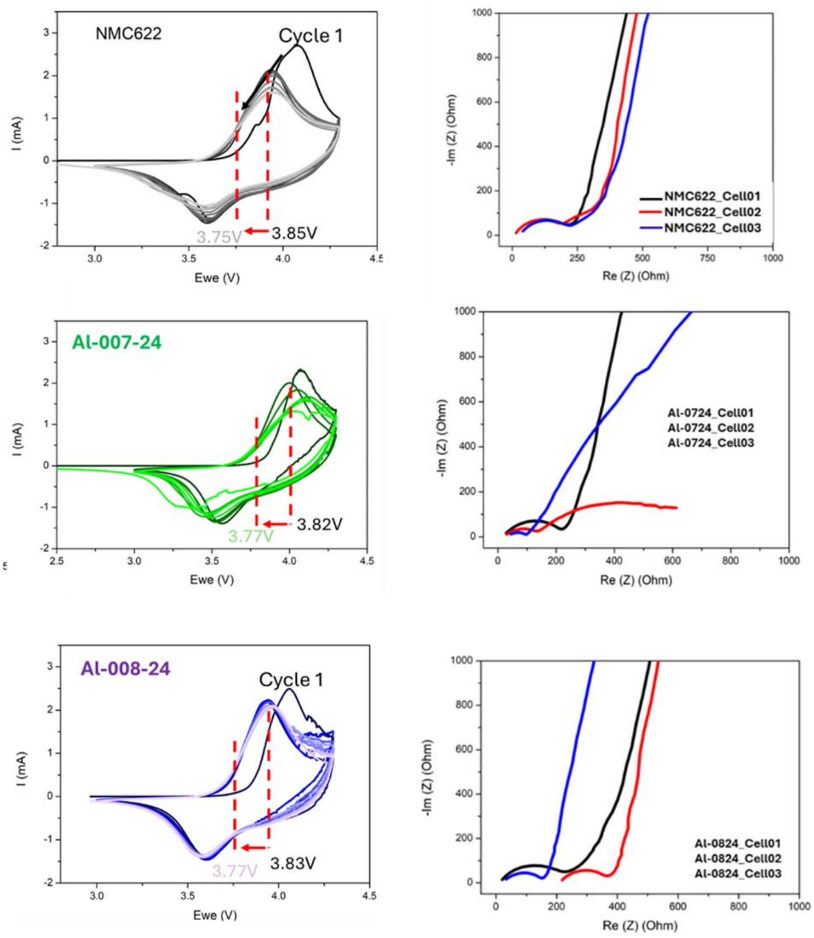

Figure 25. Cyclic voltammetry (CV) and resistance of half-cells by impedance spectroscopy for commercial NMC622, Al-007-24 and Al-008-24 respectively.

Surface of the electrodes is analyzed by Fourier-transform infrared spectroscopy (FTIR), and compared with untreated cathode to detect the Al-O bond (Figure 26). There is no significant difference in the absorbance of commercial NMC622 with Al-ion implemented 007-24 and 008-24.

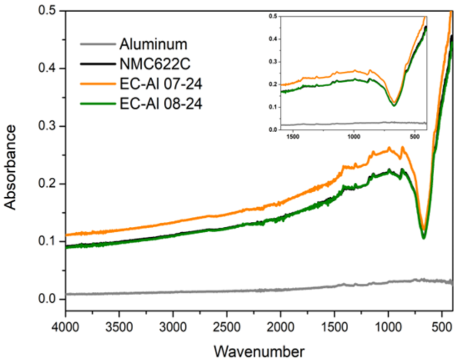

Figure 26. Fourier-transform infrared spectroscopy (FTIR) of Al-ion implemented 007-24, 008-24 with respect to commercial NMC622.

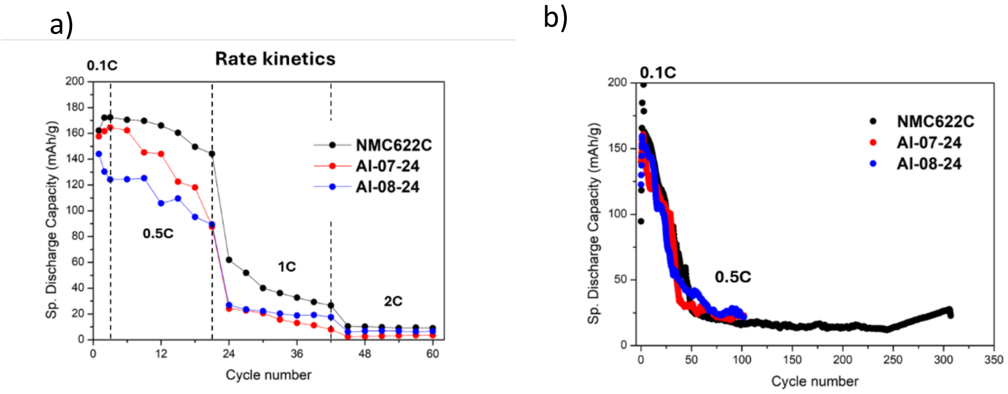

Figure 27. Coin cell testing results for Al ion implantation treatments on NMC622 in the range of 4.3-3.0V with stainless steel coin-cell caps.

Treated samples with processes 007-24 and 008-24 were tested electrochemically in half-cell using stainless-steel coin-cell caps, and results are presented in Figure 27. Results for untreated NMC622 electrodes are included for comparison. All samples show similar discharge capacities at low and high C-rates and in the range of 160-170 mAh g^{-1} at 0.1C for NMC622 and 007-24, 130-140 mAh g^{-1} at 0.1C for 008-24 Figure 27a. Some coin cells were tested for long cycling at C/2; the results are presented in Figure 27b. It is observed that there is almost no influence of Al ion implementation on the NMC622 electrodes. Furthermore, above 4V stainless steel has shown a reaction-limiting behaviour with NMC622 cathode leading to unstable electrochemical results. Therefore, similar electrochemical tests were performed with aluminium-coated coin-cell caps.

When the coin-cells were assembled with aluminium-coated caps, the stability of the electrochemical measurements have improved significantly. However, as shown in Figure 28a the discharge specific capacities are similar for Al-ion implemented samples compared to NMC622. In addition to that, long cycling at C/10 is performed for two coin-cells in each condition and 180-200 mAh g^{-1} at C/10 is the discharge capacity for NMC622, 007-24 and 008-24 (Figure 28b). The Al-ion implantation with studied conditions is negligible on the electrochemical performance of NMC622 cathodes. Because of the enhanced electrochemical stability of the measurements, from now on all coin-cells are prepared with aluminium coated coin-cells.

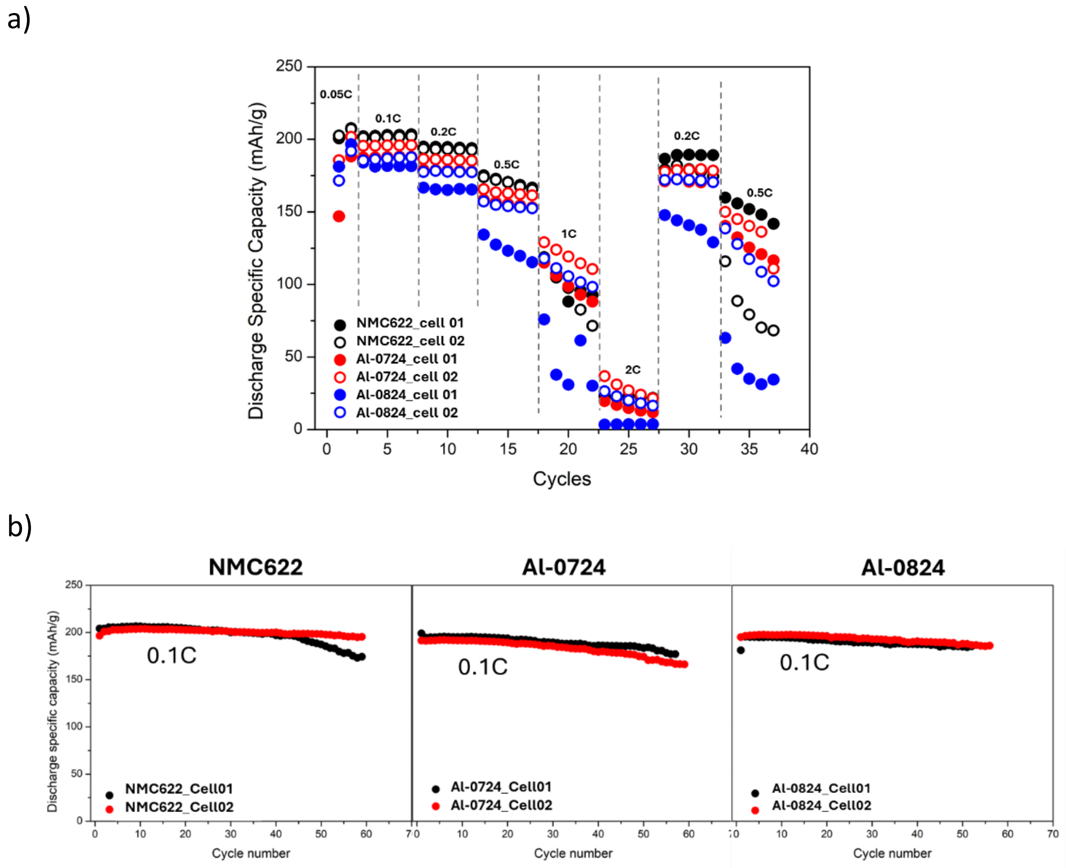

Figure 28. Coin cell testing results for Al ion implantation treatments on NMC622 in the range of 4.3-3.0V with aluminum coated coin-cell caps.

Electrochemical tests of Al-ion implantation on graphite electrode were performed with two different electrolytes, EC:DEC 1:1 and E7 (1.2M $LiPF_6$ in EC/DMC/EMC (2:3:5 vol%) + 2wt% VC + 10wt% FEC) with additives to work in lower potentials such as 1.0-0.01V.

In the presence of electrolyte EC:DEC 1:1 the discharge capacity of Al-ion implanted sample decreases sharply during long cycling at 0.1C while the reference graphite anode performs better with 250 mAh g^{-1} at 0.1C (Figure 29d). However, in the presence of the electrolyte E7 with additives, the stability has significantly improved (Figure 29a). The Al-ion implantation has either a negligible effect (in the case of E7 electrolyte) or a negative impact (in the case of electrolyte EC:DEC 1:1) which might be due to the blocking of the Li^+ diffusivity at the electrode level limiting discharge capacity.

Views and opinions expressed are those of the author(s) only and do not necessarily reflect those of the European Union or CINEA. Neither the European Union nor the granting authority can be held responsible for them. This project has received funding from Horizon Europe research and innovation programme under Grant Agreement No.1069890

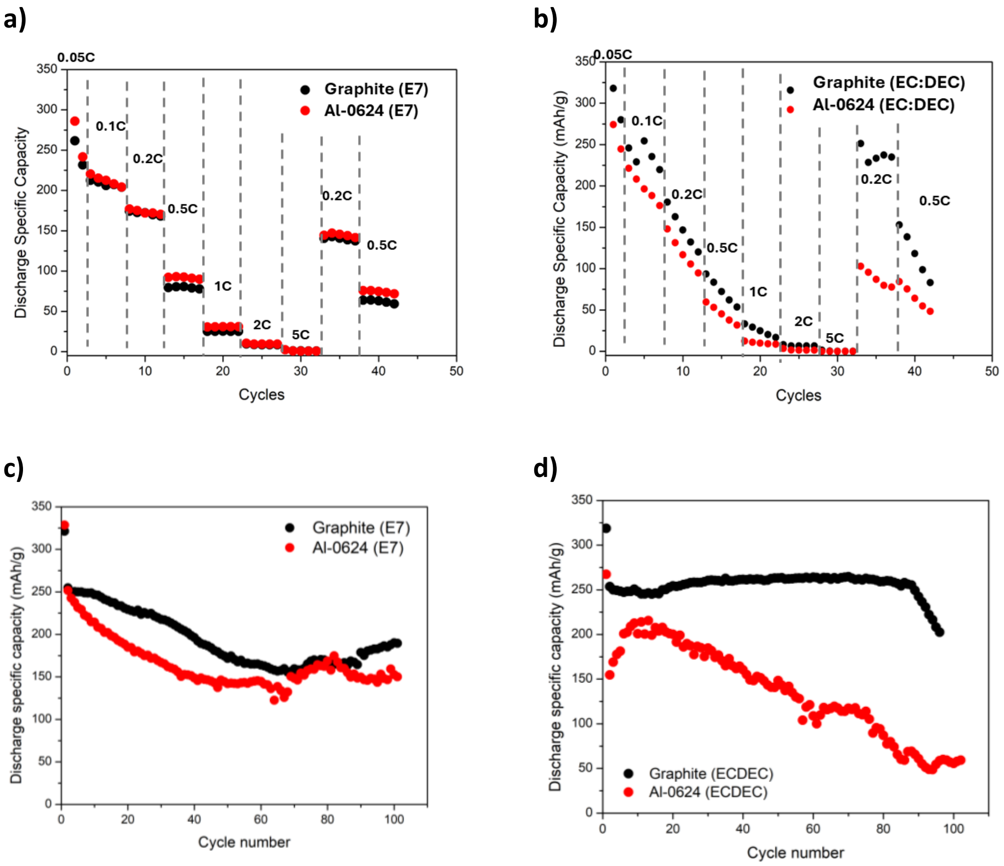

Figure 29. Coin cell testing results for Al ion implantation treatments on graphite/ copper anodes in the range of 1.0-0.01V with EC:DEC 1:1 and E7 electrolytes.

Al-deposition by atomic-layer deposition (ALD)

Atomic layer deposition is a powerful technique for surface and interface engineering in the applications of energy storage and conversion due to the controlled material deposition with atomic-level precision. During an ALD process gas-phase precursors are sequentially exposed to the substrate, forming self-limiting and saturated surface reactions. Uniform growth by precise thickness control is achieved by ALD as surface coating layers on cathode and anode materials to overcome structural and interfacial problems.

Funded by the European Union

Views and opinions expressed are those of the author(s) only and do not necessarily reflect those of the European Union or CINEA. Neither the European Union nor the granting authority can be held responsible for them. This project has received funding from Horizon Europe research and innovation programme under Grant Agreement No.1069890

Figure 30. ALD/MLD equipment of IREC.

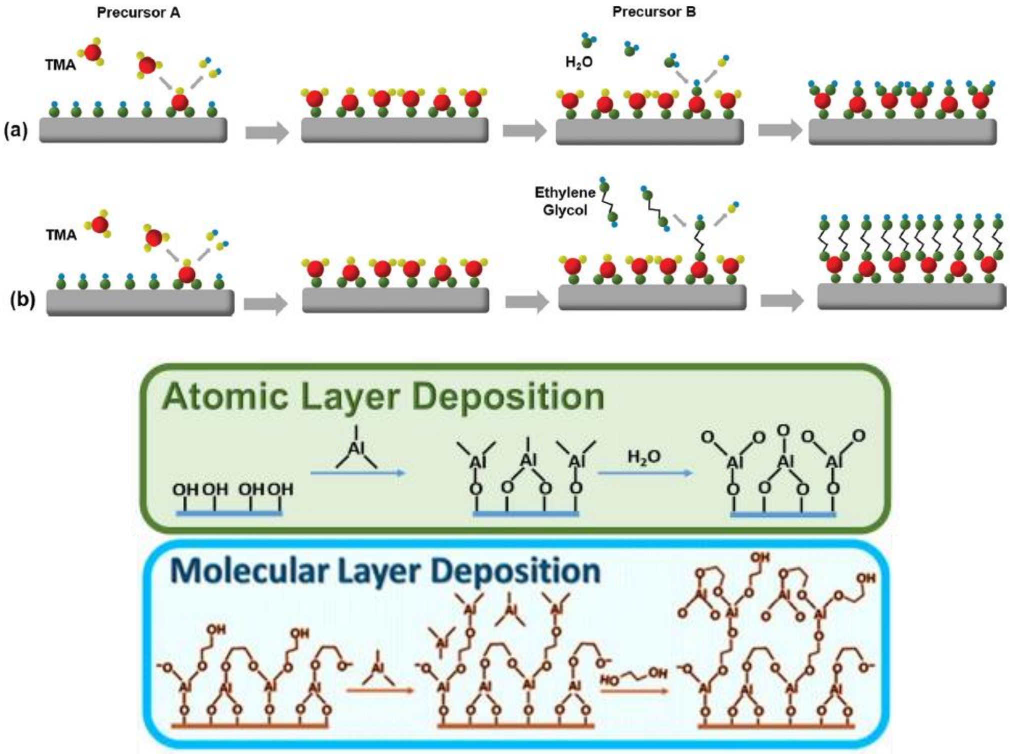

Figure 31. ALD and MLD growth mechanism.

Funded by the European Union

Views and opinions expressed are those of the author(s) only and do not necessarily reflect those of the European Union or CINEA. Neither the European Union nor the granting authority can be held responsible for them. This project has received funding from Horizon Europe research and innovation programme under Grant Agreement No.1069890

Atomic layer deposition is performed on NMC622 ($LiNi_{0.6}Mn_{0.2}Co_{0.2}O_2$)/Al and graphite/ copper electrodes with different temperature and deposition cycles. Studied conditions are listed in Table 7.

Table 7. Process parameters of Al deposition by ALD.

Samples	Substrate	Number of deposited cycles	Deposition Temperature (°C)
AL100-130C	NMC622/Al	100	130
AL100-170C	NMC622/Al	100	170
AL300-130C	NMC622/Al	300	130
AL300-150C	NMC622/Al	300	150
AL300-170C	NMC622/Al	300	170
AL100-130C	Graphite/Cu	100	130
AL100-150C	Graphite/Cu	100	150
AL300-130C	Graphite/Cu	300	130
AL300-150C	Graphite/Cu	300	150
AL300-170C	Graphite/Cu	300	170

Figure 32 show the surface functional groups before and after the Al_2O_3 deposition by atomic layer deposition (ALD) on NMC622 cathode. Towards lower wavenumber, Al-O interaction is visible especially for 300 cycles of Al_2O_3 deposition defined as Al300.

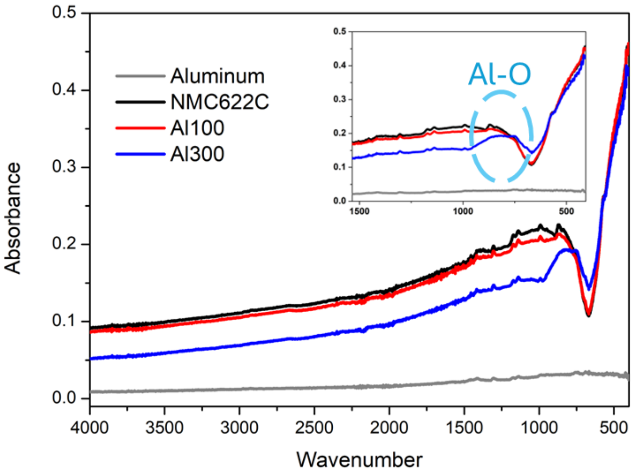

Figure 32. FTIR result of Al_2O_3 deposition by ALD on NMC622 cathode.

Funded by the European Union

Views and opinions expressed are those of the author(s) only and do not necessarily reflect those of the European Union or CINEA. Neither the European Union nor the granting authority can be held responsible for them. This project has received funding from Horizon Europe research and innovation programme under Grant Agreement No.1069890

The resistance of deposited thin films is measured and compared with untreated NMC622 cathode and graphite anode respectively (Figure 33a on NMC622, Figure 33b on graphite). The EIS of NMC622 samples are similar when compared to untreated cathode; however, 300 cycles on graphite anode at 130C exhibit greater resistance, which might be attributed to the resistance of Al_2O_3 thin film on the anode.

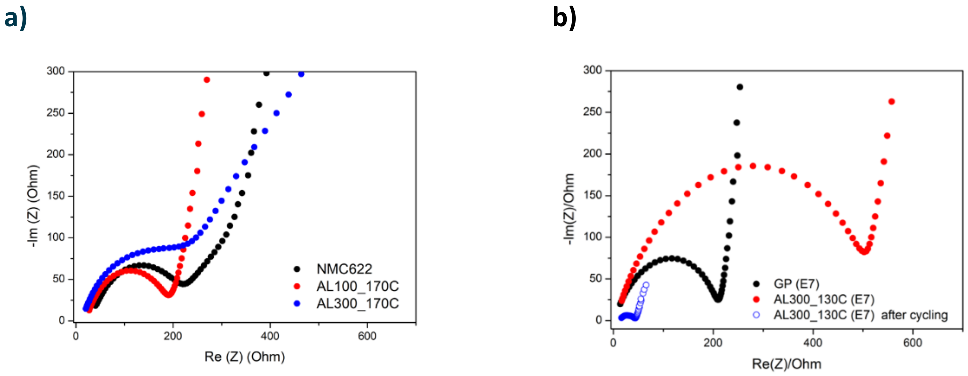

Figure 33. Resistance of untreated and Al_2O_3 deposited on a) NMC622 and b) graphite respectively.

Rate kinetics of Al_2O_3 deposited electrodes are studied for both NMC622 cathode and graphite anode (Figure 34). Among all Al-deposited conditions, there is no significant difference with respect to the bare cathode and anode. However, for NMC622 cathode, AL100_170C is the condition with discharge capacity similar to untreated NMC622 with 195-198 mAh g^{-1} at C/10. As the number of cycles has increased to 300 cycles, discharge capacity tends to decrease, which might be due to the limited Li^+ diffusivity. In order to prove that thinner Al_2O_3 deposition might improve the electrochemical performance, further tests need to be performed.

On the graphite anode (Figure 34b), untreated graphite exhibit discharge capacity 210-220 mAh g^{-1} at C/10, while AL300-150C and AL300-170C show a similar discharge property around 200 mAh g^{-1} at C/10. The deposition has a negligible influence on the electrochemical performance of graphite anode.

Views and opinions expressed are those of the author(s) only and do not necessarily reflect those of the European Union or CINEA. Neither the European Union nor the granting authority can be held responsible for them. This project has received funding from Horizon Europe research and innovation programme under Grant Agreement No.1069890

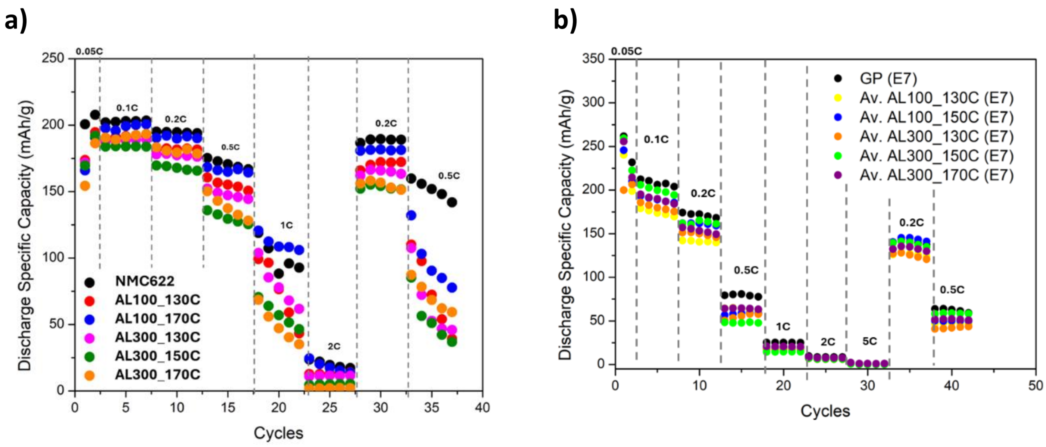

Figure 34. C-rate kinetics comparison of a) NMC622 and b) graphite electrodes.

Overall comparison of all Al-deposited (by ion implantation and ALD) are presented in Figure 35 for both NMC622 and graphite electrodes. Although the influence of Al on electrodes are negligible, Al-007-24 with $9.55 \cdot 10^{13}$ ion dose/cm^2 and 100 cycles of Al_2O_3 at 170ºC are the most promising conditions. Lower doses of aluminium and thinner layers of Al_2O_3 need to be studied to prove the improvement on NMC622 electrodes. For the anode material, Al-ion implanted with $9.55 \cdot 10^{13}$ ion dose/cm^2 shows 91 mAh g^{-1} at 0.5C while untreated graphite has a discharge capacity of 79 mAh g^{-1} at C/2. Lower doses of Al need to be ion-implanted on graphite to investigate further the impact in terms of the electrochemical performance.

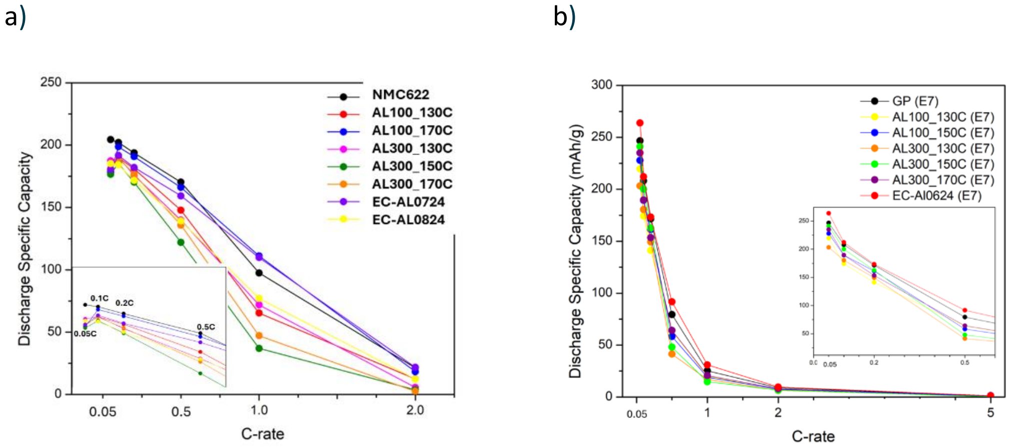

Figure 35. Overall comparison of all Al-deposited conditions by ion-implantation and atomic layer deposition on a) NMC622 and b) graphite.

Views and opinions expressed are those of the author(s) only and do not necessarily reflect those of the European Union or CINEA. Neither the European Union nor the granting authority can be held responsible for them. This project has received funding from Horizon Europe research and innovation programme under Grant Agreement No.1069890

5. Electrochemical and morphological analyses of recovered NMC 811 cathode material synthesized by hydrothermal process

5.1 Results

5.1.1 Morphological and Structural Characterization of NMC811 Cathode Powders Synthesized from Recycled Materials

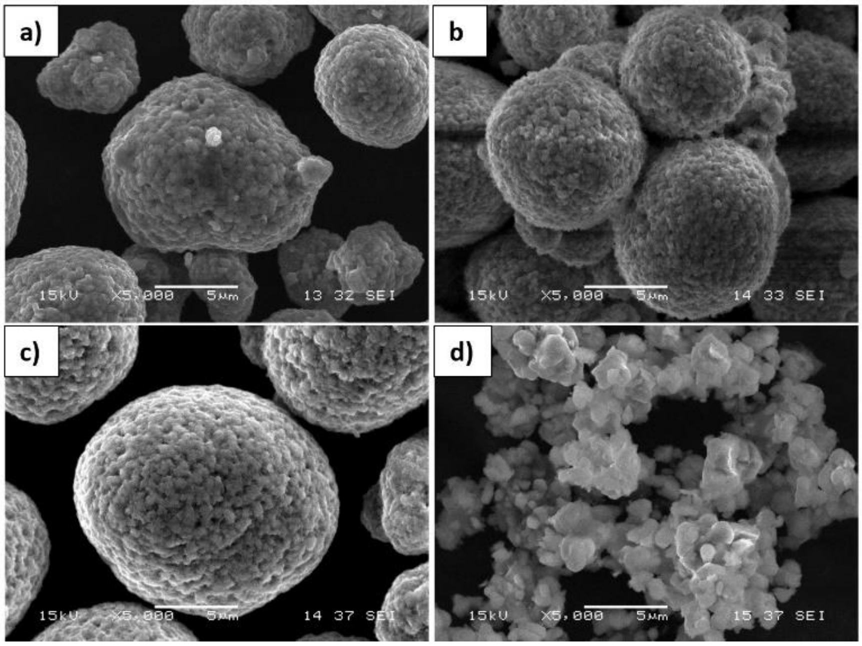

Figure 36. The SEM images of a) commercial NMC811, b) CPO7, c) CPO9 and d) CPO23 powders.

For comparative analysis, commercial NMC811, CPO7, CPO9, and CPO23 (produced by Torrecid) were investigated using a scanning electron microscope (SEM, JEOL 6060LV). Elemental composition was assessed through energy dispersive spectroscopy (EDS) equipped onto SEM. The morphology of the commercial NMC622 powder is illustrated in Figure 36a. The aggregates of commercial NMC811 particles display dense packing and consist of relatively small primary particles. These aggregates exhibit a uniform size distribution, with particle dimensions ranging from 5 to 10 µm. SEM images clearly reveal that CPO7 and CPO9 exhibit a similar morphological structure and particle size distribution as observed in the commercial NMC811. However, as illustrated in Figure 36d, CPO23 exhibits a finer-grained, submicron structure, in contrast to the compact and dense particle morphology observed in the other samples including the commercial NMC811.

Funded by the European Union

Views and opinions expressed are those of the author(s) only and do not necessarily reflect those of the European Union or CINEA. Neither the European Union nor the granting authority can be held responsible for them. This project has received funding from Horizon Europe research and innovation programme under Grant Agreement No.1069890

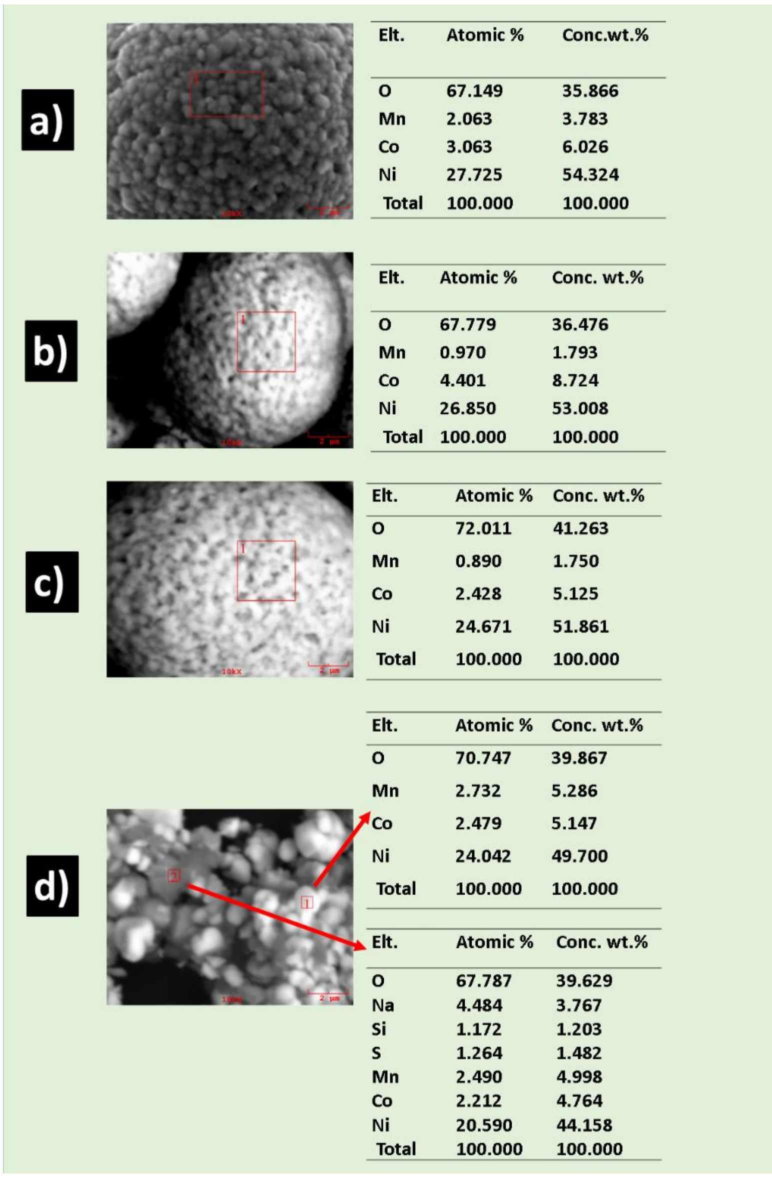

Elt.	Atomic %	Conc.wt.%
O	67.149	35.866
Mn	2.063	3.783
Co	3.063	6.026
Ni	27.725	54.324
Total	100.000	100.000

Elt.	Atomic %	Conc. wt.%
O	67.779	36.476
Mn	0.970	1.793
Co	4.401	8.724
Ni	26.850	53.008
Total	100.000	100.000

Elt.	Atomic %	Conc. wt.%
O	72.011	41.263
Mn	0.890	1.750
Co	2.428	5.125
Ni	24.671	51.861
Total	100.000	100.000

Elt.	Atomic %	Conc. wt.%
O	70.747	39.867
Mn	2.732	5.286
Co	2.479	5.147
Ni	24.042	49.700
Total	100.000	100.000

Elt.	Atomic %	Conc. wt.%
O	67.787	39.629
Na	4.484	3.767
Si	1.172	1.203
S	1.264	1.482
Mn	2.490	4.998
Co	2.212	4.764
Ni	20.590	44.158
Total	100.000	100.000

Figure 37. Atomic and weight percentages of the elements obtained from EDS analyses for a) commercial NMC811, b) CPO7, c) CPO9 and d) CPO23 powders.

The Energy Dispersive Spectroscopy (EDS) analysis of commercial NMC811, CPO7, and CPO9, as shown in Figure 37, indicates the presence of Ni, Co, Mn, and O elements, with no detectable impurities. In contrast, CPO23 displays contaminant elements, including S, Si, and Na. These impurities are likely residues from salts used during the production process, such as sulphates.

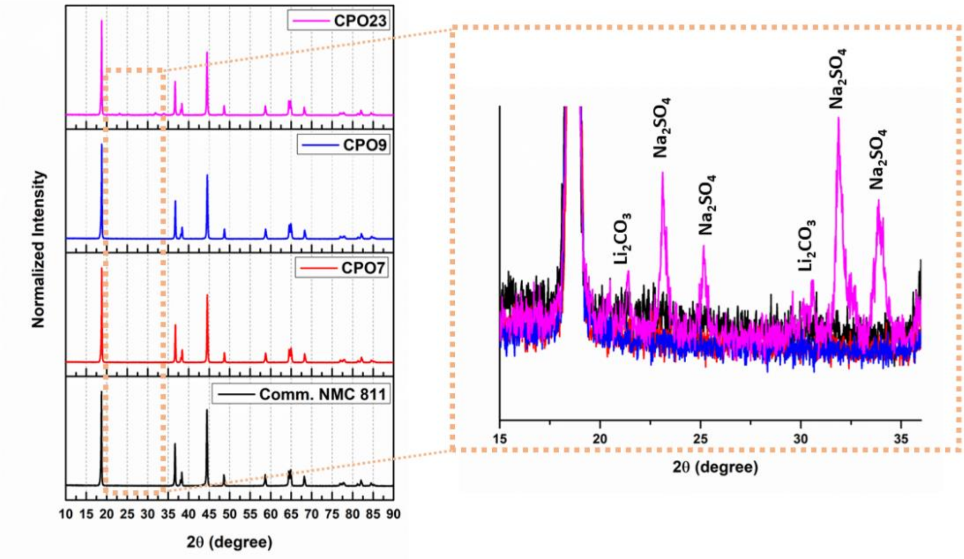

Figure 38. XRD spectrum of commercial NMC811, CPO7, CPO9 and CPO23 powders.

Phase analysis of commercial NMC811, CPO7, CPO9 and CPO23 was conducted using X-ray diffraction technique utilizing Rigaku D/MAX 2000 X-ray diffractometer equipped with Cu Kα radiation (wavelength: 1.54 Å) at a scanning rate of 2°/min within the 2θ range of 10–90°. Figure 38 displays the XRD spectra for commercial NMC811, CPO7, CPO9 and CPO23 samples. The X-ray diffraction (XRD) spectrum of the commercial NMC811 powders demonstrates a pattern that is consistent with the data reported in the literature [1]. XRD patterns of CP07 and CP09 samples are matched well with the reference pattern of commercial sample, whereas for CP023 small peaks that can be indexed to Li_2CO_3 and Na_2SO_4 are observed at between around 2θ of 15° and 35°. Coupled with the EDS analyses, sulphur and sodium impurities are evident in the CP023 sample.

5.2 Electrochemical Characterization of NMC811 Cathode Powders Synthesized from Recycled Materials

The parameters for electrode preparation (including the amounts of PVDF, carbon black, and active material), coin cell assembly conditions (such as the type of coin cell, electrolyte volume, and separator type), as well as the electrochemical test conditions, are detailed in Table 8.

---

[1] Akhilash, M., Salini, P. S., John, B., Supriya, N., Sujatha, S., & Mercy, T. D. (2023). Thermal stability as well as electrochemical performance of Li-rich and Ni-rich cathode materials—a comparative study. Ionics, 29(3), 983-992.

Views and opinions expressed are those of the author(s) only and do not necessarily reflect those of the European Union or CINEA. Neither the European Union nor the granting authority can be held responsible for them. This project has received funding from Horizon Europe research and innovation programme under Grant Agreement No.1069890

Table 8. Electrode preparation, coin cell assembly and electrochemical test conditions for commercial NMC 811, CPO9 and CPO23 samples.

NMC811, CPO9 and CPO23 electrode test specifications		
Electrode preparation	Binder type and amount	PVDF – 10 wt%
	Carbon black amount	Super P – 10 wt%
	Active material amount	80 wt.%
	Electrode thickness	Wet thickness ~300 µm
	Mass Loading (mg/cm^2)	~5 mg/cm^2
Coin cell assembly	Coin cell type	2016
	Electrolyte type	60 µl of 1M $LiPF_6$ in EC:DMC
	Half-cell or full-cell	Half-cell
	Separator	Celgard 2400
Electrochemical tests	Charge/discharge test parameters	Voltage range: 4.2-2.7 V vs. Li/Li$^+$ Current: C/20
	Cyclic Voltammetry	Voltage range: 4.2-2.7 V vs. Li/Li$^+$ Scan rate: 0.1 mV/second
	Electrochemical Impedance Spectroscopy	Frequency range: 0.01 Hz- 100 kHz

Views and opinions expressed are those of the author(s) only and do not necessarily reflect those of the European Union or CINEA. Neither the European Union nor the granting authority can be held responsible for them. This project has received funding from Horizon Europe research and innovation programme under Grant Agreement No.1069890

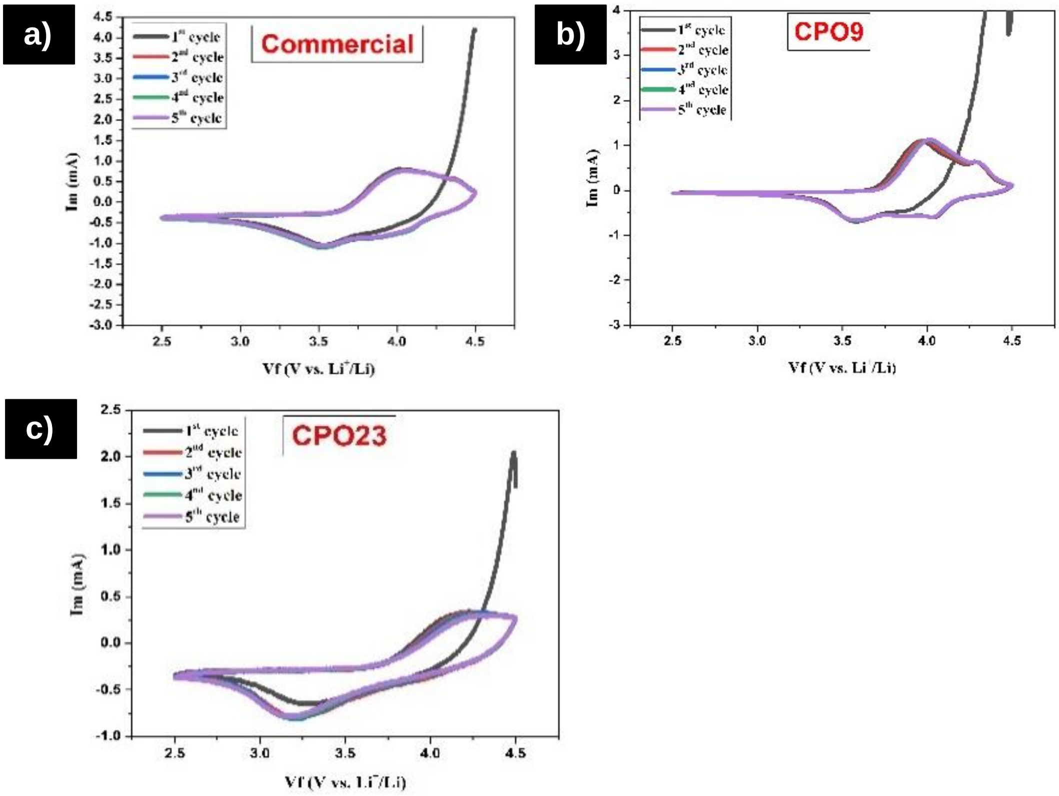

Figure 39. Cyclic voltammograms of a) commercial NMC811, b) CPO9 and c) CPO23 samples.

Figure 39 presents the cyclic voltammograms (CVs) of commercial NMC811, CPO9 and CPO23 samples. In the anodic scan of NCM811, a prominent oxidation peak is observed at approximately 3.95 V, corresponding to the lithium insertion process. Conversely, in the cathodic curve of NCM811, two discernible reduction peaks are detected: a minor peak and a more pronounced peak, situated at approximately 3.95 V and 3.58 V, respectively. The minor reduction peak stands for the multiphase transitions between two hexagonal structures, while the sharp reduction peak is attributed to a redox reaction.

Electrochemical Impedance Spectroscopy (EIS) measurements were conducted within the frequency range of 0.01 Hz to 100 kHz, employing a excitation voltage of 10 mV. The semicircles observed at medium frequencies correspond to the charge-transfer resistance (Rct), reflecting the kinetic reaction occurring at the interface between the electrolyte and the electrode. In the Nyquist plots of commercial NMC811, it is evident that the charge transfer resistance increases after 5 CV cycles, a phenomenon attributed to the formation of the cathode electrolyte interphase (CEI) layer. While the CPO9 sample exhibits almost identical impedance behaviour to commercial NMC811, CPO23 displays higher resistivity after 5-cycle CV tests. The elevated charge transfer resistance observed in CPO23 can be ascribed to its smaller particle size relative to commercial NMC811 and CPO9. The reduced particle size leads to an increased surface area for CPO23. Consequently, the content of the surface electrolyte interphase (SEI) layer is increased with the larger surface area, resulting in a higher resistance for the CPO23 samples.

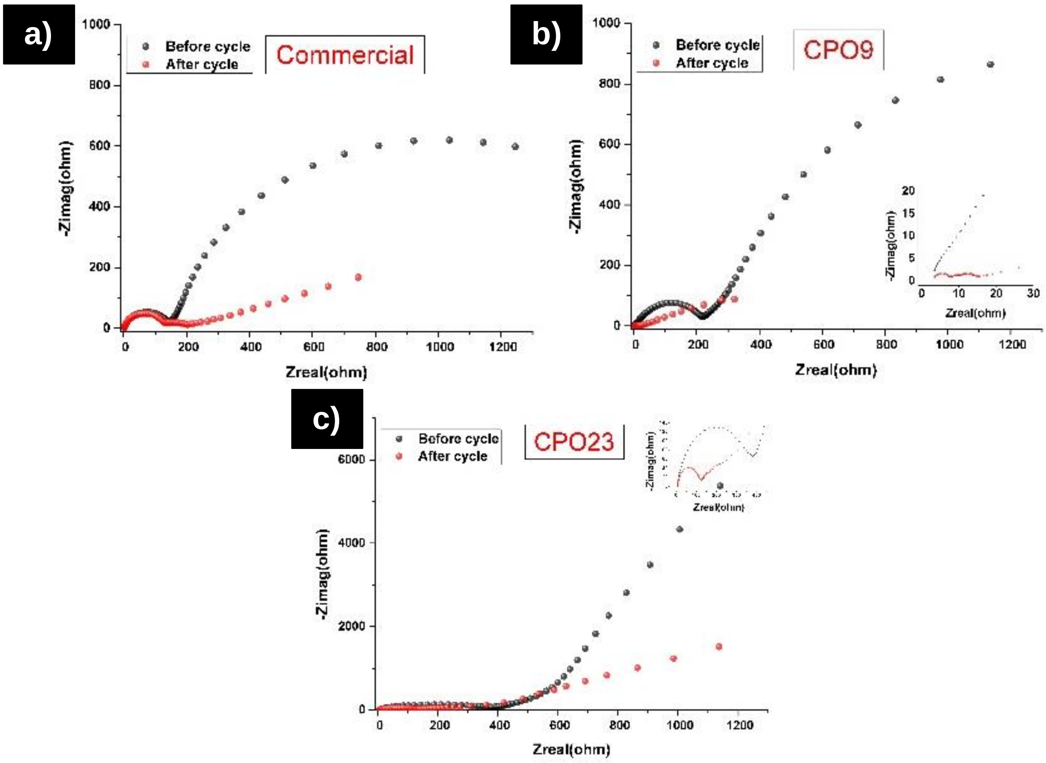

Figure 40. Nyquist plots of a) commercial NMC811, b) CPO9 and c) CPO23 samples before and after five cycle CV tests.

Figure 41 presents the electrochemical galvanostatic charge/discharge curves at C/20 (first 4 cycles) and C/10 C-rates for commercial NMC811, CPO9, and CPO23 samples. After the first charge-discharge at C/20 current density, commercial NMC811 displayed a specific capacity exceeding 235 mAh g^{-1}, while the CPO9 and CPO23 samples demonstrated specific capacities of 205 mAh g^{-1} and 143 mAh g^{-1}, respectively. Following 25 cycles (4 cycles at C/20 + 21 cycles at C/10 C-rate), commercial NMC811 showed a specific capacity of 114 mAh g^{-1}, whereas CPO9 and CPO23 displayed specific capacities of 191 mAh g^{-1} and 126 mAh g^{-1}, respectively. These results indicate the feasibility of these samples for pouch cell assembly.

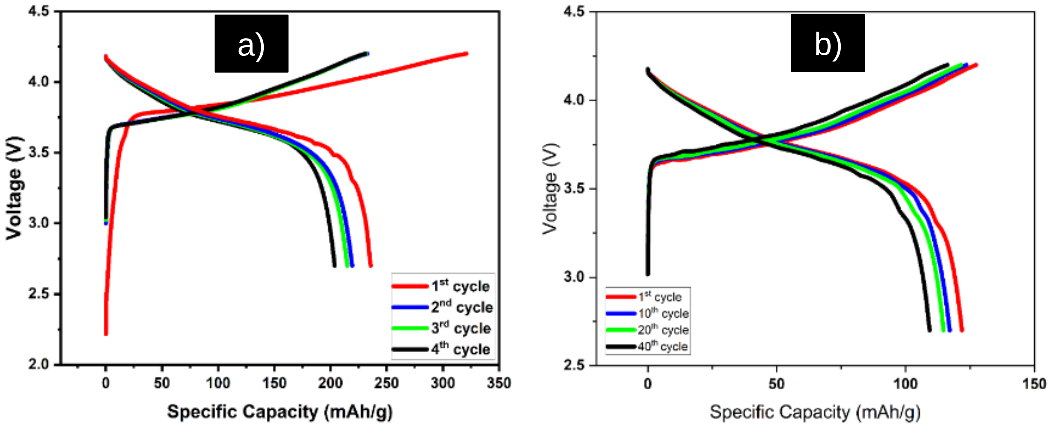

Funded by the European Union

Views and opinions expressed are those of the author(s) only and do not necessarily reflect those of the European Union or CINEA. Neither the European Union nor the granting authority can be held responsible for them. This project has received funding from Horizon Europe research and innovation programme under Grant Agreement No.1069890

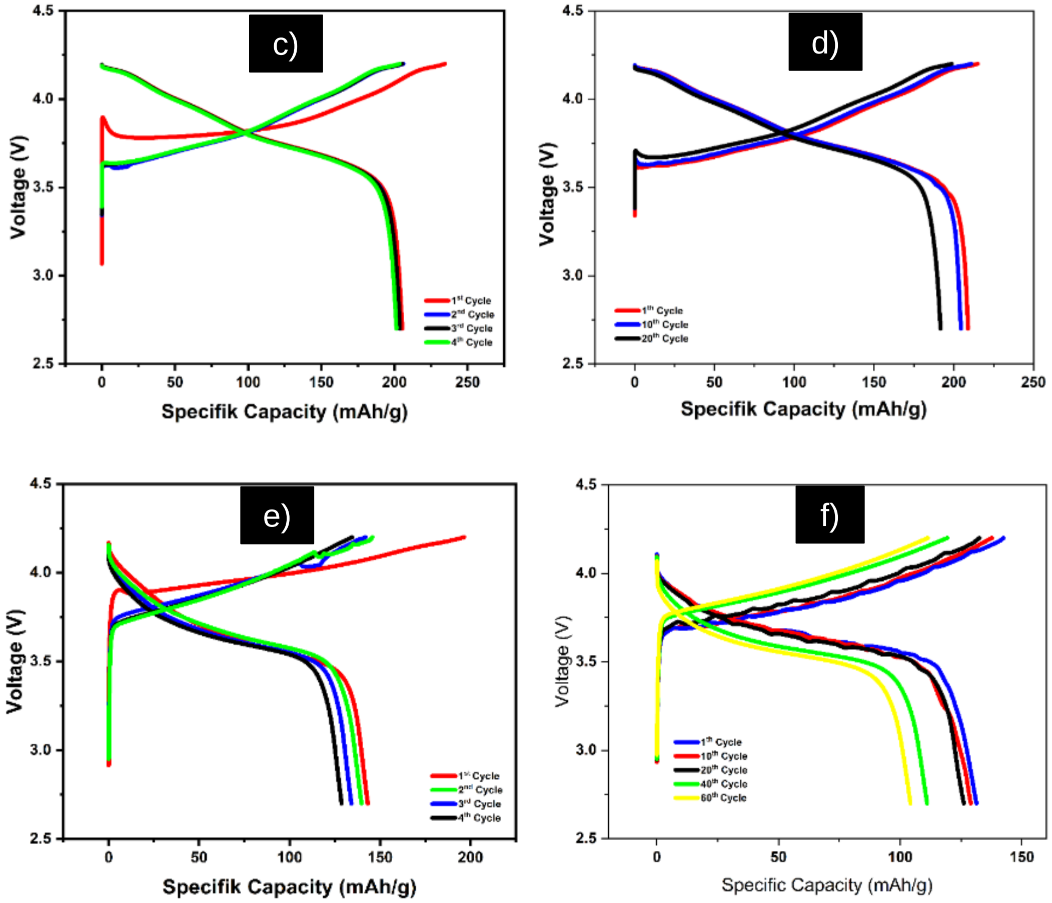

Figure 41. Electrochemical galvanostatic charge/discharge curves of a) commercial NMC811 initial four cycles at C/20 C-rate, b) commercial NMC811 at C/10 C-rate after four cycles at C/10 C-rate, c) CPO9 first four cycles at c/20 C-rate, d) CPO9 at C/10 C-rate after four cycles at C/10 C-rate, e) CPO23 first four cycles at c/20 C-rate and f) CPO23 at C/10 C-rate after four cycles at C/10 C-rate.

5.3 The electrochemical properties of high energy ball milled NMC811

5.3.1 Materials and Methods

High-energy ball milling was performed using Retsch 400 equipment. Electrodes for electrochemical testing were prepared from slurries composed of LMNO, carbon black (Super P), and polyvinylidene fluoride (PVDF) in a weight ratio of 90:5:5, with N-Methylpyrrolidone (NMP) as the solvent. These slurries were coated to aluminium foil via doctor blade with the wet thickness of 150 µm. The coated foil was then dried in two stages: initially at 70°C for 4 hours, followed by overnight drying in a vacuum oven at 110°C. Following the drying process, 12 mm diameter discs of the electrode material were cut and used to assemble C2032 coin cells. Each cell contained 36 µL of 1M LiPF6 electrolyte in a 1:1 (v/v) mixture of ethylene carbonate (EC) and diethyl carbonate (DEC), a single layer of Celgard 2400 separator, and lithium chips as the counter electrode. Electrochemical

Views and opinions expressed are those of the author(s) only and do not necessarily reflect those of the European Union or CINEA. Neither the European Union nor the granting authority can be held responsible for them. This project has received funding from Horizon Europe research and innovation programme under Grant Agreement No.1069890

measurements were conducted using a Biologic battery tester within a voltage range of 3.5 to 4.9 V. For galvanostatic charge/discharge experiments, the assumed capacity was 147 mAh g^{-1} at a 1C rate, and the C-rate measurements were adjusted accordingly. The galvanostatic results presented in this report represent the average of 10 replicates per sample.

5.3.2 Results

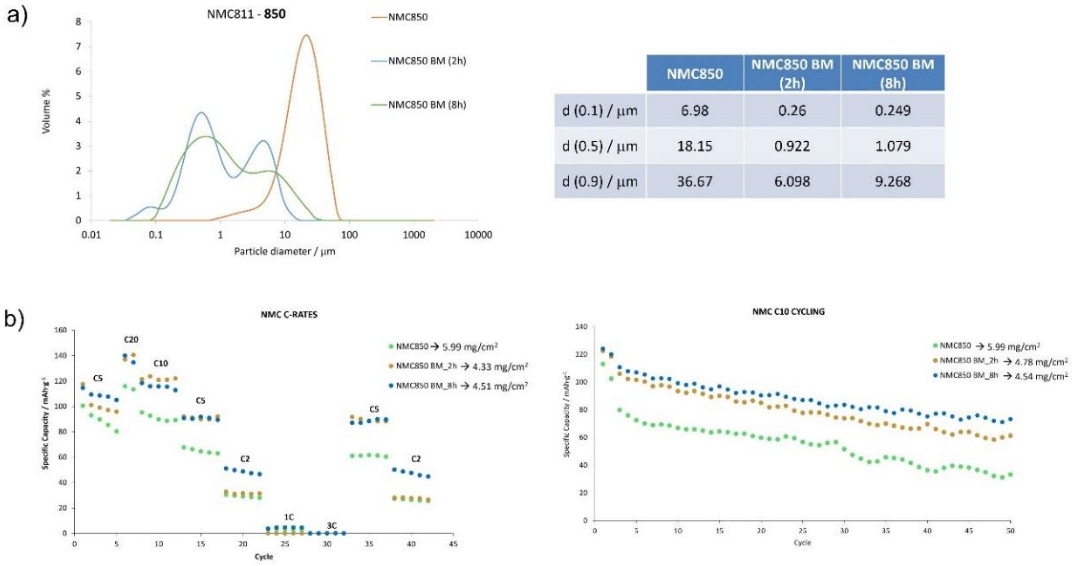

	NMC850	NMC850 BM (2h)	NMC850 BM (8h)
d (0.1) / μm	6.98	0.26	0.249
d (0.5) / μm	18.15	0.922	1.079
d (0.9) / μm	36.67	6.098	9.268

Figure 42. a) Particle size distribution measurements for NMC811 and ball milled samples for 2 and 8h and b) half-cell test results at coin-cell level.

The Particle Size Distribution (PSD) analysis of NMC811 (NMC850) reveals a bimodal distribution, consisting of primary and secondary particle sizes, similar to that observed in processed (ball-milled) samples. In such measurements, the commonly reported percentiles are d (0.1), d(0.5), and d(0.9). These percentiles facilitate the assessment of any significant variations in the median particle size d(0.5), as well as changes at the distribution's extremes, which may be indicative of the presence of fine particles or oversized particles and agglomerates. Milling NMC811 for 2 hours (NMC850 BM_2h) and 8 hours (NMC850 BM_8h) leads to notable changes in particle size, with d(0.1) decreasing from approximately 7 μm to less than 1 μm, the mean particle size reducing from around 18 μm to approximately 1 μm, and d(0.9) decreasing from about 36 μm to roughly 8 μm (see Figure 42a). This indicates a reduction in both the primary and secondary particle sizes. The samples were subjected to electrochemical testing, as illustrated in Figure 42b. The fabricated electrodes, particularly those from processed samples, exhibited an enhanced discharge capacity of 120 mAh g^{-1} at a C/10 rate compared to the baseline sample, which had a capacity of 90 mAh g^{-1}. Similar improvements were observed at higher C-rates. The ball-milled samples benefit from shorter diffusion pathways, which enhance charge/discharge kinetics. Long-term cycling tests demonstrated that, despite a similar degradation mechanism across all samples—characterized by capacity decay with cycling—the milled samples showed improved

Views and opinions expressed are those of the author(s) only and do not necessarily reflect those of the European Union or CINEA. Neither the European Union nor the granting authority can be held responsible for them. This project has received funding from Horizon Europe research and innovation programme under Grant Agreement No.1069890

discharge capacities. Overall, high-energy ball milling proves to be an effective method for enhancing the performance of (recycled) active materials.

6. Electrochemical and morphological investigation of recovered NMC 622 cathode material synthesized by solid state process

6.1 Materials and methods

Table 9 provides the sample codes alongside an explanation of the synthesis methods and the respective partners where the samples were obtained. Initially, the morphological and chemical characteristics of the samples are investigated. For comparative analysis, both commercial NMC622 and the synthesized samples (from various recycling methods in the FREE4LIB project) are examined using a scanning electron microscope (SEM, JEOL 6060LV), with elemental analysis conducted through energy dispersive spectroscopy (EDS) integrated with the SEM. Additionally, phase analysis of commercial NMC622 and the synthesized samples (CPO24, CPO25, CPO28, CPO29, CPO30, CPO32, and CPO38) is performed using X-ray diffraction (XRD) patterns. This analysis is conducted with a Rigaku D/MAX 2000 X-ray diffractometer, employing Cu Kα radiation with a wavelength of 1.54 Å, and is scanned at a rate of 2°/min across the 2θ range of 10–90°.

Table 9. NMC622 samples and their synthesis conditions investigated in the Free4LIB project.

Sample code	Source	Synthesis	Conditions	Precursor
CP024	Torrecid	Solid-state	950 °C 10 h	Relithiation on NMC622 using recycled black mass CP021. Thermal process to integrate Li_2O in structure
CP025	Torrecid	Solid-state	950 °C 20 h	NMC622 synthesis using CP021and adjusting NiO, MnO_2/CoO. 95% recycling of CP021
CP028	Torrecid	Solid-state	950 °C 20 h	NMC622 synthesis using CP021and adjusting NiO, MnO_2/ CoO. 85% recycling of CP021
CP029	Torrecid	Solid-state	900 °C 8 h	NMC622 synthesis using CP021and adjusting NiO, MnO2/ CoO/ Li_2O. 68% recycling of CP021

Funded by the European Union

Views and opinions expressed are those of the author(s) only and do not necessarily reflect those of the European Union or CINEA. Neither the European Union nor the granting authority can be held responsible for them. This project has received funding from Horizon Europe research and innovation programme under Grant Agreement No.1069890

CP030	Torrecid	Hybrid	800 °C 15 h	NMC622 synthesis using a mixture of solid-state oxides and sulphates, co precipitation and thermal treatment
CP032	Torrecid	Hybrid	800 °C 15 h	NMC622 synthesis using 70% of CP021 and addition of NMC622 remaining precursors as sulphates. Coprecipitation on surface
CP038	Torrecid	Solid-state	950 °C 20 h	NMC622 using 75% of PR03 and adjusting rest of oxides $NiO/MNO_2/ CoO/Li_2O$
CPO21: Ultrasonic delaminated cathode active materials supplied from CARTIF				
PRE03: Ni, Mn, Co oxalate obtained by hydrometallurgical process supplied from CSIC				

Electrode preparation parameters (PVDF, carbon black and active material amount), coin cell assembling conditions (coin cell type, electrolyte volume, separator type) and electrochemical test conditions (galvanostatic charge/discharge tests, cyclic voltammetry and impedance) are given in Table 10.

Table 10. Electrode preparation, coin cell assembling and electrochemical test conditions for commercial NMC 622 and synthesized samples for Free4LIB project.

Commercial NMC622, CPO24, CPO25, CPO28, CPO29, CPO30, CPO32 and CPO38 electrode test specifications		
Electrode preparation	Binder type and amount	PVDF – 10 wt%
	Carbon black amount	Super P – 10 wt%
	Active material amount	80 wt.%
	Electrode thickness	Wet thickness ~300 µm
	Loading (mg/cm^2)	~5 mg/cm^2
Coin cell assembly	Coin cell type	2016
	Electrolyte type and volume	60 µl of 1M $LiPF_6$ in EC:DMC
	Half-cell or full-cell	Half-cell
	Separator	Celgard 2400
Electrochemical tests	Charge/discharge test parameters	Voltage range: 4.2-2.7 V vs. Li/Li^+ Current: C/20
	Cyclic Voltammetry	Voltage range: 4.2-2.7 V vs. Li/Li^+

Views and opinions expressed are those of the author(s) only and do not necessarily reflect those of the European Union or CINEA. Neither the European Union nor the granting authority can be held responsible for them. This project has received funding from Horizon Europe research and innovation programme under Grant Agreement No.1069890

		Scan rate: 0.1 mV/second
	Electrochemical impedance spectroscopy	Frequency range: 0.01 Hz- 100 kHz

6.2 Results

6.2.1 Morphological and Structural Characterization of NMC622 Cathode Powders Synthesized from Recycled Materials

Variations in the chemical valence and electronic configuration of transition metal (TM) elements typically occur with the intercalation and deintercalation of lithium ions. These alterations can lead to structural instabilities within the electrode material and may initiate undesirable side reactions at the electrode-electrolyte interface. The electronic and crystalline structures of these materials are pivotal in determining their electrochemical performance. Empirical electrochemical data on various nickel-manganese-cobalt (NMC) materials, each with different stoichiometric ratios of nickel (Ni), manganese (Mn), and cobalt (Co), reveal that nickel contributes to enhanced capacity but compromises safety features; cobalt improves rate capability but increases the material's cost; and manganese enhances structural stability, though it results in reduced capacity.

Figure 43 presents the XRD results of commercial NMC622 and synthesized samples from within the FREE4LIB project, focusing on the detailed 2Θ ranges of 18-19° and 43-46°. The peaks observed at 2Θ values of 18.18°, 36.8°, 38°, 38.4°, 44.5°, 48.7°, 58.7°, 64.5°, 65°, and 68.3° are characteristic of NMC622 and correspond to the (003), (101), (006), (012), (104), (105), (107), (108), (110), and (113) crystallographic planes, respectively. It is evident that all diffraction peaks can be indexed to the crystal planes of a well-defined hexagonal α-NaFeO2 structure within the R-3m space group (JCPDS No. 00-066-0854), with no impurities detected [2] [3]. The XRD patterns of the commercial NMC622 exhibit sharp and clear peaks, indicating the cathode powders are well-crystallized. Upon examining the XRD patterns of the CPO28, CPO29, CPO30, and CPO31 samples, it was observed that the peaks correspond to the (003) and (104) planes align well with those of the commercial NMC622. Nevertheless, the X-ray diffraction (XRD) patterns of the CPO24, CPO25, and CPO38 samples do not exhibit alignment with the commercial NMC622.

---

[2] *Wang, Q., Shen, C. H., Shen, S. Y., Xu, Y. F., Shi, C. G., Huang, L., ... & Sun, S. G. (2017). Origin of structural evolution in capacity degradation for overcharged NMC622 via operando coupled investigation. ACS applied materials & interfaces, 9(29), 24731-24742.*

[3] *Wang, L., Huang, B., Xiong, W., Li, H., Xiao, S., Chen, Q., ... & Yang, J. (2020). Improved solid-state synthesis and electrochemical properties of LiNi0. 6Mn0. 2Co0. 2O2 cathode materials for lithium-ion batteries Journal of Alloys and Compounds, 844, 156034.*

The normalized intensities (003) and (104) peaks, I(003)/I(104), for all samples are reported in Table 11, considered as a parameter to determine the cationic distribution in the in the α-$NaFeO_2$-type lattice[4]. The I(003)/I(104) ratio serves as an indirect indicator of cation mixing between Li^+ and Ni^{2+} within lithium layer. Typically, a higher I(003)/I(104) ratio signifies increased cation mixing. The presence of Ni2+ ions in the lithium layer not only reduce discharge capacity but also hinders the ionic diffusivity Li^+ [5]. An I(003)/I(104) ratio below 1.2 suggests the occurrence of undesirable cation mixing [6]. For the CPO24, CPO25, CPO28 and CPO38 samples, the I(003)/I(104) ratios are below 1.2, indicating the presence of unfavorable cation mixing. In contrast, the I(003)/I(104) ratios for CPO29, CPO30, and CPO32 exceed 1.2, which suggests a moderate level of cation mixing

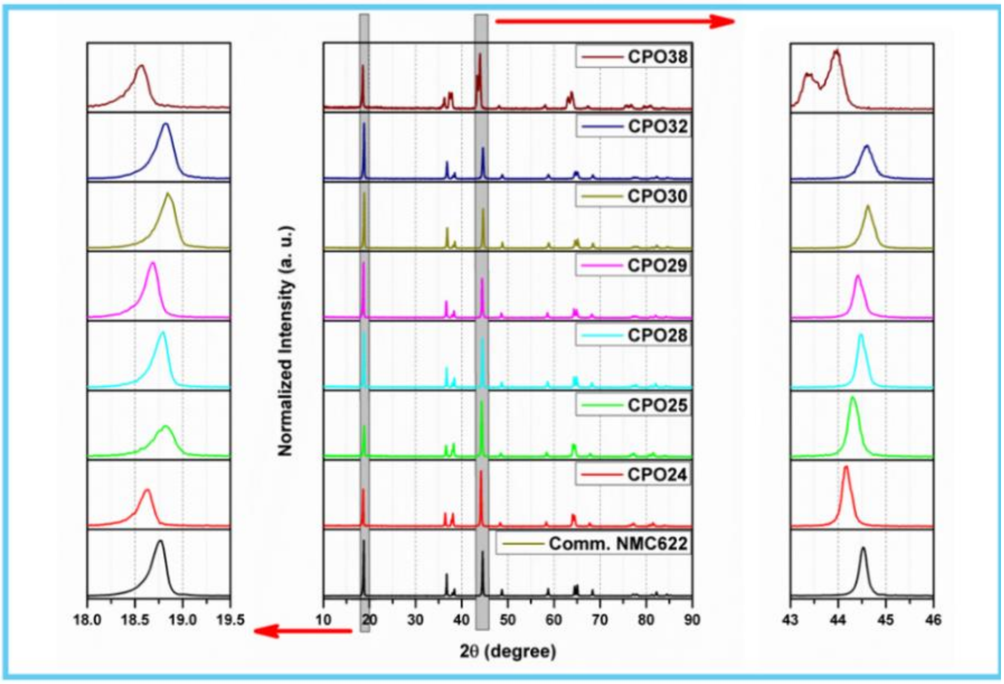

*Figure 43. XRD spectrum of commercial NMC811, CPO24, CPO25, CPO28, CPO29, CPO30, CPO32 and CPO38 samples with a detailed 2*Θ range of 18-19° and 43-46°.

Figure 44 presents the detailed XRD patterns within the 2Θ ranges of 35.5–39° and 62.5–65.5°. The focus is on the (006)/(012) peaks (at 2Θ values of 38° and 38.4°, respectively) and the (108)/(110) peaks (at 2Θ values of 64.5° and 65°, respectively). The sharpness of these peaks in commercial NMC622 indicates a high degree of crystallization, suggesting the

---

[4] *Zhang, X., Jiang, W. J., Mauger, A., Gendron, F., & Julien, C. M. (2010). Minimization of the cation mixing in $Li_{1+x}(NMC)_{1-x}O_2$ as cathode material. Journal of Power Sources, 195(5), 1292-1301.*

[5] *Noh, H. J., Youn, S., Yoon, C. S., & Sun, Y. K. (2013). Comparison of the structural and electrochemical properties of layered $Li[Ni_xCo_yMn_z]O_2$ (x= 1/3, 0.5, 0.6, 0.7, 0.8 and 0.85) cathode material for lithium-ion batteries. Journal of power sources, 233, 121-130.*

[6] *Azhari, L., Zhou, X., Sousa, B., Yang, Z., Gao, G., & Wang, Y. (2020). Effects of Extended Aqueous Processing on Structure, Chemistry, and Performance of Polycrystalline $LiNi_xMn_yCo_zO2$ Cathode Powders. ACS applied materials & interfaces, 12(52), 57963-57974.*

Funded by the European Union

Views and opinions expressed are those of the author(s) only and do not necessarily reflect those of the European Union or CINEA. Neither the European Union nor the granting authority can be held responsible for them. This project has received funding from Horizon Europe research and innovation programme under Grant Agreement No.1069890

presence of a well-ordered layered trigonal structure. In contrast, the (006)/(012) and (108)/(110) peaks for CPO24, CPO25, and CPO38 are shifted to lower angles and appear broader compared to those of NMC622, implying reduced crystallinity. For CPO28, CPO29, CPO30, and CPO32, the (006)/(012) and (108)/(110) peaks appear at the same 2Θ positions as in NMC622; however, the (108)/(110) peaks are broader, and the absence of a clear separation suggests lower crystallinity, which may result in decreased battery performance.

Table 11. Intensity ratio I(003)/I(104) of commercial NMC811, CPO24, CPO25, CPO28, CPO29, CPO30, CPO32 and CPO38 samples.

Samples	I (003)	I (104)	I (003) / I (104)
Commercial NMC 622	100	80.3407	1.2447
CP024	66.80088	100	0.6680
CP025	56.23043	100	0.5623
CP028	100	88.2451	1.1332
CP029	100	70.77136	1.4130
CP030	100	71.45481	1.3995
CP032	100	56.01599	1.7851
CP038	79.85515	100	0.7986

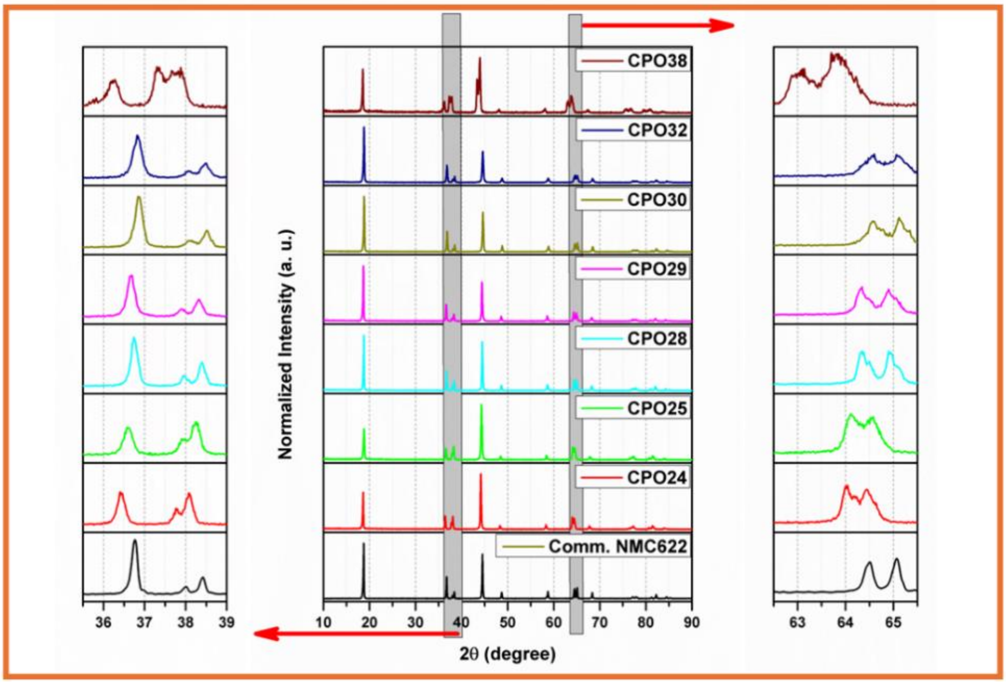

Figure 44. XRD spectrum of commercial NMC811, CPO24, CPO25, CPO28, CPO29, CPO30, CPO32 and CPO38 samples with a detailed 2Θ range of 35.5-39° and 62.5-65.5°.

Funded by the European Union

Views and opinions expressed are those of the author(s) only and do not necessarily reflect those of the European Union or CINEA. Neither the European Union nor the granting authority can be held responsible for them. This project has received funding from Horizon Europe research and innovation programme under Grant Agreement No.1069890

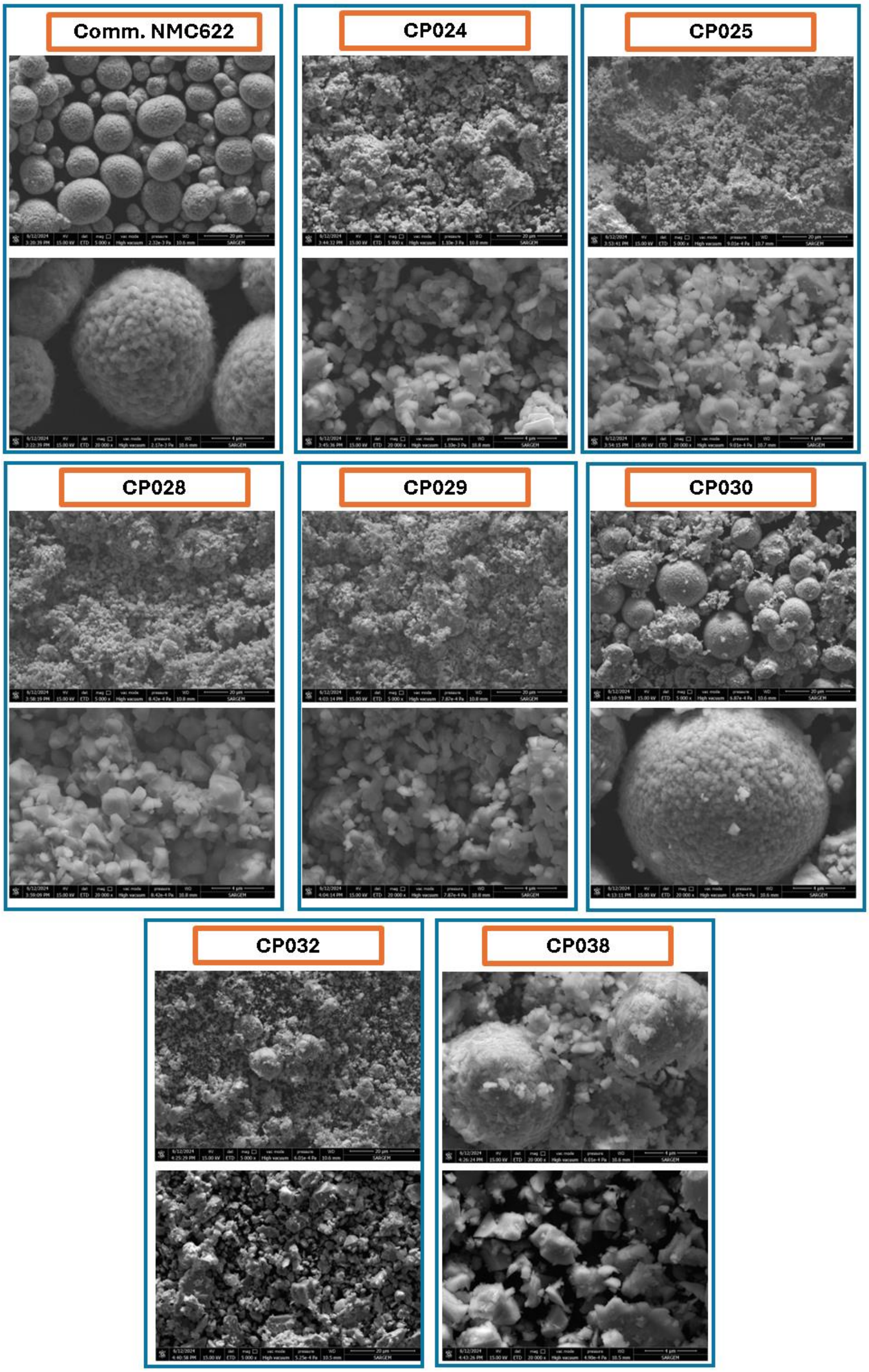

Figure 45. The SEM images of commercial NMC811, CPO24, CPO25, CPO28, CPO29, CPO30, CPO32 and CPO38 samples.

Funded by the European Union

Views and opinions expressed are those of the author(s) only and do not necessarily reflect those of the European Union or CINEA. Neither the European Union nor the granting authority can be held responsible for them. This project has received funding from Horizon Europe research and innovation programme under Grant Agreement No.1069890

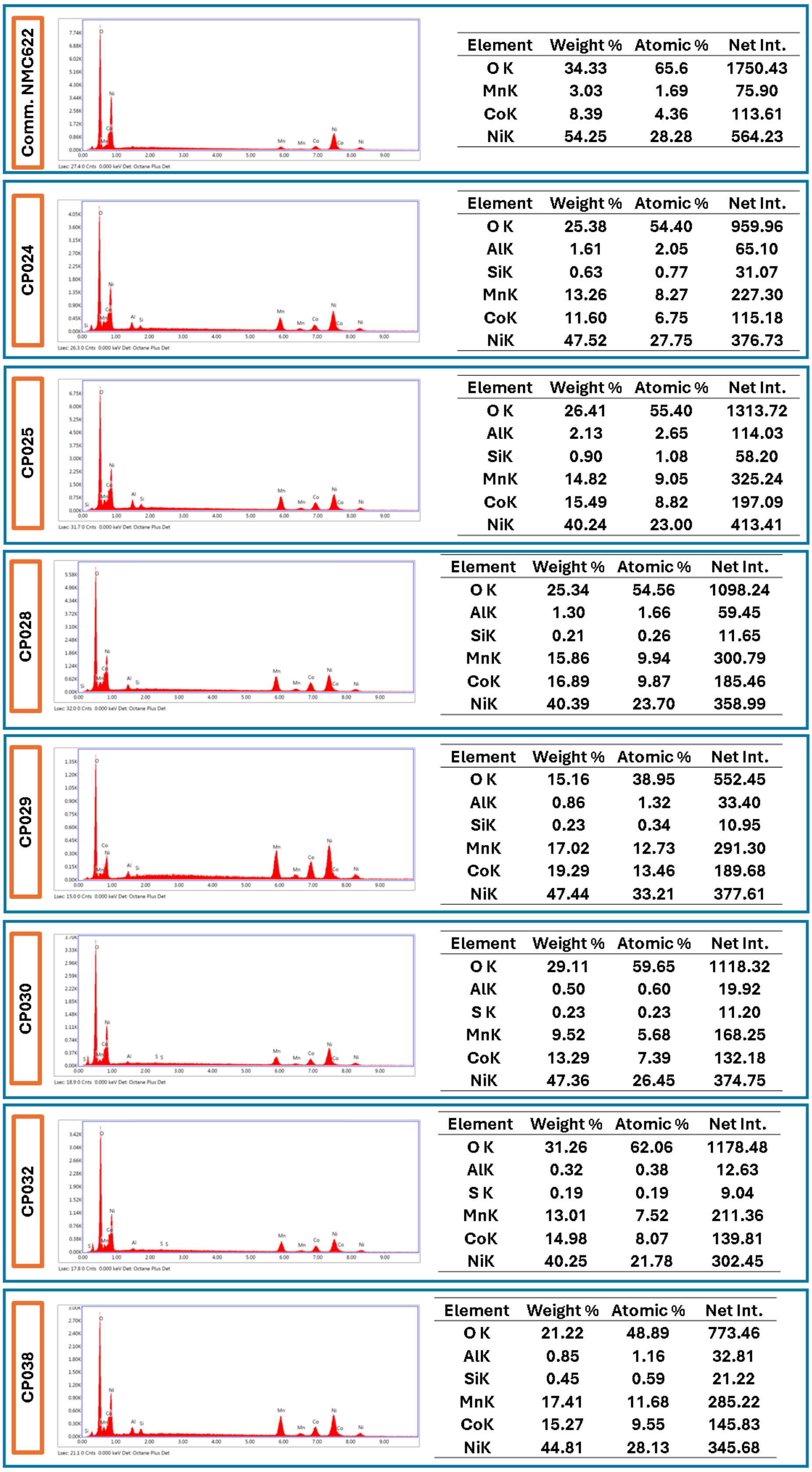

Comm. NMC622

Element	Weight %	Atomic %	Net Int.
O K	34.33	65.6	1750.43
MnK	3.03	1.69	75.90
CoK	8.39	4.36	113.61
NiK	54.25	28.28	564.23

CP024

Element	Weight %	Atomic %	Net Int.
O K	25.38	54.40	959.96
AlK	1.61	2.05	65.10
SiK	0.63	0.77	31.07
MnK	13.26	8.27	227.30
CoK	11.60	6.75	115.18
NiK	47.52	27.75	376.73

CP025

Element	Weight %	Atomic %	Net Int.
O K	26.41	55.40	1313.72
AlK	2.13	2.65	114.03
SiK	0.90	1.08	58.20
MnK	14.82	9.05	325.24
CoK	15.49	8.82	197.09
NiK	40.24	23.00	413.41

CP028

Element	Weight %	Atomic %	Net Int.
O K	25.34	54.56	1098.24
AlK	1.30	1.66	59.45
SiK	0.21	0.26	11.65
MnK	15.86	9.94	300.79
CoK	16.89	9.87	185.46
NiK	40.39	23.70	358.99

CP029

Element	Weight %	Atomic %	Net Int.
O K	15.16	38.95	552.45
AlK	0.86	1.32	33.40
SiK	0.23	0.34	10.95
MnK	17.02	12.73	291.30
CoK	19.29	13.46	189.68
NiK	47.44	33.21	377.61

CP030

Element	Weight %	Atomic %	Net Int.
O K	29.11	59.65	1118.32
AlK	0.50	0.60	19.92
S K	0.23	0.23	11.20
MnK	9.52	5.68	168.25
CoK	13.29	7.39	132.18
NiK	47.36	26.45	374.75

CP032

Element	Weight %	Atomic %	Net Int.
O K	31.26	62.06	1178.48
AlK	0.32	0.38	12.63
S K	0.19	0.19	9.04
MnK	13.01	7.52	211.36
CoK	14.98	8.07	139.81
NiK	40.25	21.78	302.45

CP038

Element	Weight %	Atomic %	Net Int.
O K	21.22	48.89	773.46
AlK	0.85	1.16	32.81
SiK	0.45	0.59	21.22
MnK	17.41	11.68	285.22
CoK	15.27	9.55	145.83
NiK	44.81	28.13	345.68

Figure 46. EDS results of commercial NMC811, CPO24, CPO25, CPO28, CPO29, CPO30, CPO32 and CPO38 samples.

Funded by the European Union

Views and opinions expressed are those of the author(s) only and do not necessarily reflect those of the European Union or CINEA. Neither the European Union nor the granting authority can be held responsible for them. This project has received funding from Horizon Europe research and innovation programme under Grant Agreement No.1069890

Figure 45 and 46 illustrates the SEM images at low (X5000) and high magnifications (X20000), along with the corresponding elemental distribution results. The commercial NMC622 sample exhibits the typical densely packed, loosely agglomerated spherical particles with a uniform size distribution ranging from 5 to 10 µm. EDS analysis confirms the absence of any contaminant elements in the commercial NMC622, ensuring the material's high crystallinity, stable electrochemical performance, and optimal battery efficiency. In contrast, the SEM images of CPO24 reveal the presence of submicron powder, with EDS analysis detecting contaminant elements such as Al and Si. The presence of these elements can disrupt the crystal structure, reduce thermal stability, and lower the electrochemical performance of the material, all of which may contribute to the structural disorder observed in the XRD results shown in Figures 43 and 44. Similarly, CPO25 also consists of Al and Si contaminants, along with submicron grain sizes, which further indicate a deterioration in material quality. These contaminants could potentially lead to diminished battery performance due to their negative impact on crystallinity and conductivity. For CPO28 and CPO29, although lower amounts of Si and Al contaminants were detected compared to CPO24 and CPO25, their grain structure, as observed in the SEM images, closely resembles that of commercial NMC622. However, the presence of even trace amounts of these contaminants can still pose risks to the overall battery performance. For CPO30 and CPO32, the presence of Si contaminants has been eliminated, and the Al content has significantly decreased, leading to a more stable crystalline structure. The SEM images suggest that these samples consist of a blend of commercial powders, displaying a coexistence of approximately 10 µm structures and submicron particles, which is favourable for maintaining performance integrity. In the case of CPO38, the particles exhibit an angular morphology rather than the spherical grain structure typical of NMC622, as confirmed by the XRD data in Figures 43 and 44. The absence of spherical grains and the altered morphology suggest significant deviations from the desired structure, likely contributing to inferior electrochemical performance." without any contaminant elements.

6.2.2 Electrochemical Characterization of NMC622 Cathode Powders Synthesized from Recycled Materials

Figure 47 and Figure 48 presents the galvanostatic charge/discharge curves, cycle performance, and cyclic voltammetry (CV) curves of commercial NMC622, as well as the CPO24, CPO25, CPO28, CPO29, CPO30, CPO32, and CPO38 samples.

Funded by the European Union

Views and opinions expressed are those of the author(s) only and do not necessarily reflect those of the European Union or CINEA. Neither the European Union nor the granting authority can be held responsible for them. This project has received funding from Horizon Europe research and innovation programme under Grant Agreement No.1069890

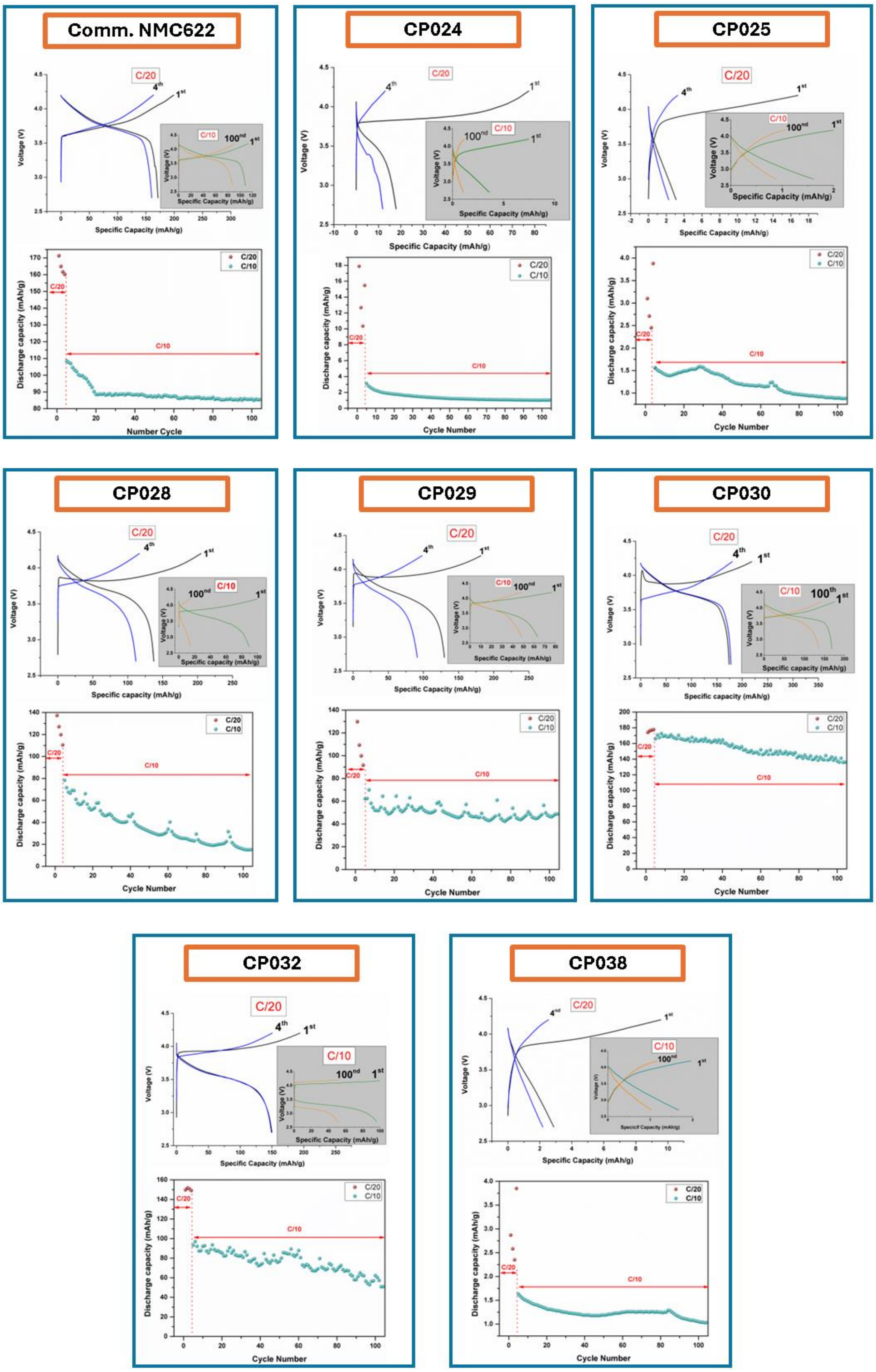

Figure 47. Electrochemical galvanostatic charge/discharge curves and cycle performances of commercial NMC811, CPO24, CPO25, CPO28, CPO29, CPO30, CPO32 and CPO38 samples.

Funded by the European Union

Views and opinions expressed are those of the author(s) only and do not necessarily reflect those of the European Union or CINEA. Neither the European Union nor the granting authority can be held responsible for them. This project has received funding from Horizon Europe research and innovation programme under Grant Agreement No.1069890

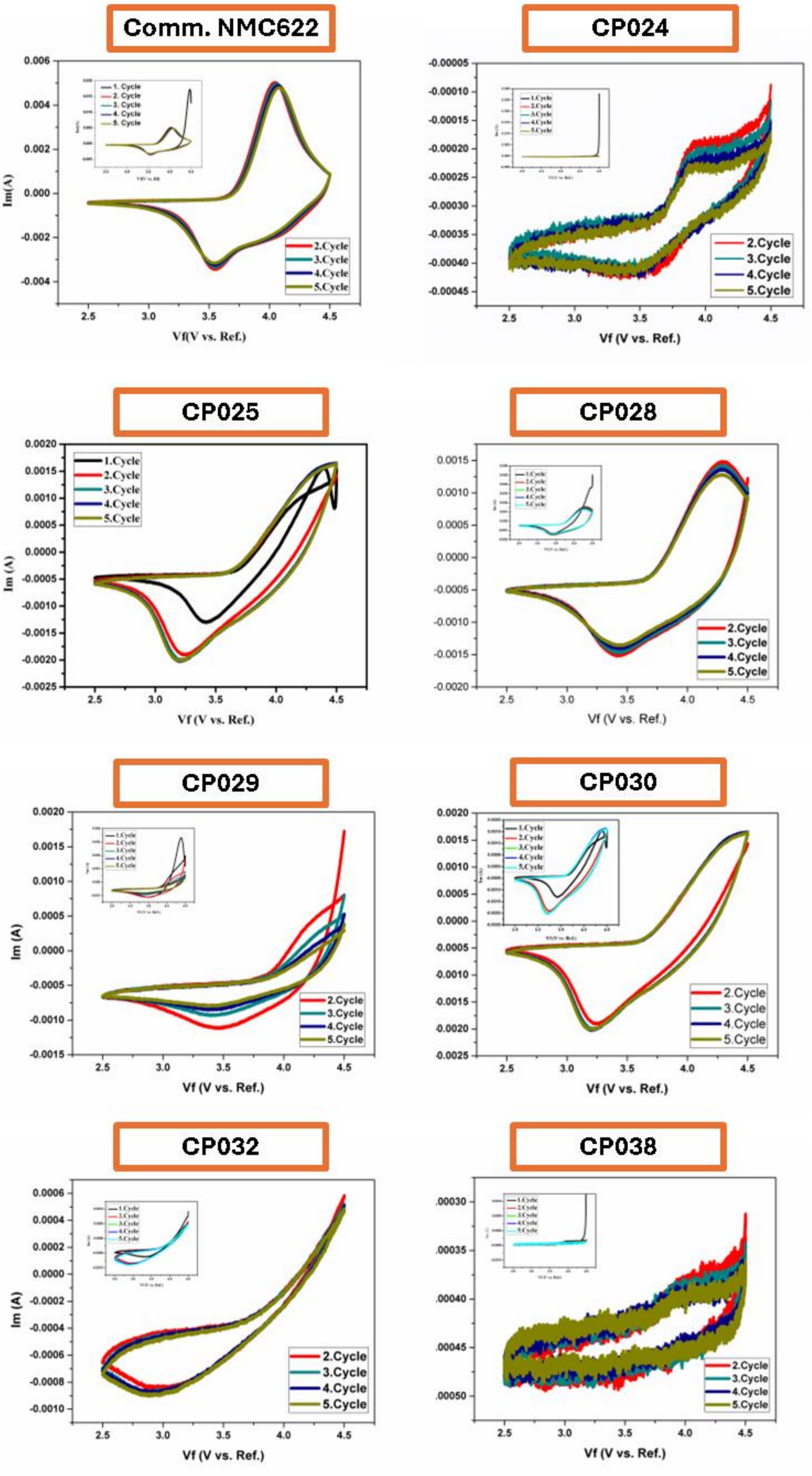

Figure 48. CV curves of commercial NMC811, CPO24, CPO25, CPO28, CPO29, CPO30, CPO32 and CPO38 samples.

Views and opinions expressed are those of the author(s) only and do not necessarily reflect those of the European Union or CINEA. Neither the European Union nor the granting authority can be held responsible for them. This project has received funding from Horizon Europe research and innovation programme under Grant Agreement No.1069890

In the CV curves of commercial NMC622, an oxidation peak is observed in the anodic scan at approximately 4.03 V, corresponding to the lithium insertion process. In the cathodic scan, two distinct reduction peaks are evident: a minor peak at around 4.03 V and a sharp peak at approximately 3.53 V. The minor reduction peak indicates multiphase transitions between two hexagonal structures, while the sharp peak is associated with a redox reaction. Electrochemical galvanostatic charge/discharge tests were conducted at a C/20 rate for the first four cycles, followed by a C/10 rate for the subsequent 100 cycles (4 cycles at C/20 + 100 cycles at C/10 = 104 total cycles). The initial discharge capacities were calculated as 171, 17, 3, 137, 129, 174, 149, and 3 mAh g^{-1} for commercial NMC622, CPO24, CPO25, CPO28, CPO29, CPO30, CPO32, and CPO38, respectively. Comparing the initial discharge capacities, it is evident that the CPO24, CPO25, and CPO38 samples are practically not feasible as active cathode materials for LIBs. In contrast, CPO28, CPO29, CPO30, and CPO32 demonstrated promising initial discharge capacities, suggesting their potential as viable candidates for active cathode materials in LIBs. However, after 104 cycles, the discharge capacities were found to be 85, 1, 0.8, 15, 48, 136, 51, and 1 mAh g^{-1} for commercial NMC622, CPO24, CPO25, CPO28, CPO29, CPO30, CPO32, and CPO38, respectively. These results indicate that CPO29, CPO30, and CPO32 exhibit sufficient stability and capacity retention, making them suitable for scaling up to pouch cells in the FREE4LIB project.

Electrochemical Impedance Spectroscopy (EIS) measurements were conducted within the frequency range of 0.01 Hz to 100 kHz, employing a excitation voltage of 10 mV shown in Figure 49. The semicircles observed at medium frequencies correspond to the charge-transfer resistance (Rct), reflecting the kinetic reaction occurring at the interface between the electrolyte and the electrode. CPO32 is display higher charge discharge transfer resistance than that of CPO24, CPO25, CPO28, CPO29, CPO30 and CPO32. The Warburg impedance describes the diffusion of ions through the electrolyte or the solid-state material. In the Nyquist plot, the Warburg impedance typically appears as a 45-degree line at the low-frequency region, representing the diffusion process of Li-ions into the electrodes. Warburg impedance arises because of the finite diffusion rate of lithium ions during charge/discharge. It can be described by a series of RC (resistor-capacitor) networks in a distributed fashion, simulating the ion transport's resistive and capacitive nature. This diffusion is slow, leading to a distinctive slope in the Nyquist plot. CPO24, CPO25, CPO30, CPO32 and CPO38 shows good Warburg curve when compared to other samples.

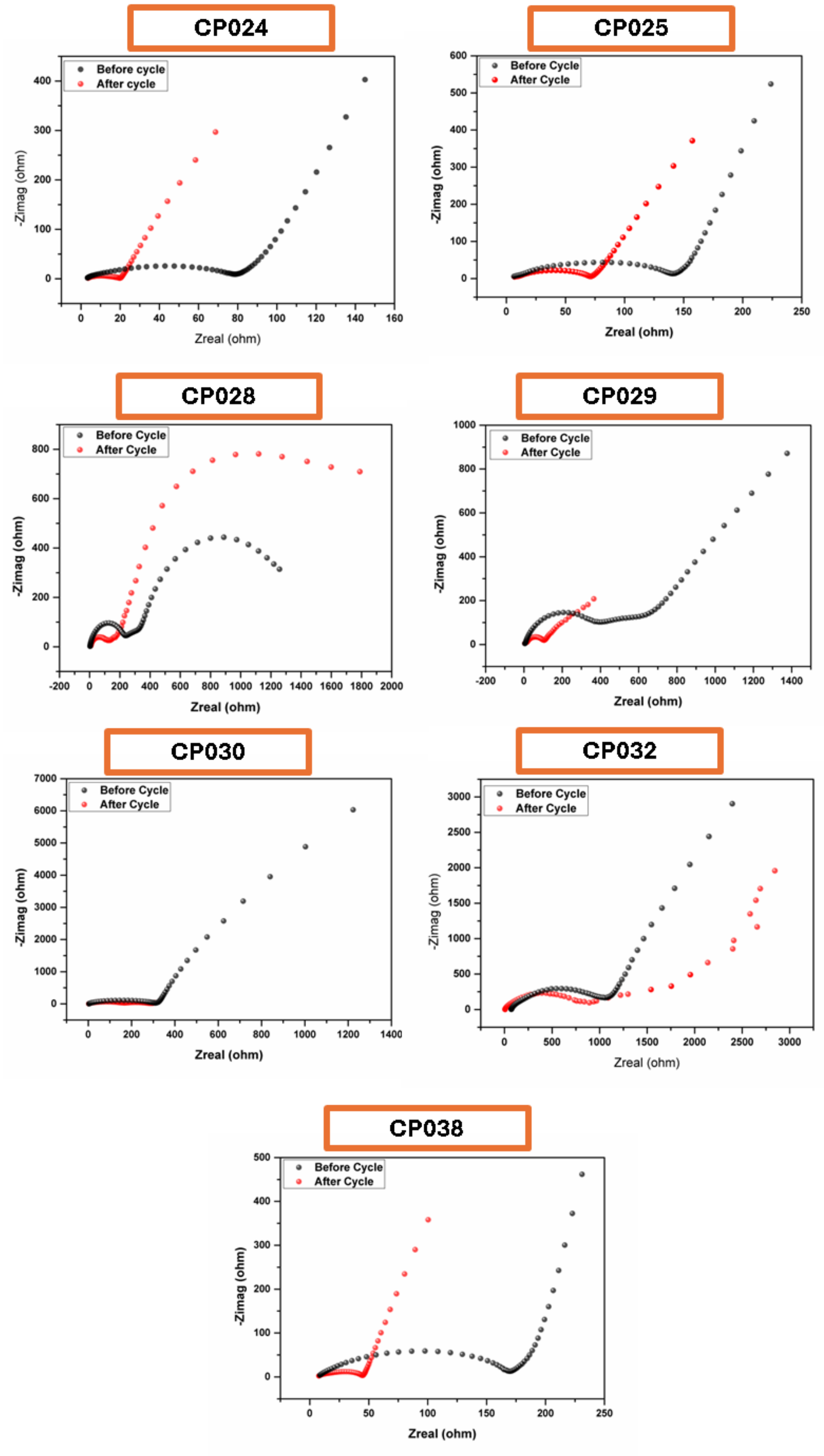

Figure 49. Nyquist plots of CPO24, CPO25, CPO28, CPO29, CPO30, CPO32 and CPO38 before and after five cycle CV tests.

Views and opinions expressed are those of the author(s) only and do not necessarily reflect those of the European Union or CINEA. Neither the European Union nor the granting authority can be held responsible for them. This project has received funding from Horizon Europe research and innovation programme under Grant Agreement No.1069890

7. Electrochemical and morphological investigation of spinel LNMO cathodes synthesized from recovered materials

7.1 Morphological and Structural Characterization of spinel LNMO Cathodes

$LiNi_{0.5}Mn_{1.5}O_4$ (LNMO) is considered one of the most promising cathode materials for next-generation batteries. The theoretical capacity of the material is 147 mAh g^{-1}, and it operates at high voltages, in the voltage range of 3.5 to 4.9 V vs Li^+/Li, maximizing energy and power at the electrode level. Additionally, it is cheap and less toxic than state-of-the-art (NMC622, NMC811) cathode materials since it does not contain cobalt. The most promising phase of LNMO from the electrochemical point of view is the cubic phase with space group Fd-3m: the O atoms are arranged in a cubic close-packed lattice, the Li atoms occupy the 8a tetrahedral sites, and the Mn and Ni are disordered within the 16d octahedral sites. The spinel LNMO samples investigated in the FREE4LIB project, and their synthesis conditions are shown in Table 12. Samples are divided into three groups. The first category comprises the CP035 sample, which serves as the reference for comparison with other samples; this sample is commercially available and sourced from the TOPSOE brand. The second category includes the CP031 sample, synthesized by the company TORRECID using commercial precursors. The third category consists of the CP012, CP014, and CP037 samples, which were also synthesized by TORRECID, but using a combination of recycled and commercial precursors.

Table 12. Spinel LNMO samples and their synthesis conditions investigated in the FREE4LIB project.

Sample code	Source	Synthesis	Conditions	Precursor type
CP012	Torrecid	Solid-state	Initially, the manganese and nickel precursors were subjected to calcination at 900°C for 5 hours, followed by annealing of the resulting powder with Li_2CO_3 at 800°C for 12 hours.	Recycled
CP014	Torrecid	Hydrothermal	Calcination of acetates at 800°C for 20h	Recycled

Views and opinions expressed are those of the author(s) only and do not necessarily reflect those of the European Union or CINEA. Neither the European Union nor the granting authority can be held responsible for them. This project has received funding from Horizon Europe research and innovation programme under Grant Agreement No.1069890

CP031	Torrecid	Hybrid	Calcination of sulfates at 800°C for 20h	Commercial
CP035	Commercial	Unknown	Unkown	Unknown
CP037	Torrecid	Hybrid	Solid sate using 59 % PRE04 in LNMO synthesis 2 steps first 900 ºC, lithiation at 800 ºC. PRE04 is Ni/Mn	Recycled

Figure 50 presents the X-ray diffraction (XRD) patterns for the analysed samples (refer to Table 12). The primary diffraction peaks for each pattern can be indexed using a cubic unit cell with a lattice parameter of approximately 8.2(2) Å, consistent with the reference code 01-080-2126 (ICSD Collection Code: 70023). The uniformity in unit cell parameters across all indexed samples suggests that there are no significant differences in sample stoichiometry, such as lithium stoichiometry, among the samples. However, Sample CP037, depicted by the green line in Figure 50, exhibits minor additional peaks near the main reflections that could not be precisely identified. These un-indexed reflections are likely indicative of an impurity phase, which is presumably related to sample contamination during the synthesis process, as detailed in Table 12.

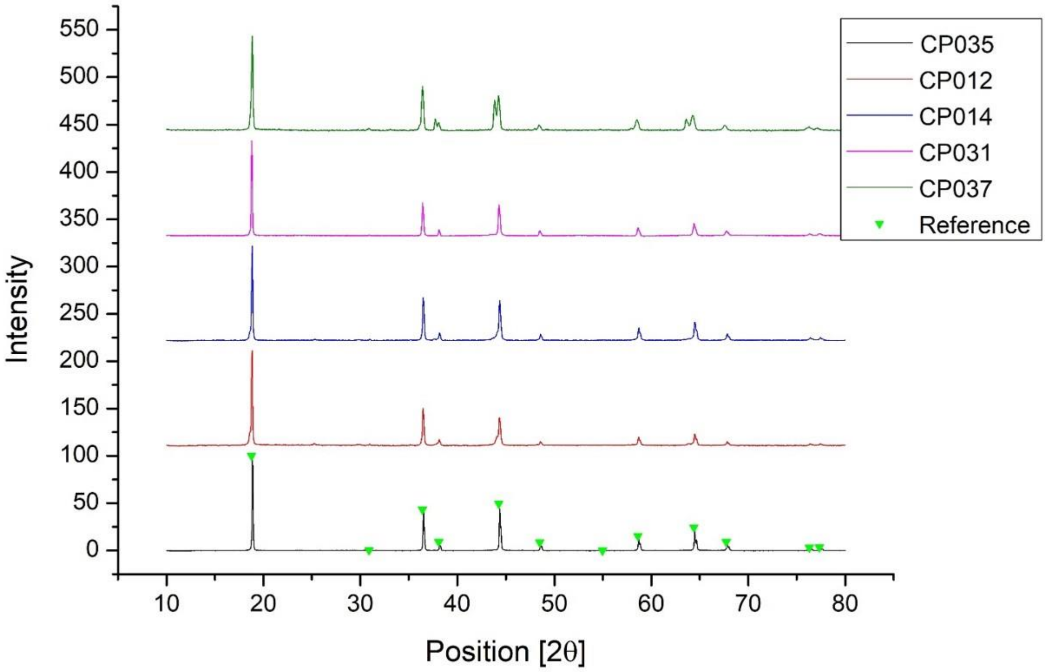

Figure 50. XRD patterns of samples specified in Table 12 From top to bottom: CP037, CP031, CP014, CP012 and CP35. Theoretical peak positions are green marks in the bottom pattern and correspond to reference 01-080-2126.

Samples were further analyzed using Scanning Electron Microscopy (SEM), with the results depicted in Figure 51. The SEM images of Sample CP035 reveal two distinct particle

Views and opinions expressed are those of the author(s) only and do not necessarily reflect those of the European Union or CINEA. Neither the European Union nor the granting authority can be held responsible for them. This project has received funding from Horizon Europe research and innovation programme under Grant Agreement No.1069890

morphologies: one type comprises secondary spherical particles, while the other is characterized by polyhedral shapes, representing primary particles. The spherical particles exhibit an average diameter of 5.4 µm. In contrast, the polyhedral particles exhibit a wide range of sizes and shapes, which posed challenges for precise quantification. For the other samples, namely CP012, CP014, CP031, and CP037, the predominant particle forms are polyhedral or amorphous, with noticeable agglomeration, particularly evident in CP012 and CP014. This observation is consistent regardless of whether commercial or recycled precursors were utilized in the synthesis.

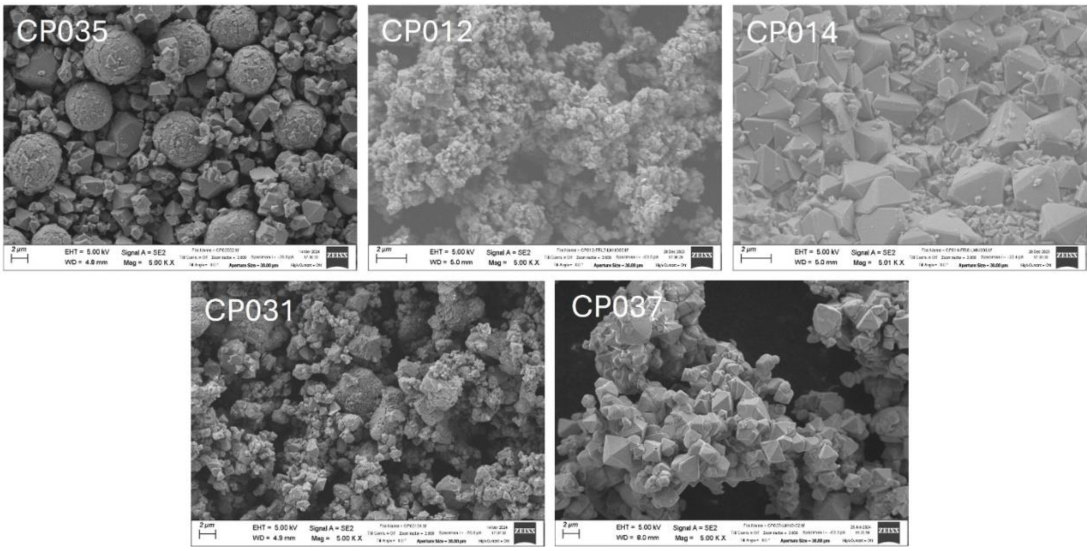

Figure 51. SEM images of the samples specified in Table 12.

7.2 Electrochemical Characterization of spinel LNMO Cathodes

Electrochemical measurements, including Cyclic Voltammetry, galvanostatic charge/discharge, and electrochemical impedance spectroscopy, were conducted using Al-coated 2032 coin cells to minimize corrosion at high voltages > 4.5 V. Cyclic Voltammetry (CV) results in the voltage window 3.5-4.9 V and scan rate 50 μVs^{-1} are shown in Figure 52. The typical CV profile for the cubic LNMO is shown in Figure 52a. The main anodic/cathodic contributions are highlighted in the CV curves, as discussed in Y. Xue et al. [7]. There are two anodic peaks around 4.7-4.9 V, which are attributed to a Ni^{2+}/Ni^{4+} redox couple, and the weak peaks at 4.0 V are attributed to a Mn^{3+}/Mn^{4+} redox couple. The peaks are reversible during reduction. These redox reactions are clearly identified in the commercial sample CP035, as shown in Figure 52b.

---

[7] *Xue, Y., Wang, Z., Zheng, L., Yu, F., Liu, B., Zhang, Y., & Ke, K. (2015). Investigation on preparation and performance of spinel* $LiNi_{0.5}Mn_{1.5}O_4$ *with different microstructures for lithium-ion batteries. Scientific Reports, 5(1), 13299.*

Views and opinions expressed are those of the author(s) only and do not necessarily reflect those of the European Union or CINEA. Neither the European Union nor the granting authority can be held responsible for them. This project has received funding from Horizon Europe research and innovation programme under Grant Agreement No.1069890

For sample CP012, Figure 52c, there are no visible peaks related to the oxidation or reduction of Mn and Ni. This typical profile is generally observed in highly resistive materials with no electrochemical activity. Sample CP014, Figure 52d, displays a similar profile to the reference sample, as it presents the same range of specific current and exhibits the oxidation and reduction peaks of Mn and Ni. The oxidation peaks of Ni are in the range of 4.7 V to 4.8 V, and Mn's peak is at 4.0 V. Finally, the reduction peaks of Ni and Mn are in the ranges of 4.5 V and 3.9 V, respectively. Regarding sample CP031, Figure 52e, the peaks associated with the oxidation of Ni are not clearly defined, but those associated with its reduction are clearly present. In contrast, the oxidation and reduction peaks of Mn are clearly visible and are within the expected ranges for this redox reaction to occur. Sample CP037, Figure 52f, shows poor reproducibility between cycles; as cycling progresses, these peaks decrease in intensity and shift to higher potential. Overall, if the peak intensity (mAg-1) for the Ni^{2+}/Ni^{4+} redox activity is considered, the following trend can be observed, from low to high current response: CP012 > CP037 > CP031 > CP014 > CP035 (commercial). From these results, we selected the three best-performing samples, and new coin cells were assembled for galvanostatic charge/discharge and electrochemical impedance spectroscopy studies.

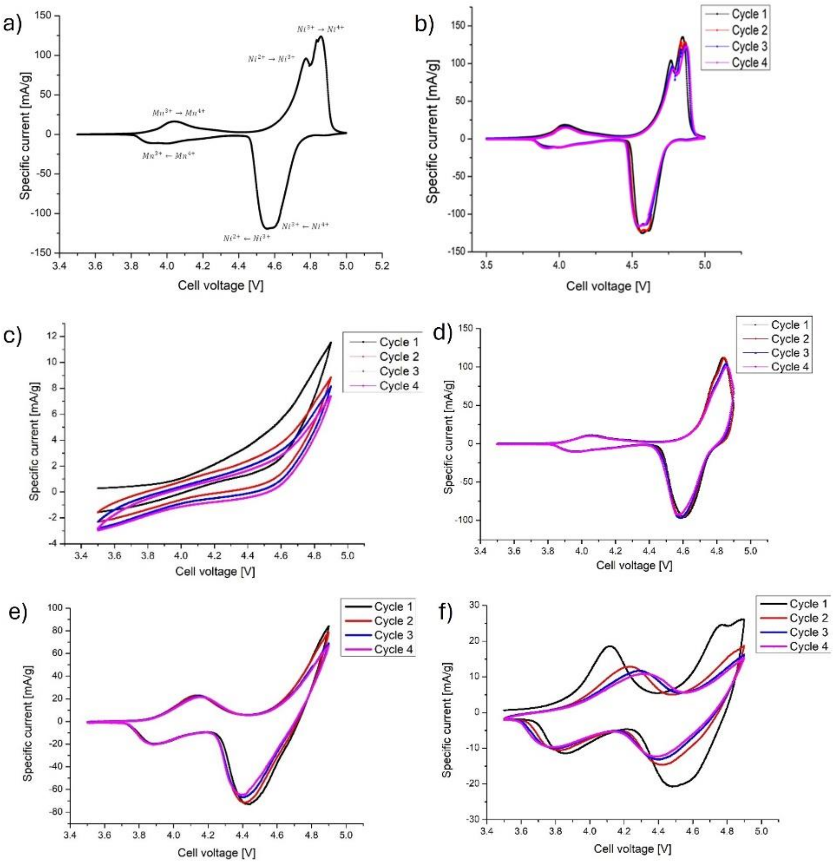

Figure 52. Cyclic Voltammetry of LNMO half-cells at room temperature measured at 50µVs-1: a) as published1, b) CP035, c) CP012, d) CP014, e) CP031, f) CP037.

The following protocol was carried out: 1) measurement of the cell's impedance at its equilibrium potential, 2) two formation cycles at C/10 to activate the cells, 3) cell charging

Views and opinions expressed are those of the author(s) only and do not necessarily reflect those of the European Union or CINEA. Neither the European Union nor the granting authority can be held responsible for them. This project has received funding from Horizon Europe research and innovation programme under Grant Agreement No.1069890

up to 4 V at C/10 and relaxed for impedance measurement, 4) 1 charge/discharge cycle at C/2, 5) cell charging up to 4 V at C/10 and relaxed for impedance measurement, and then repetition from 3) at different C-rates. Results are presented in Figure 53.

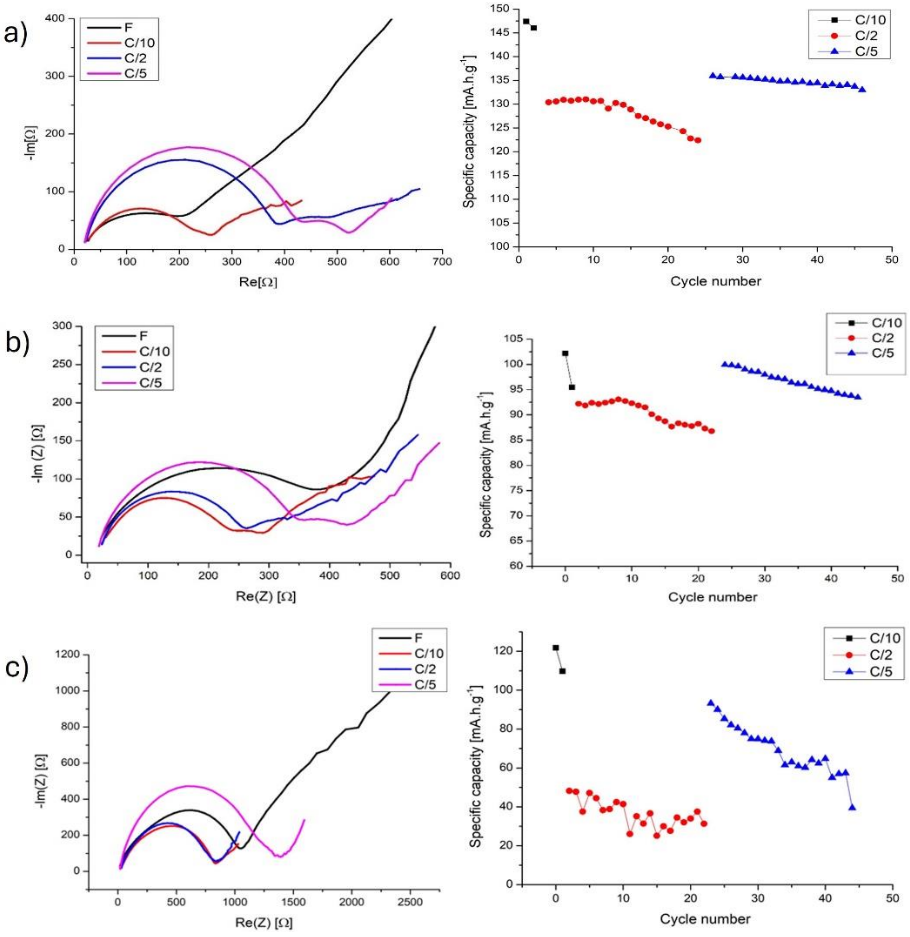

Figure 53. Electrochemical impedance spectroscopy and galvanostatic charge/discharge measurements following protocol defined above of LNMO half-cells at room temperature: a) CP035, b) CP014, c) CP031.

The commercial sample CP035 delivers a specific discharge capacity of 147 mAhg-1 during activation (2 cycles at C/10), and 134 and 128 mAh g^{-1} at C/5 and C/2, respectively. The associated impedances measured at 4 V as a function of C-rate are 229, 374, and 412 Ω, respectively. Sample CP014 delivers a specific capacity of 98 mAh g^{-1} at C/10 during activation and 96 and 90 mAhg-1 at C/5 and C/2, respectively. The associated impedances measured at 4 V as a function of C-rate are 233, 252, and 343 Ω, respectively. Sample CP031 delivers a specific capacity of 115 $mAhg^{-1}$ at C/10, and 70 and 30 mAhg-1 at C/5 and C/2, respectively. The associated impedances measured at 4 V as a function of C-rate are 884, 817, and 1260 Ω. The resistance values considered in this study were extracted from the low-frequency Z' intercept of the charge-transfer semicircle.

Regarding LNMO cycling performance, new coin cells were assembled, activated at C/10 for 2 cycles, and then galvanostatically cycled at C/10. The samples analyzed were CP035,

Funded by the European Union

Views and opinions expressed are those of the author(s) only and do not necessarily reflect those of the European Union or CINEA. Neither the European Union nor the granting authority can be held responsible for them. This project has received funding from Horizon Europe research and innovation programme under Grant Agreement No.1069890

CP014, CP031, and CP037. Results are presented in Figure 54. Samples CP031 and CP014 show the best performance in capacity retention: 90 % after 100 cycles for CP031 and 90 % for CP014 after 55 cycles. Sample CP037 only delivers 30 % of its initial capacity after 30 cycles.

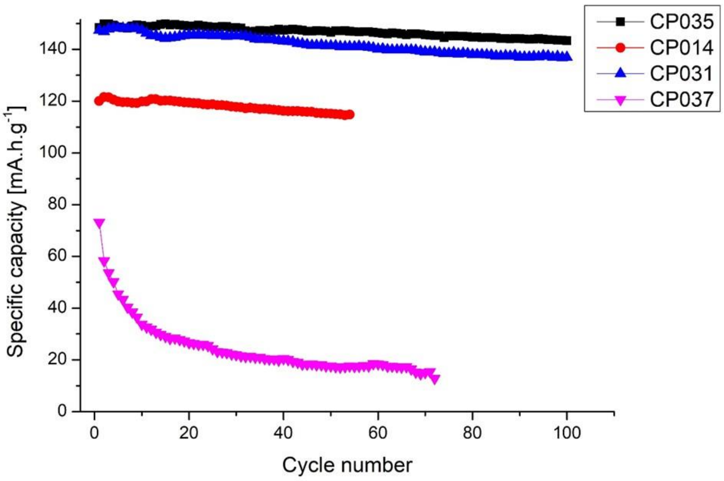

Figure 54. Specific discharge capacity vs. cycle number at C/10 current density for the samples CP035 (black trace), CP014 (red trace), CP031 (blue trace), and CP037 (pink trace).

From a structural point of view, all samples analysed show cubic structures with similar lattice parameters a ~ 8.2(2) Å. All appear to be phase pure by XRD except CP037, which contains some unidentified peaks most probably associated with Co contamination as reported by provided partner. At the micro/nano-structural level, SEM pictures show significant differences among powders, especially compared to the commercial ones, in which a well-homogeneous morphology of spherical and polyhedral particles is observed. Processed powders using either commercial or recycled precursors show a random distribution of polyhedral and amorphous particles with no clear correlation with the synthesis procedure. Regarding cathode performance, LNMO samples with codes CP014 and CP031 are the best-performing ones in the various tests conducted, including C-rate, impedance, and capacity retention. Sample CP014 was synthesized via a hydrothermal process using recycled precursors: it delivers lower discharge capacities (98 mAh g^{-1} at C/10) than the commercial one (147 mAh g^{-1} at C/10), and a capacity retention of 90 % after 55 cycles. Sample CP031 was synthesized via a hybrid process using commercial precursors; its performance is more like the commercial sample, CP035, delivering 115 mAh g^{-1} at C/10 and a capacity retention of 90% after 100 cycles. Our results indicate the potential of the powders obtained from the CP014 and CP031 precursors for upscaling.

Views and opinions expressed are those of the author(s) only and do not necessarily reflect those of the European Union or CINEA. Neither the European Union nor the granting authority can be held responsible for them. This project has received funding from Horizon Europe research and innovation programme under Grant Agreement No.1069890

8. Electrochemical and morphological investigation of recycled graphite from black mass

8.1 Morphological and structural characterization of recycled graphite from black mass

The graphite is recycled after some pyro- and hydrometallurgical process within this deliverable. Details regarding the process utilized to the recovered graphite after recycling processes are provided with their codes in Table 13.

Table 13. Recycled graphite powder samples with their obtained conditions.

Sample code	Classifications
BM01-1	BM from ACCUREC after hydrometallurgical treatment (leached H_2SO_4+O_3)
BM01-2	BM from ACCUREC after combined pyro-hydrometallurgical treatment (thermal treatment+water leaching+HCl leaching)
BM03-1	BM from FRAUNHOFER after hydrometallurgical treatment (leached H_2SO_4+O_3)
BM03-2	BM from FRAUNHOFER after combined pyro-hydrometallurgical treatment (thermal treatment+water leaching+HCl leaching)

Figure 55 presents the XRD patterns of the recycled graphite samples BM01-1, BM01-2, BM03-1, and BM03-2. The diffraction peaks at 2Θ angles of 26.5°, 42.2°, and 54.7° correspond to the (002), (100), and (004) planes of graphite, respectively, as referenced by JCPDS No. 00-041-1487. The XRD patterns indicate that all samples exhibit a high degree of crystallinity, with minor shifts in the 2Θ angles suggesting that the crystalline structure of the graphite has been largely preserved post-recycling. Despite the presence of some impurities, such as Al_2O_3 and NMC, across all samples, BM03-1 shows a notably higher amount of NMC impurity. It is crucial to note the limitations of XRD detection, as contaminants present in quantities below 5 wt.% may not be detectable.

Views and opinions expressed are those of the author(s) only and do not necessarily reflect those of the European Union or CINEA. Neither the European Union nor the granting authority can be held responsible for them. This project has received funding from Horizon Europe research and innovation programme under Grant Agreement No.1069890

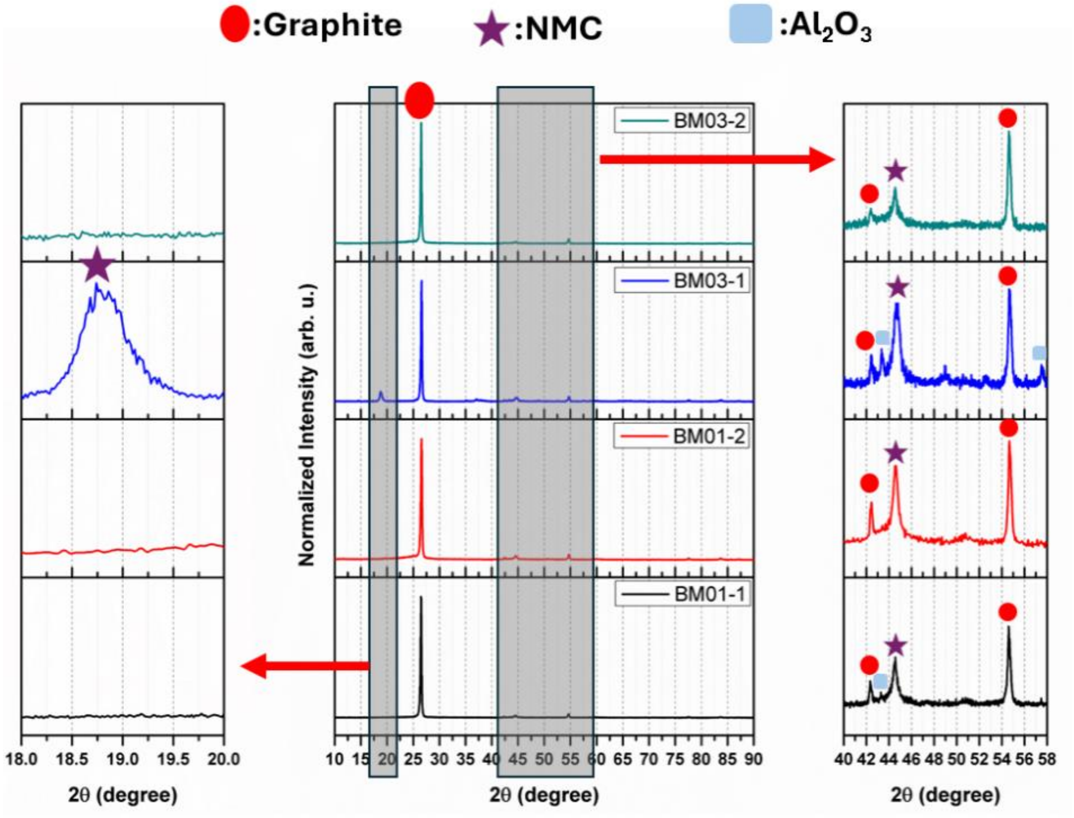

Figure 55. XRD curves of recycled graphite.

The corresponding SEM images of BM01-1, BM01-2, BM03-1, and BM03-2, shown in Figure 56 and captured in back-scattered electron mode, reveal compositional differences in the specimens (differences in average atomic number). The electrodes exhibit a uniform distribution of graphite particles, varying in size from 5 to 10 µm. The elemental distribution of specific zones (marked in Figure 56) is presented in Table 14, with atomic percentages obtained from the energy-dispersive spectrometer equipped with the SEM. The SEM image of BM01-1 shows both lighter and darker zones. The EDS results for zone A1 indicate a high atomic percentage of aluminium, suggesting that some Al_2O_3 residues remain in the sample after the recycling process. Zones A1 and A2 also show the presence of copper and sulphur contaminants, which may have been introduced during sulfuric acid treatment (or due to sulphur in possible electrolyte additives) and from the copper foil [8]. In contrast, zone A3 contains only carbon, with no detectable contamination. However, zone A4 shows the presence of Al, P, and O contaminants, likely originating from the aluminium foil and the electrolyte ($LiPF_6$ salt). Although the EDS results for the BM01-2 sample show only phosphorus contamination in zone B2, BM03-1 exhibits additional contaminants, including Co, Ni, Mn, F, and Al. Lithium cannot be measured by EDS analysis due to its low atomic

---

[8] *Chernyaev, A., Kobets, A., Liivand, K., Tesfaye, F., Hannula, P. M., Kallio, T., ... & Lundström, M. (2024). Graphite recovery from waste Li-ion battery black mass for direct re-use. Minerals Engineering, 208, 108587.*

Funded by the European Union

Views and opinions expressed are those of the author(s) only and do not necessarily reflect those of the European Union or CINEA. Neither the European Union nor the granting authority can be held responsible for them. This project has received funding from Horizon Europe research and innovation programme under Grant Agreement No.1069890

number; however, the presence of Co, Mn, and Ni indicates that the structure is likely NMC (as evidenced by the lighter regions in the back-scattered SEM image), which is further supported by the XRD data in Figure 55. The presence of Al and F is attributed to the aluminium foil (for Al) and PVDF and/or electrolyte (for F). The SEM image of the BM03-2 sample also shows lighter areas corresponding to residual NMC, as confirmed by the EDS results. However, the quantity of these lighter areas is less than in BM03-1. These residues might negatively affect the electrochemical performance of the recycled graphite, as organic impurities or metals in the leach residue could cause undesired reactions in the lithium-ion battery during cycling.

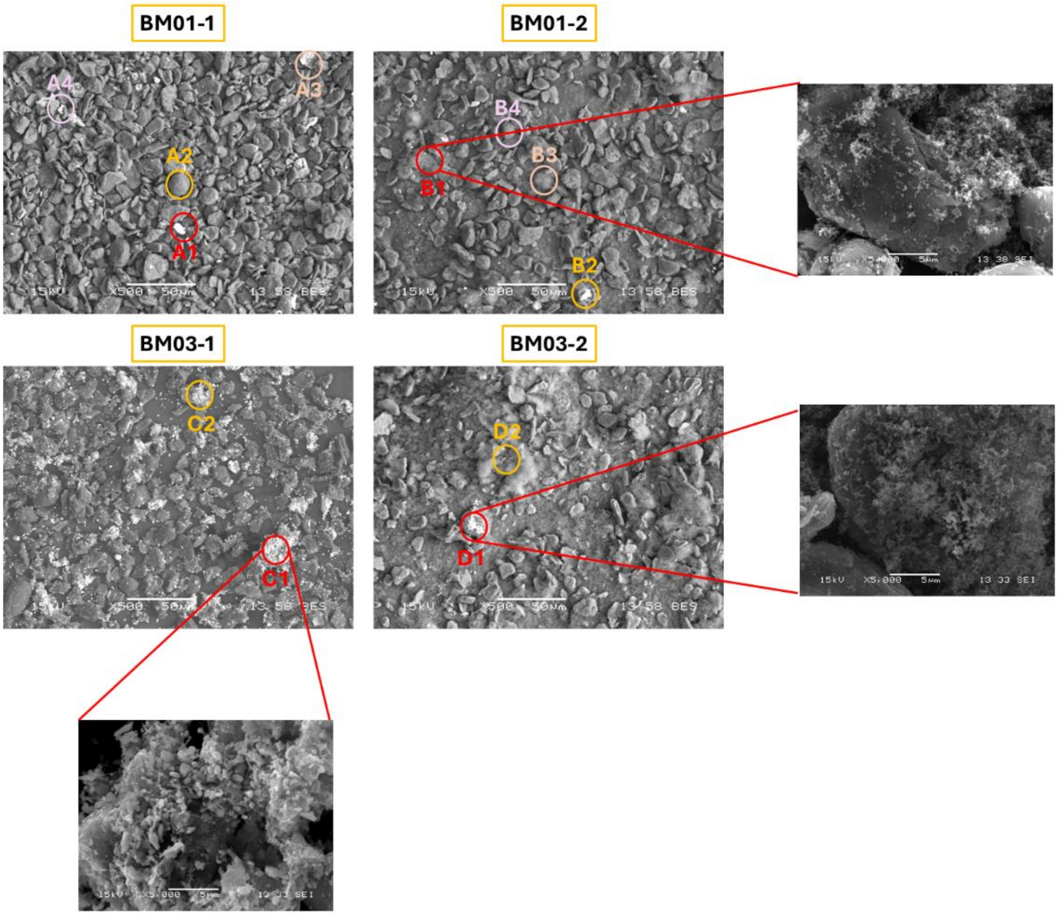

Figure 56. SEM figure of recycled graphite.

Table 14. Elemental Distribution obtained by EDS from selected zones in Figure 55.

Elements (at. %)	C	O	F	Al	S	Cl	Cu	P	Mn	Co	Ni
A1	51.643	29.795	4.416	10.424	2.495	0.155	0.916	-	-	-	-
A2	76.070	15.605	-	0.657	4.981	-	2.688	-	-	-	-
A3	71.727	28.273	-	-	-	-	-	-	-	-	-
A4	70.378	26.507	-	1.549	-	-	-	1.566	-	-	-
B1	79.517	20.483	-	-	-	-	-	-	-	-	-
B2	62.949	30.031	-	-	-	-	-	7.030	-	-	-
B3	77.537	22.463	-	-	-	-	-	-	-	-	-
B4	77.836	22.164	-	-	-	-	-	-	-	-	-
C1	47.893	29.750	6.209	8.130	-	-	-	-	5.871	5.362	13.797
C2	57.359	30.306	4.223	6.101	-	-	-	-	0.690	0.276	1.045
D1	71.018	19.447	-	8.005	-	-	-	-	0.220	0.351	0.959
D2	76.294	23.706	-	-	-	-	-	-	-	-	-

8.2 Electrochemical characterization of recycled graphite from black mass

The parameters for electrode preparation (including the amounts of CMC, carbon black, and active material), coin cell assembly conditions (the type of coin cell, electrolyte volume, and separator type), as well as the electrochemical test conditions, are detailed in Table 15.

Funded by the European Union

Views and opinions expressed are those of the author(s) only and do not necessarily reflect those of the European Union or CINEA. Neither the European Union nor the granting authority can be held responsible for them. This project has received funding from Horizon Europe research and innovation programme under Grant Agreement No.1069890

Table 15. Electrode preparation, coin cell assembly and electrochemical test conditions for commercial graphite, BM01-1, BM01-2, 3-1 and BM03-2.

BM01-1, BM01-2, BM03-1 and BM03-2 electrode test specifications		
Electrode preparation	Binder type and amount	CMC – 5 wt%
	Carbon black amount	Super P – 5 wt%
	Active material amount	90 wt.%
	Electrode thickness	Wet thickness ~300 µm
	Mass Loading (mg/cm^2)	~5 mg/cm^2
Coin cell assembly	Coin cell type	2016
	Electrolyte type	60 µl of 1M $LiPF_6$ in EC:DMC
	Half-cell or full-cell	Half-cell
	Separator	Celgard 2400
Electrochemical tests	Charge/discharge test parameters	Voltage range: 1.5-0.1 V vs. Li/Li$^+$ Current: C/20 and C/10
	Cyclic Voltammetry	Voltage range: 1.5-0.1 V vs. Li/Li$^+$ Scan rate: 0.1 mV/second
	Electrochemical Impedance Spectroscopy	Frequency range: 0.01 Hz- 100 kHz

Views and opinions expressed are those of the author(s) only and do not necessarily reflect those of the European Union or CINEA. Neither the European Union nor the granting authority can be held responsible for them. This project has received funding from Horizon Europe research and innovation programme under Grant Agreement No.1069890

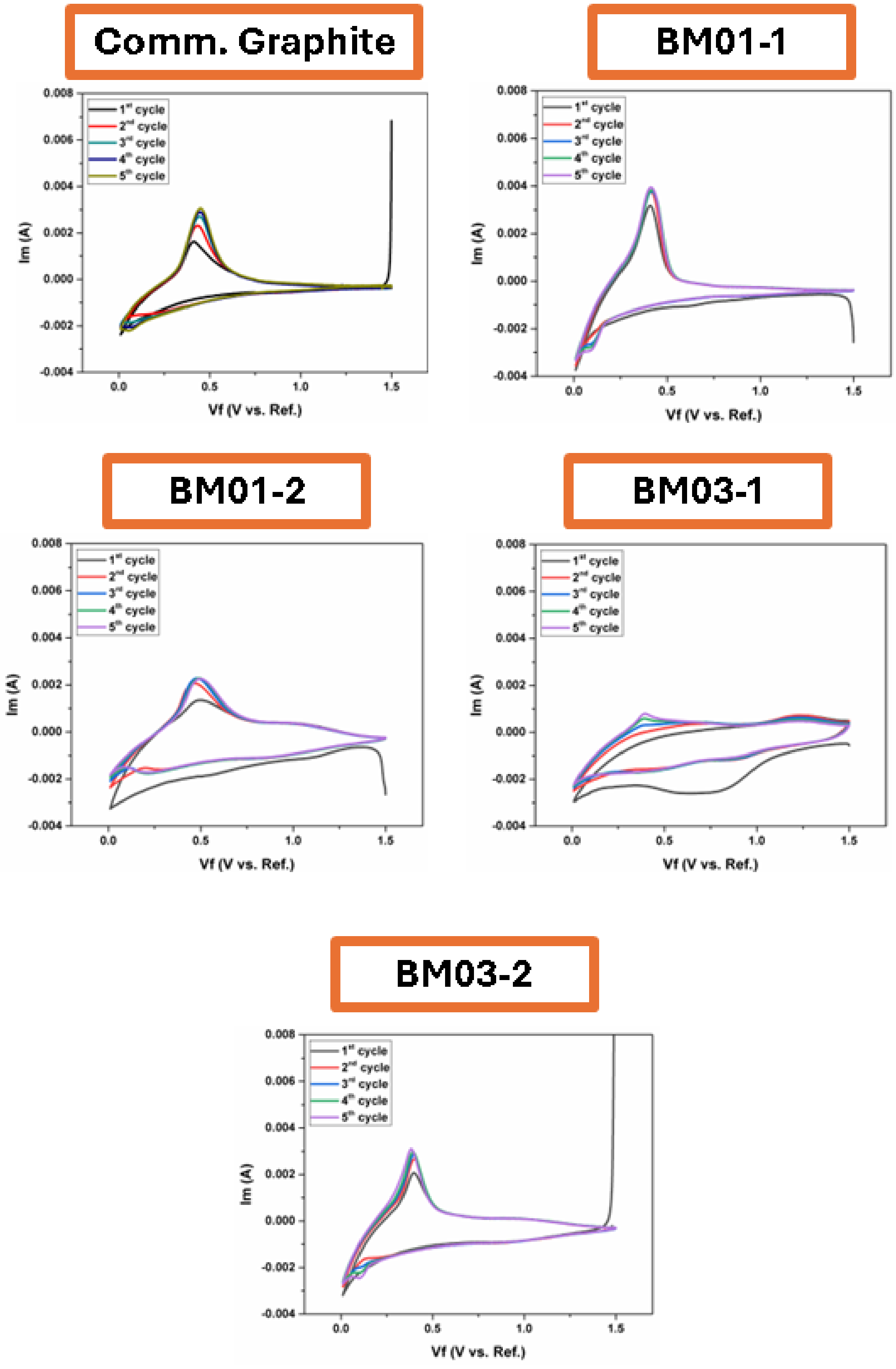
Comm. Graphite

BM01-1

BM01-2

BM03-1

BM03-2

Figure 57. Cyclic Voltammetry curves of commercial graphite, BM01-1, BM01-2, BM03-1 and BM03-2.

Funded by the European Union

Views and opinions expressed are those of the author(s) only and do not necessarily reflect those of the European Union or CINEA. Neither the European Union nor the granting authority can be held responsible for them. This project has received funding from Horizon Europe research and innovation programme under Grant Agreement No.1069890

The CV curves of the commercial graphite, BM01-1, BM01-2, 3-1 and BM03-2 are given in Figure 57. In the cathodic curve of commercial graphite, two distinct reduction peaks are observable, one small and one sharp, located at around ~ 0.75 V and 0.1 V corresponding to the initial formation of an SEI film on the surface of the electrode and the insertion of Li^+ into graphite to form LiC_6, respectively. Within the anodic curve of commercial graphite electrode, an oxidation peak is evident, located at approximately 0.43 V, attributed to extraction of Li^+ from graphite [9]. The CV curves of recycled materials show that samples BM01-1 and BM03-2 are in complete agreement with the commercial graphite, whereas this alignment is not observed in samples BM01-2 and BM03-1. This discrepancy can be attributed to the residual NMC and P (Table 14) exist in these two samples, which likely have a negative impact on the reactions that are expected to occur.

Electrochemical impedance spectroscopy (EIS) results for the commercial and recycled graphite samples are presented in Figure 58. These results were obtained before and after five cycles CV test. In the Nyquist diagrams for all samples, a semicircle appears in the high-frequency range, while a straight line is observed in the low to mid-frequency range. The intercept on the real axis in the high-frequency region corresponds to the internal resistance (Rs) of the battery, whereas the semicircle in the mid-frequency region represents the charge transfer resistance (Rct), and W corresponds to ion diffusion resistance within the active material. The EIS results for the commercial graphite show low internal and charge transfer resistances both before and after five CV cycles. In the recycled samples, only BM03-2 exhibits similarly low internal and charge transfer resistances, while samples BM01-1, BM01-2, and BM03-1 display higher resistances, which affects the battery performance negatively.

---

[9] *Liu, K., Yang, S., Luo, L., Pan, Q., Zhang, P., Huang, Y., ... & Li, Q. (2020). From spent graphite to recycle graphite anode for high-performance lithium ion batteries and sodium ion batteries. Electrochimica Acta, 356, 136856.*

Views and opinions expressed are those of the author(s) only and do not necessarily reflect those of the European Union or CINEA. Neither the European Union nor the granting authority can be held responsible for them. This project has received funding from Horizon Europe research and innovation programme under Grant Agreement No.1069890

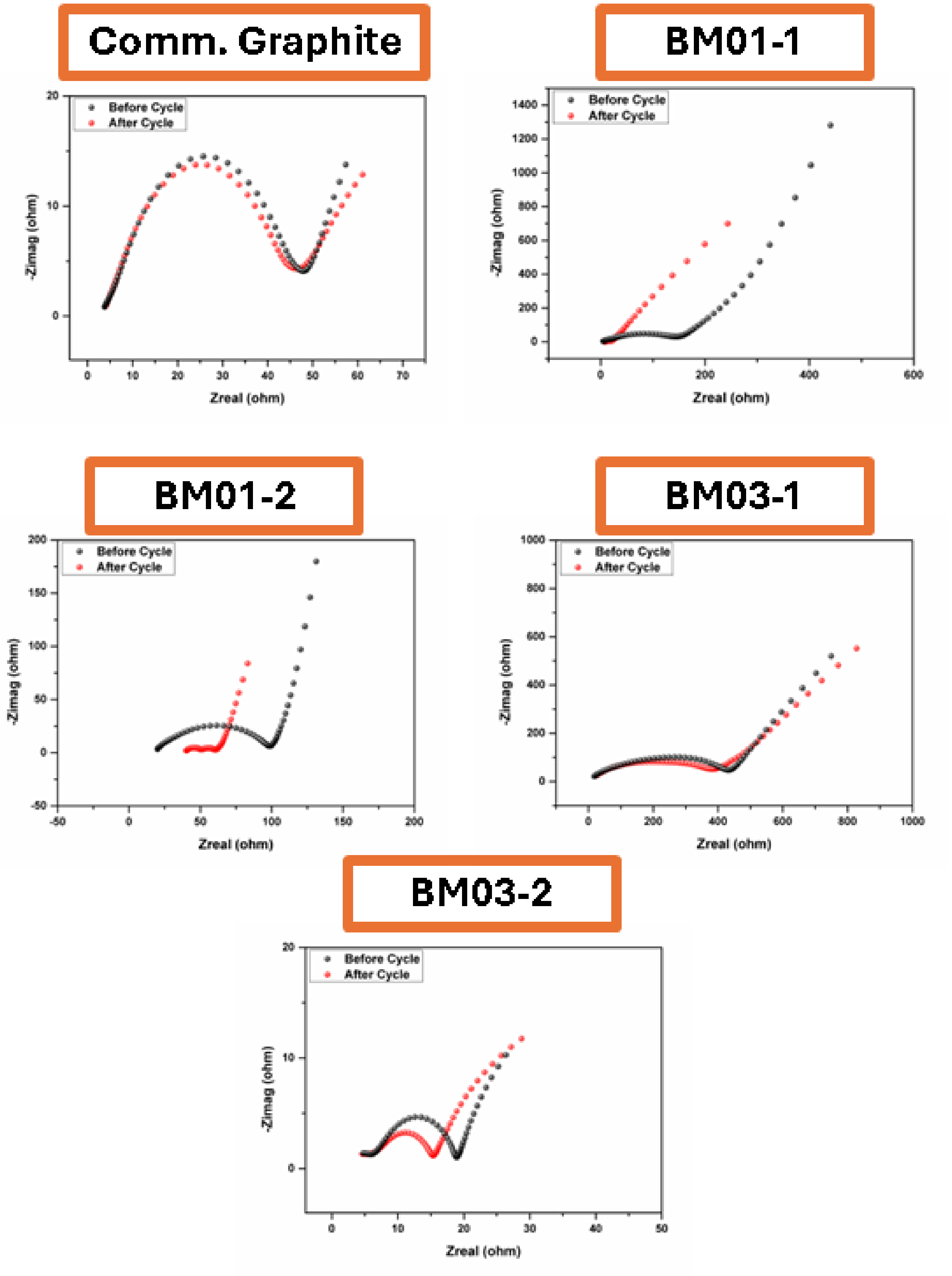

Figure 58. Nyquist plots of commercial graphite, BM01-1, BM01-2, BM03-1 and BM03-2.

Views and opinions expressed are those of the author(s) only and do not necessarily reflect those of the European Union or CINEA. Neither the European Union nor the granting authority can be held responsible for them. This project has received funding from Horizon Europe research and innovation programme under Grant Agreement No.1069890

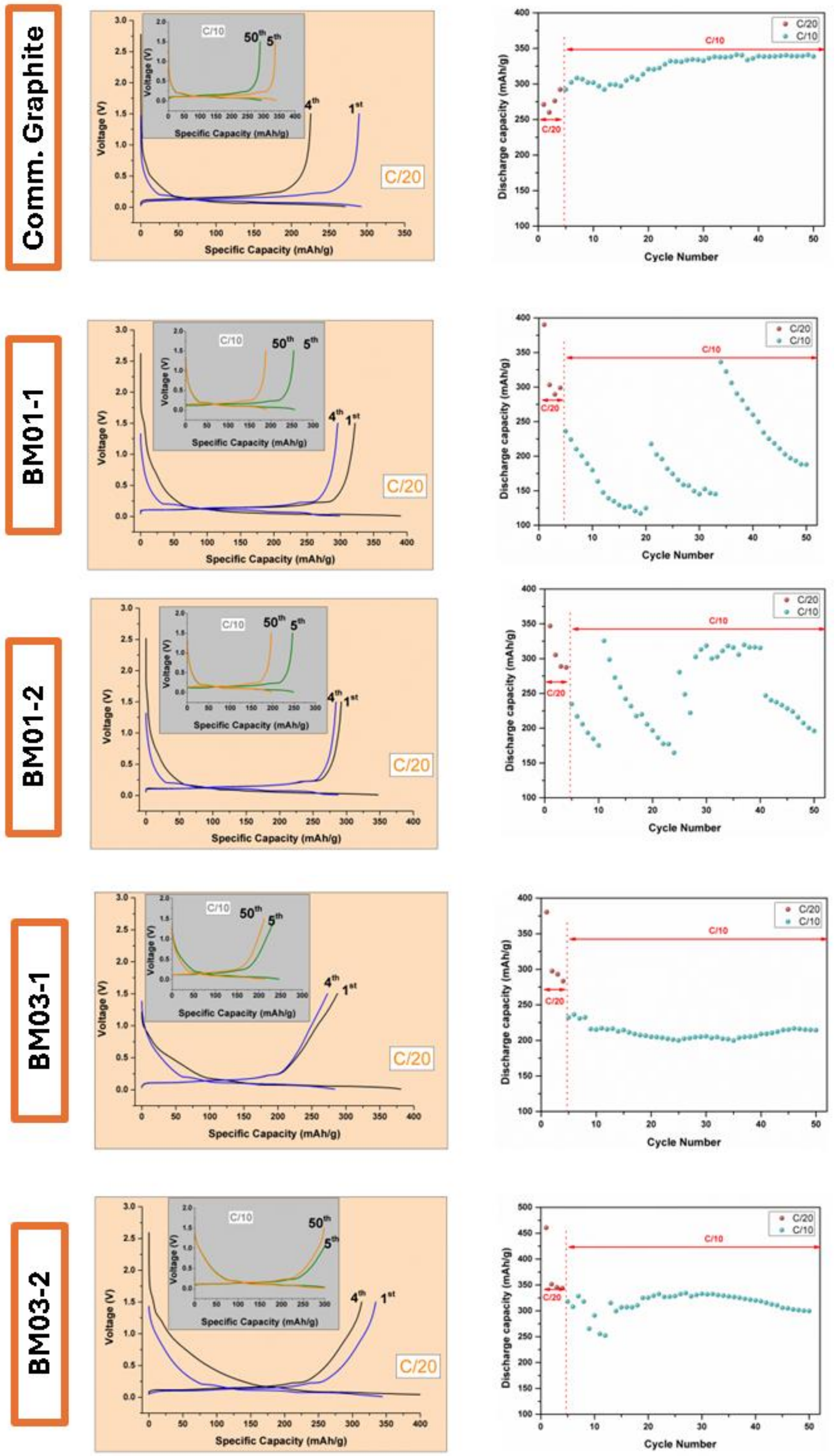

Figure 59. Electrochemical galvanostatic charge/discharge curves and cycle performances of commercial graphite, BM01-1, BM01-2, BM03-1 and BM03-2.

Funded by the European Union

Views and opinions expressed are those of the author(s) only and do not necessarily reflect those of the European Union or CINEA. Neither the European Union nor the granting authority can be held responsible for them. This project has received funding from Horizon Europe research and innovation programme under Grant Agreement No.1069890

Figure 59 presents the electrochemical galvanostatic charge/discharge curves at C/20 (first 4 cycles) and C/10 C-rates for commercial graphite, BM01-1, BM01-2, BM03-1 and BM03-2 samples. After the first cycle at a C/20 C-ratio, commercial graphite exhibited a specific capacity exceeding 271 mAh g^{-1}, while the BM01-1, BM01-2, BM03-1 and BM03-2 samples demonstrated specific capacities of 390, 347, 380 and 347 mAh g^{-1}, respectively. Following 50 cycles (4 cycles at C/20 + 46 cycles at C/10 C-rate), commercial graphite displayed a specific capacity of 338 mAh g^{-1}, whereas BM01-1, BM01-2, BM03-1 and BM03-2 samples displayed specific capacities of 188, 196, 214 and 300 mAh g^{-1}, respectively. Although BM01-1 and BM01-2 demonstrate relatively good capacities, the significant fluctuations between cycles are likely to negatively impact long-term cycling performance, making them unsuitable for scale-up applications due to the inconsistency in capacity retention. In contrast, BM03-1 and BM03-2 exhibit more stable cycling performance across cycles. Among the recycled samples, BM03-2 appears to be the most promising for scale-up, offering both higher capacity values and stability.

9. The scaling-up the cell manufacturing research

9.1 Li-ion Cell Manufacturing Process Flow

General aspects for Li-ion cell manufacturing are given in this section. The flow chart of the coin and pouch cell scale Li-ion batteries is illustrated in Figure 60.

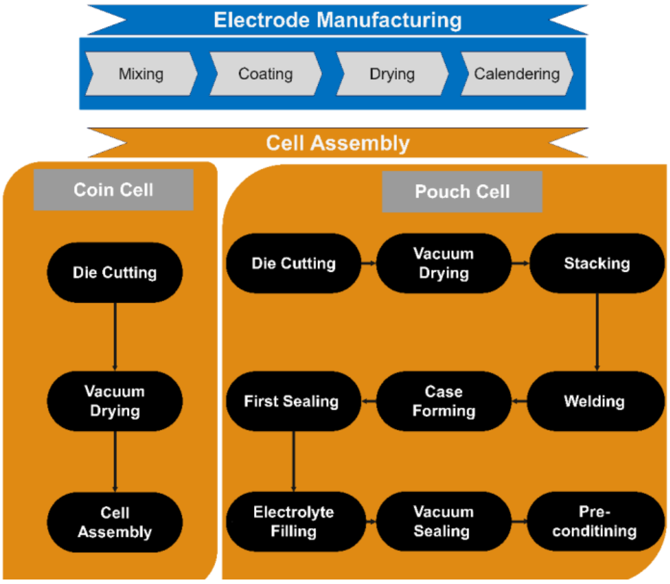

Figure 60. The flowchart of the cell manufacturing.

The manufacturing processes for lithium-ion batteries exhibit both similarities and differences when comparing coin and pouch cells. While the electrode manufacturing

Views and opinions expressed are those of the author(s) only and do not necessarily reflect those of the European Union or CINEA. Neither the European Union nor the granting authority can be held responsible for them. This project has received funding from Horizon Europe research and innovation programme under Grant Agreement No.1069890

processes are fundamentally similar for both types of cells, the primary distinctions arise during the cell assembly stages. Detailed information regarding the electrode manufacturing and cell assembly procedures will be presented in the subsequent.

9.1.1 Electrode Manufacturing

The stages of the electrode manufacturing are (i) mixing materials in a vacuum mixer (to make a slurry), (ii) casting the slurry on the current collector, and drying (to evaporation solvent and cast), and (iii) calendaring. The electrode manufacturing process were carried out under the controlled humidity atmosphere by the help of a dehumidifier.

i. **Mixing:** The components for the anode and cathode mixtures are initially subjected to drying in a vacuum dryer for 24 hours to eliminate any residual moisture. In the slurry preparation phase, the binder is first dissolved in an appropriate solvent using a vacuum mixer. Deionized water and N-methyl-2-pyrrolidone (NMP) are employed as solvents for the anode and cathode, respectively, while carboxymethyl cellulose (CMC) and polyvinylidene fluoride (PVDF) are chosen as binders. Once the binder is completely dissolved in the solvent, active materials and conductive carbon black are introduced into the viscous solution. Prior to this addition, the active materials and conductive carbon are mechanically mixed to ensure a homogeneous distribution. The vacuum mixing process is employed for a specific duration to guarantee that all components are uniformly mixed, free from any agglomeration or precipitation.

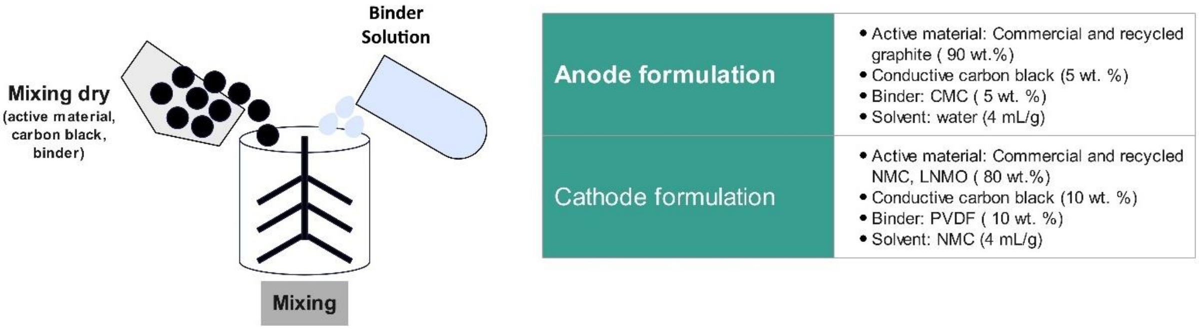

Anode formulation	• Active material: Commercial and recycled graphite (90 wt.%) • Conductive carbon black (5 wt. %) • Binder: CMC (5 wt. %) • Solvent: water (4 mL/g)
Cathode formulation	• Active material: Commercial and recycled NMC, LNMO (80 wt.%) • Conductive carbon black (10 wt. %) • Binder: PVDF (10 wt. %) • Solvent: NMC (4 mL/g)

Figure 61. The schematic illustration of vacuum mixing of electrode components.

ii. **Coating and drying:** The subsequent steps involve the coating and drying of the slurry onto the current collectors, with copper used for the anode and aluminium for the cathode. Initially, the foil is placed on a semi-automatic coating device, where a slight vacuum is applied to ensure a smooth surface and to prevent waviness during the coating process. The slurry is then poured onto the foil, and an adjustable doctor blade is employed to achieve a specific thickness for the electrode layer. For coin cells, the slurry is coated on one side, whereas for pouch cells, it is applied to both sides. Following this, the uniformly coated foil is dried at room temperature for a specified duration, followed by drying at 70 °C overnight in a vacuum environment.

A schematic illustration of the coating and drying processes is presented in Figure 62.

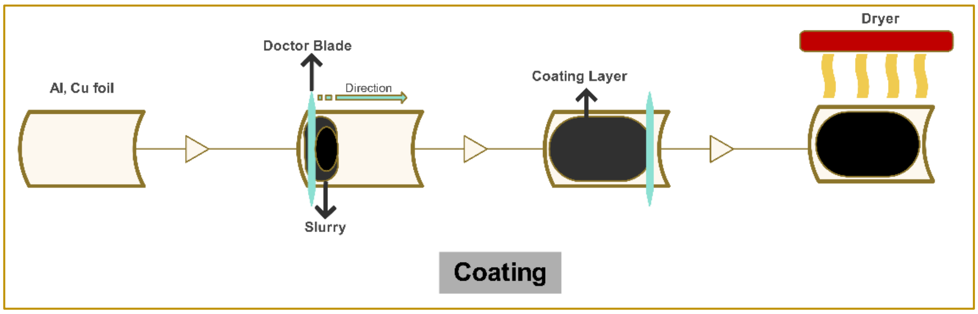

Figure 62. The schematic illustrations for the coating and drying processes.

iii. **Calendering:** The calendering process is a critical step in the manufacturing of lithium-ion batteries, significantly enhancing the quality and uniformity of the anode and cathode electrode layers prior to their assembly into battery cells. This process involves passing the electrode sheets through a series of precision rollers that apply controlled pressure to compress, densify, and smooth the material. By reducing the thickness and increasing the density of the electrode layers, calendering ensures optimal contact between the active materials and the current collector, thereby improving conductivity and overall battery efficiency. Furthermore, calendering standardizes the thickness and surface characteristics of the electrodes, which is essential for maintaining uniformity in large-scale production. A well-calendered electrode facilitates improved lithium-ion transport during charge and discharge cycles, ultimately enhancing battery capacity, energy density, and overall performance. Additionally, numerous electromechanical effects occur during the electrochemical cycling within the cell, and the calendering process helps preserve the mechanical integrity of the electrodes. In summary, calendering plays a vital role in maximizing the efficiency, durability, and safety of lithium-ion batteries. A schematic illustration of the calendering process is presented in Figure 63.

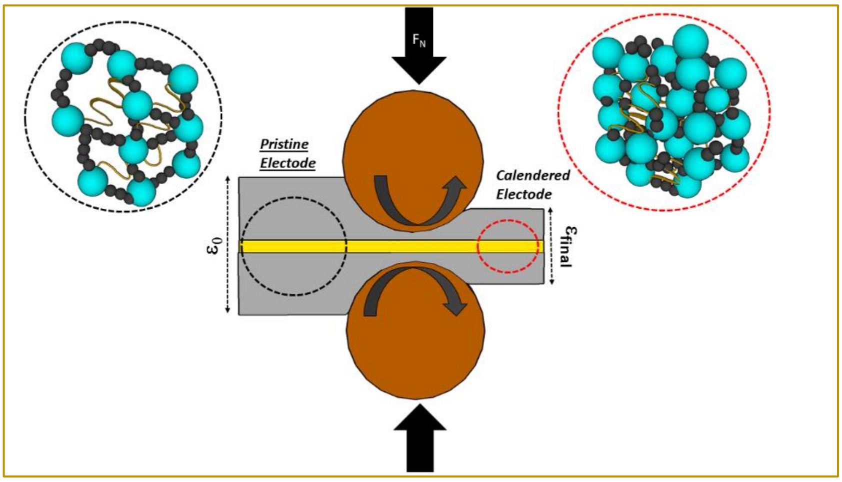

Figure 63. Schematic illustration of the calendering process.

Funded by the European Union

Views and opinions expressed are those of the author(s) only and do not necessarily reflect those of the European Union or CINEA. Neither the European Union nor the granting authority can be held responsible for them. This project has received funding from Horizon Europe research and innovation programme under Grant Agreement No.1069890

9.1.2 Cell Assembly

The main differences between the manufacturing processes of coin cells and pouch cells lie in the components of the cells and the shape of the electrodes. While the production of coin cells involves stages such as die cutting, vacuum drying, and cell assembly (cap pressing), the manufacturing of pouch cells includes additional stages, such as die cutting, vacuum drying, stacking, case forming, tab welding, 3-side sealing, electrolyte filling, vacuum sealing, preconditioning and degassing, final sealing, and aging. A detailed explanation of all stages in the cell manufacturing process is provided below.

i. **Die cutting:** The coin cell electrodes are manually punched using electrode disc cutter (ø16 mm). For pouch cells, anodes and cathodes have been cut a specific dimension of 45mmx55mm in an automatic application tool for different cells capacities. The digital photography for coin and pouch cell electrodes is given in Figure 64.

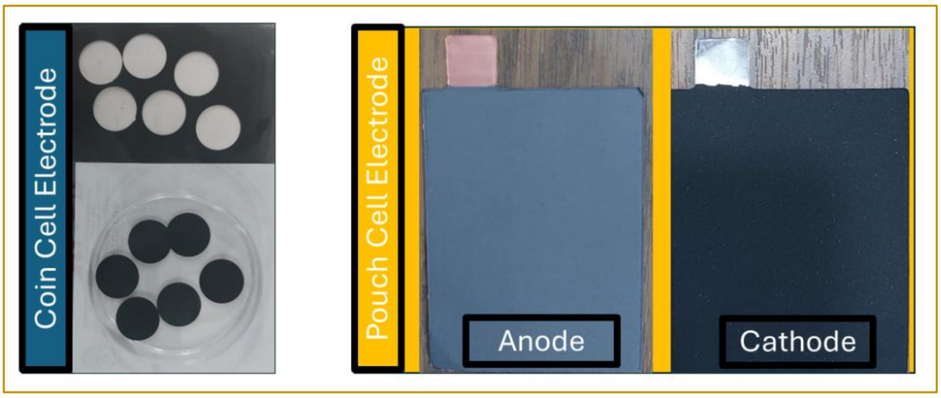

Figure 64. The digital photography for coin and pouch cell electrodes.

ii. **Vacuum drying:** Vacuum drying stage is carried out in a vacuum oven to remove the moisture and solvent on the electrodes. The vacuum drying time will be approx. 12 h to 24 h.

iii. **Stacking:** During the stacking process of pouch cells, each electrode layers are arranged in a repeating sequence of anode, separator, cathode, separator, and so on. A variety of stacking technologies are employed in this process, many of which are patented by specific manufacturers. One common method is the Z-folding technique, where anode and cathode layers are alternately inserted from the left and right into a Z-shaped folded separator. The polypropylene Celgard separator, typically in the form of a continuous tape, is trimmed after the stacking process is complete. Finally, the assembled cell stack is secured using adhesive green tape to ensure stability.

iv. **Welding:** Before housing the stacked layers, copper and aluminium current collectors are contacted with nickel and aluminium cell tabs using an ultrasonic

Funded by the European Union

Views and opinions expressed are those of the author(s) only and do not necessarily reflect those of the European Union or CINEA. Neither the European Union nor the granting authority can be held responsible for them. This project has received funding from Horizon Europe research and innovation programme under Grant Agreement No.1069890

welding process. The number of layers is adjusted so that capacities of the pouch cells were ensured. Ultrasonic welding process mostly limits to increase number of the layers due to the tiny nature of the current collectors. Applying strong frequency and time can destroy the foil. Therefore, the welding process must be handled very carefully to supply the current through the negative and positive terminals.

v. **Case forming:** The assembly of coin cell electrodes is typically performed manually within a controlled environment, often under an argon atmosphere inside a glove box to prevent contamination and ensure a stable assembly process. Proper alignment of the electrode discs is crucial for achieving consistent and reproducible performance across batches of coin cells. Misalignment can lead to variations in electrochemical behaviour, negatively impacting the cell's overall performance and reliability. Therefore, precise alignment during the stacking process is essential to maintain uniform current distribution and optimize the cell's operational efficiency. Closing the coin cell caps is performed with a crimper machine by applying an adjusted pressure. But for the pouch cell, manual or semi-automatic stacking equipment needed to stack the layer in a proper order. Stacked and tab welded electrodes should be placed in an Al laminated film. To protect the structural integrity of the cell after sealing, the case formation process must be completed to create an efficient space according to the cell dimensions and number of the layers.

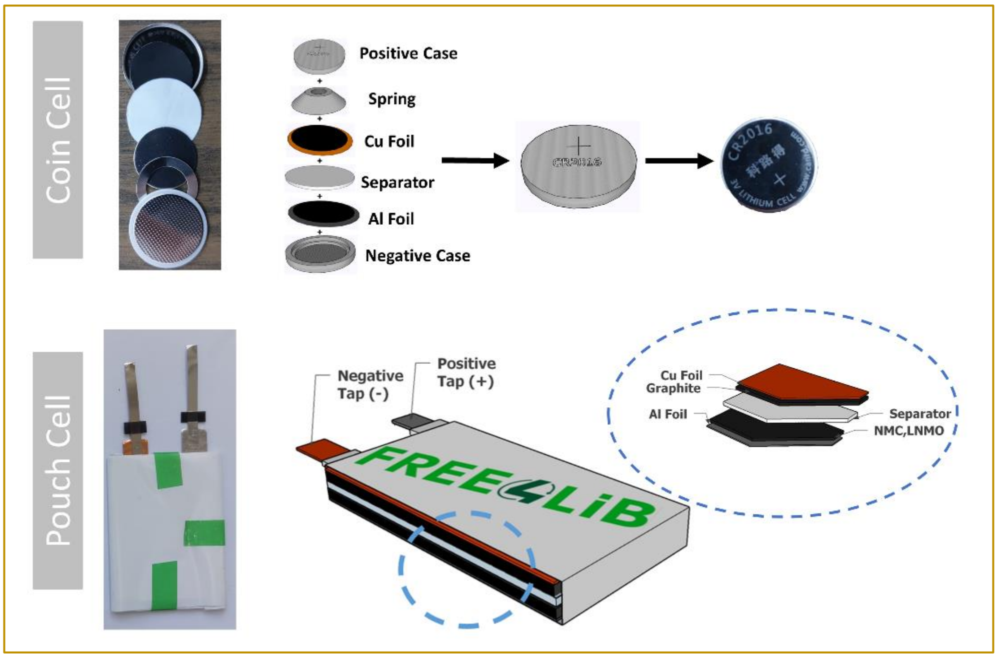

Figure 65. The components and case forming of coin and pouch cell.

vi. **First sealing and electrolyte filling:** The first sealing stage is carried out before filling electrolytes into the pouch cells. Three sides of Al laminated film are sealed, and transferred into the glove box to add the electrolyte in to the pouch. The amount of electrolyte is determined based on the amount of the cathode active material.

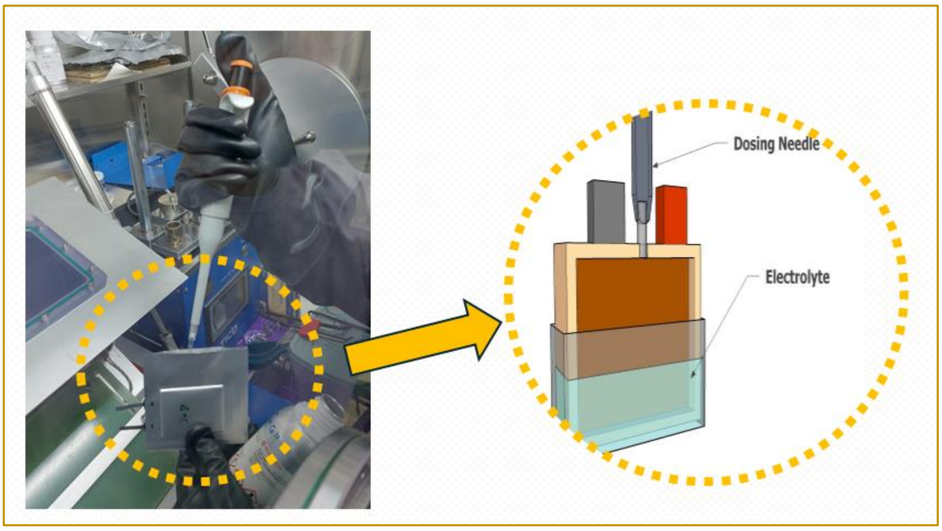

Figure 66. Electrolyte filling process in argon filled glovebox.

vii. **Vacuum sealing:** After filling the electrolyte, last side of Al laminated film is vacuum sealed in the glove box.

viii. **Pre-conditioning and degassing:** After vacuum sealing, the pouch cells are charged and discharged according to defined current and voltages. The solid electrolyte interface (SEI) layer and a gas evolution are formed during the first charge and discharge processes. The pouch cells are transferred into the glove box. After the removal of the gas, the final sealing is carried out.

ix. **Aging:** The final step of the manufacturing of pouch cells is the aging process. In this process, the pouch cell will be stored at room temperature for up to 24 h before the assessment of the battery performance.

9.2 Results of pouch cells manufacturing for FREE4LIB Project

The results of pouch cell tests for samples that demonstrated good electrochemical performance in coin cell tests are presented in this section. All pouch cells were prepared as described in Section 9.1. For tests involving recycled anodes and cathodes, galvanostatic charge/discharge tests were conducted using batteries assembled with the recycled anode or cathode paired with the corresponding commercial anode or cathode.

According to the objectives of the project, production of the cathode layers was scaled suitable for making pouch cells. All the cathode materials used in the pouch cells provided by the project partners and commercial graphite used as an anode for electrochemical tests. Pouch cell assembly steps were given in detail in the previous section. Studies have been carried out with two of each of the selected cathode powders. To ensure the validation of

Funded by the European Union

Views and opinions expressed are those of the author(s) only and do not necessarily reflect those of the European Union or CINEA. Neither the European Union nor the granting authority can be held responsible for them. This project has received funding from Horizon Europe research and innovation programme under Grant Agreement No.1069890

the results, two pouch cells were produced for each sample. Figure 67 shows the digital images of the obtained pouch cells. Pouch cells that were labelled as 28A, 28B, 30A, 30B, 32A and 32B were shown in the figure are cells produced with CPO28, CPO30 and CPO32 cathode materials.

Figure 67. Digital images of assembled pouch cell assembled with recycled cathode materials.

These pouch cells are contained several layers just for initial tests and see the electrochemical behaviours. That means, the maximum expected capacity can be just several hundred mAh. Therefore, the specific capacities were calculated for the good comparison of the results. Open circuit potentials (OCV) were measured at the beginning of the electrochemical tests. Figure 68 shows the OCV values of the obtained pouch cells.

Views and opinions expressed are those of the author(s) only and do not necessarily reflect those of the European Union or CINEA. Neither the European Union nor the granting authority can be held responsible for them. This project has received funding from Horizon Europe research and innovation programme under Grant Agreement No.1069890

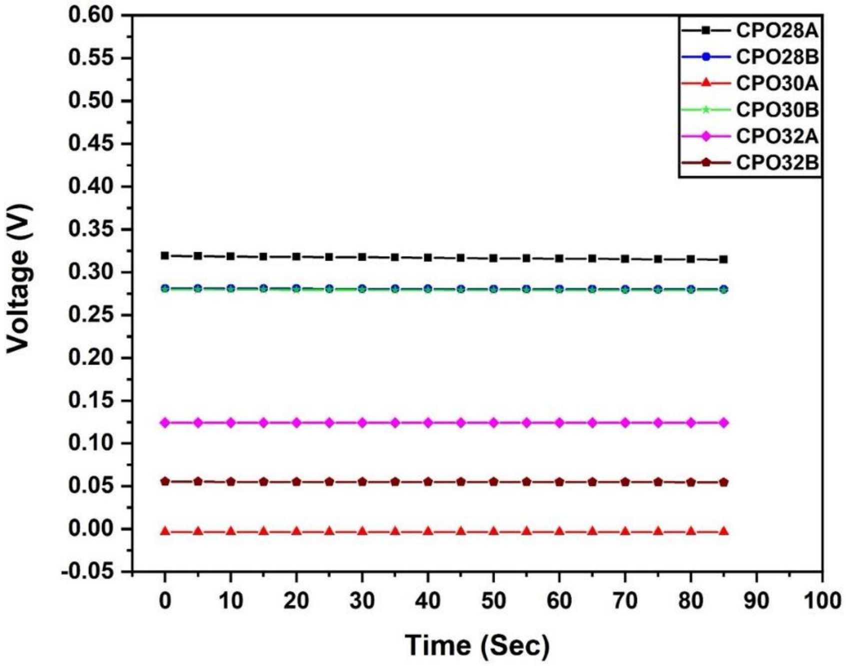

Figure 68. OCV values of the fresh cells.

OCV tests were performed under constant temperature for 90 seconds. Although their potentials are stable during the tests, OCV values are pretty low when compared with pouch cells assembled with the commercial cathode materials. OCV value of the CPO30A sample is zero that means which is attributed to unsuccessful assembling process that leads to short circuit.

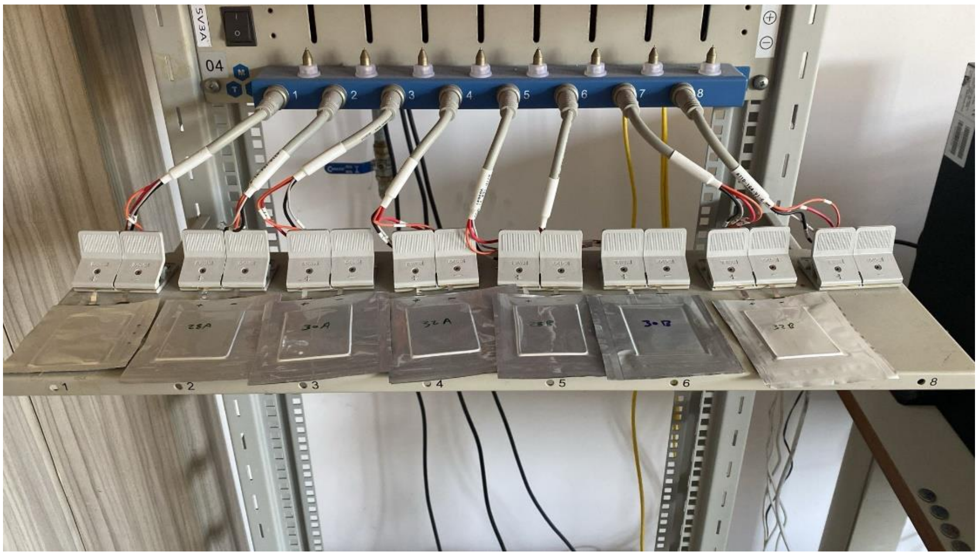

Figure 69. Digital images of the pouch cells during the electrochemical tests.

After measuring the OCV values, pouch cells are applied the formation tests. Figure 69 shows the pouch cells during the formation tests.

Funded by the European Union

Views and opinions expressed are those of the author(s) only and do not necessarily reflect those of the European Union or CINEA. Neither the European Union nor the granting authority can be held responsible for them. This project has received funding from Horizon Europe research and innovation programme under Grant Agreement No.1069890

Formation protocol is very important step for cell manufacturing process and must be handled very carefully to obtain optimum results during the further steps. Firstly, all the pouch cells have been applied to charge discharge test starting with C/20 current rate. Unfortunately, most of the pouch cells are not stable and seems to need further development in the cathode materials. All the first cycle attempts are given below separately.

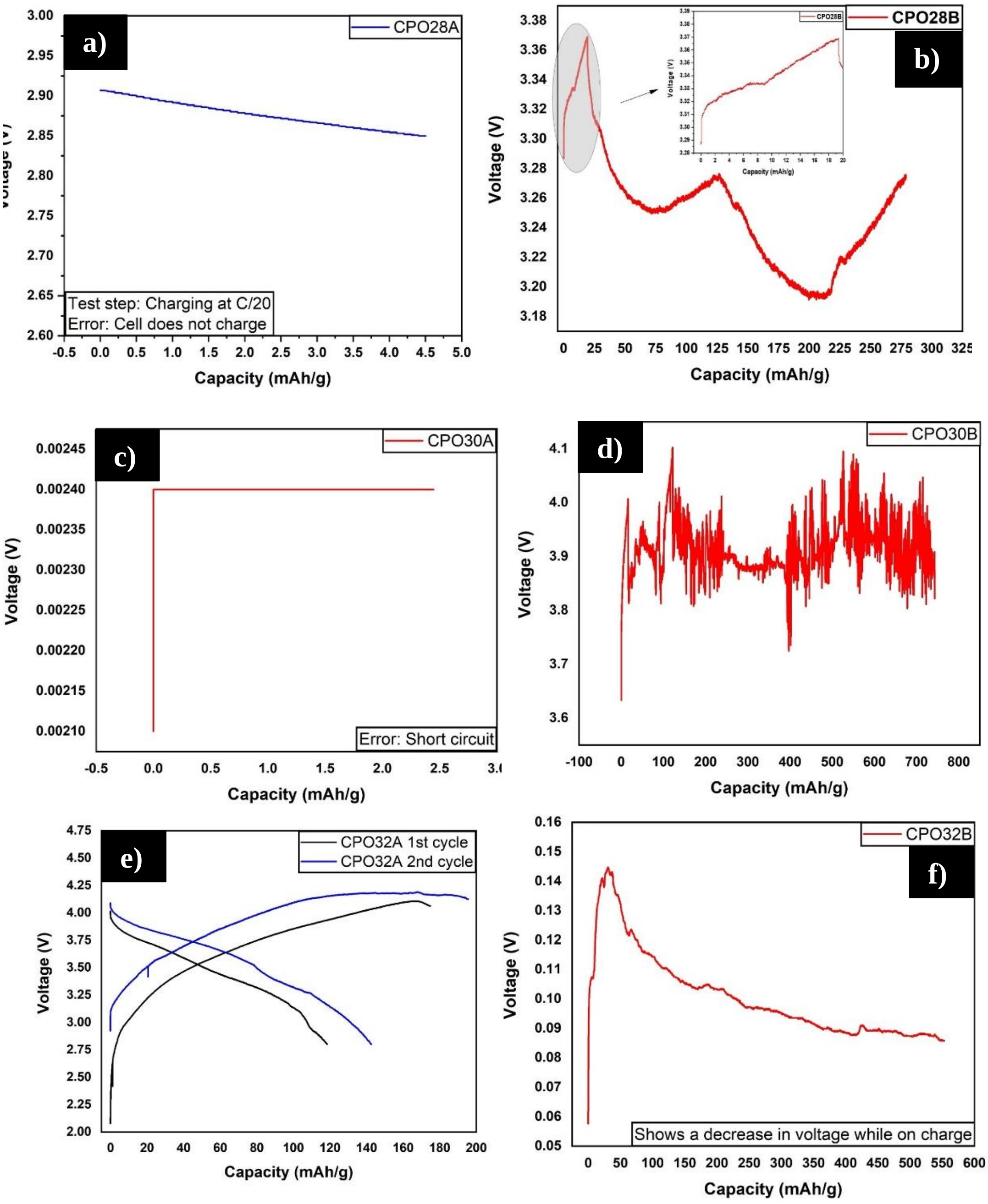

Figure 70. Electrochemical results of pouch cells: a) and b) CPO28, c) and d) CPO30, e) and f) CPO32.

The first charge and discharge cycles of the recycled powders are given in Figure 70. During the charging process, the potential must be increased but CPO28A sample show decreased

Funded by the European Union

Views and opinions expressed are those of the author(s) only and do not necessarily reflect those of the European Union or CINEA. Neither the European Union nor the granting authority can be held responsible for them. This project has received funding from Horizon Europe research and innovation programme under Grant Agreement No.1069890

potential even during the charging step. This can be explained high resistance occurring in the cell. CMO30A cell must be assembled again to explain the zero potential result. However, for the period with the limited availability of the materials, this will be carried out in the next mounts. For now, this result can be accepted as a short circuit of the pouch cell. Charge discharge test of the CPO32 sample shows the better results when compared to the other samples. But again, it could not reach the charging cut-off voltage of 4.2V. For that reason, it was manually jumped this cell to discharge after a while (in both cycles, manually jumped it to discharge). This can also be explained by the higher resistance in the cells. In the subsequent tests, EIS analysis will be performed on the cells before electrochemical tests. Besides, the assembled cell exhibited a promising charge capacity of 200 mAh g^{-1} and a discharge capacity of 160 mAh g^{-1} in the first cycle. This can stand as a good starting point for further studies. It is also expected to exhibit higher capacity and more stable cycle life in the gradual proportional use with commercial materials. This is an important criterion for the success of the project.

CPO28B, CPO30B, and CPO32B samples also could not reach the higher potentials during the charging process. Their resistances seem very high and leads to the voltage drop during the charging process. This shows that impurities that may have resistance-enhancing properties in these active materials should be handled more carefully in future studies.

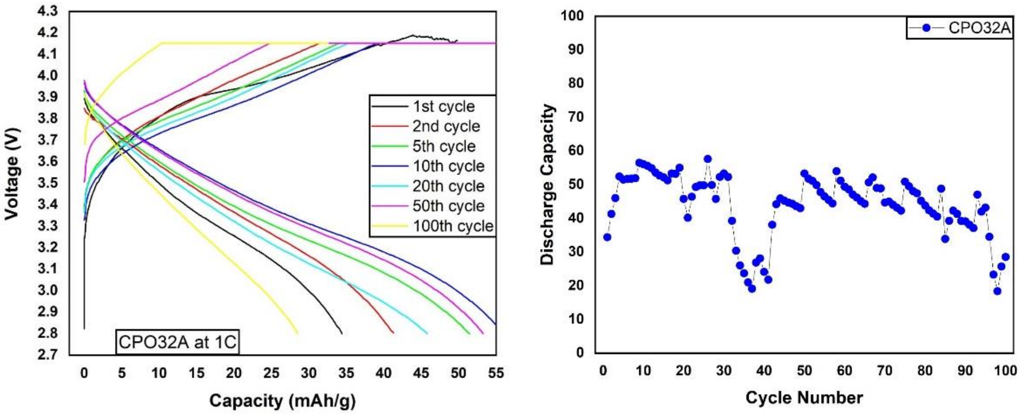

Figure 71. Electrochemical charge discharge test of CPO32 pouch cell.

Figure 71 shows the electrochemical charge/discharges tests of CPO32 at 1C current rate. 1C is normally very high for early results. As a result of this, the pouch cell gave lower capacity. However, it was important to see the cycling ability character of this sample.

Views and opinions expressed are those of the author(s) only and do not necessarily reflect those of the European Union or CINEA. Neither the European Union nor the granting authority can be held responsible for them. This project has received funding from Horizon Europe research and innovation programme under Grant Agreement No.1069890

10. Conclusions

In the context of our project, anode and cathode electrodes were produced from powders obtained through various recycling processes and evaluated for their electrochemical performance in both coin cell and pouch cell formats. In the context of our project, the battery cells prepared for electrochemical testing were initially fabricated at the coin cell level, where the tests were conducted. Subsequently, the compositions that yielded the best results were utilized to produce pouch cells, which were then subjected to further electrochemical testing. In this context, CP028, CP030, and CP032 exhibited relatively higher electrochemical performance compared to other batches in the coin cell tests. In the pouch cell tests conducted with the same compositions, the electrochemical performance did not reach the levels achieved in the coin cell tests. Possible reasons for this discrepancy may include technical issues in the pouch cell assembly process, as well as the presence of trace impurities in the powder compositions, which could significantly impact the performance at the pouch cell scale.

Views and opinions expressed are those of the author(s) only and do not necessarily reflect those of the European Union or CINEA. Neither the European Union nor the granting authority can be held responsible for them. This project has received funding from Horizon Europe research and innovation programme under Grant Agreement No.1069890